Imperial College London

Model-based development of high-pressure membrane contactors for natural gas sweetening

Ven Chian Quek

A thesis submitted for the degree of
Doctor of Philosophy of Imperial College London

Department of Chemical Engineering
Imperial College London
United Kingdom

July 2019

Declaration of Originality

The work presented in this thesis was performed in the Department of Chemical Engineering at Imperial College London between May 2015 and June 2019, under the supervision of Professor Nilay Shah and Dr. Benoît Chachuat. All of the work contained is my own unless otherwise stated. The results within this thesis have not been submitted for any other degree at Imperial College London or elsewhere.

Ven Chian Quek
July 2019

Copyright Declaration

Abstract

Membrane separation and chemical solvent absorption technologies are both widely employed for Natural Gas (NG) Sweetening. A new hybrid process combining the advantages of both technologies, called membrane contactor (MBC), has been drawing significant attention over the past decade. MBC is considered a promising process for intensification purposes, as it can provide high specific surface areas, independent control over the gas and liquid flow rates, modularity, and compactness. Nevertheless, no literature to date has conducted a process-wide assessment of using MBC for NG sweetening, and therefore, its intensification potential cannot be systematically quantified. This challenge is the motivation of the research presented in this thesis.

The main objective of this work is to develop process-wide modeling of NG sweetening using MBC to enable MBC process design and performance assessment. A predictive mathematical model of high-pressure MBC for NG sweetening with alkanolamines as the chemical solvent was developed. The model explicitly accounts for the rates of mass transfer through the membrane, diffusion, and chemical reaction in the liquid phase. A combination of 1-d and 2-d mass-balance equations to predict the CO_2 absorption flux was considered, whereby the degree of membrane wetting itself is calculated using the Laplace-Young equation based upon knowledge of the membrane pore-size distribution, fluid flow configuration, and operating condition. The MBC model can also predict the solvent evaporative losses and the hydrocarbon (HC) absorption into amine solvent, which is important to maintain the CO_2 absorption performance in MBC and to quantify the potential solvent make-up and product loss. Then, a full-scale steady-state MBC-based NG sweetening process was developed whereby the MBC model (absorption section) is integrated with the conventional solvent regeneration model (desorption section) in the gPROMS ProcessBuilder environment.

The predictive capability of the model was tested using two sets of membranes with different characteristics, against data from two experimental settings; a lab-scale MBC module, where the purification is conducted using binary gas mixtures of CH_4/CO_2 and N_2/CO_2; and a pilot-scale MBC module operated under industrially relevant conditions at a NG processing plant in Malaysia. The important operation and design parameters such as the CO_2 partial pressure, gas and liquid flowrates, pressure, temperature, liquid CO_2 loading, membrane area and fiber length were varied to determine the performance of MBC. The model results clearly showed

the change in the CO_2 absorption performance and the energy consumption related to the variables. All model predictions showed a close agreement with the measured CO_2 absorption fluxes, energy consumptions and the HC absorption and recovery from the solvent. The MBC model provided valuable research recommendations, whereby approximately 80% increase of CO_2 absorption performance was achieved in MBC pilot plant by operating a smaller diameter of hollow fiber membrane in a horizontal orientation.

The integrated process model is used to analyse the effects of various design configuration and operating conditions, such as the lean and semi-lean operations to meet sales gas specification. The experimental data and model analysis has confirmed the advantages of semi-lean operation in terms of energy reduction and physical footprint. Finally, a model based scale-up of a commercial MBC for NG sweetening was conducted to gauge its intensification potential. Overall, the scaled-up MBC commercial module showed promising prospects, whereby (i) the predicted reboiler energy per ton of CO_2 removed is lower than the conventional amine absorption column by 12 - 50%; (ii) the predicted amine loss rate per treated gas and per ton of CO_2 removed are lower compared to the typical loss rates reported in a conventional amine-based processes; and (iii) a potential savings of $\text{US\$ } 0.96 - 1.1 \text{ million yr}^{-1}$ from the HC recovery can be realized, subject to further sweetening of the flash gas. Nevertheless, the MBC may require larger footprint than conventional absorption column due to horizontal operation. Going forward, the MBC model can be used to provide research and development targets, such as the improvement in membrane specific surface area and the hydrophobicity to enable commercial MBC modules to be stacked, thereby improving the intensification potential in terms of footprint.

Acknowledgments

Undertaking this Ph.D. has been one of the most challenging and humbling endeavors in my life thus far. None of this would have been possible without the support and guidance that I have received throughout the conception of this thesis, and I will express to the best of my abilities the gratitude, appreciation, and respect I have for all those who helped me on my journey.

Professor Nilay Shah and Dr. Benoît Chachuat, thank you for your patience, your dedication, your expert knowledge, wisdom, advice, and for keeping me enthused throughout this unforgettable journey. It is a great honor to be awarded the Senior Moulton Medal (2018) by IChemE for our journal paper. I will cherish the time learning and exchanging ideas with both of you.

Thank you to the Leadership Team of PRSB, PETRONAS, specifically Dr. Shahidah Mohd Sharriff and Dr. Nasir Darman for entrusting and for allowing me to pursue this research project. I am grateful to Dr. Norfaizah A Manan and Mr. M Adaham Ishak, who have been supportive of my career goals and who worked actively to provide me with the opportunities to purse my goals.

To the past and present colleagues in membrane contactor (MBC) project, in particular, Chan Zhe Phak, Syafiqa, Hajar, Nurida, Azmil, Grace, Shahril, Adam, Jamali, Amiruddin, and Francis. I thank you for your endless support and guidance in making this collaboration a success. Sara, Zaid, Rui Yan, Amira, Yu Kun, Antonio, Kyung Jae, Kai Bin – thank you for your listening, advice, and genuine care in supporting me through this entire Ph.D. journey. I take great pleasure in calling every one of you, my colleagues, and my friends. I am very fortunate to have crossed paths with all of you; this thesis would not have been completed without the genuine care, support, and love from all of you. The great inspiration throughout our time spent working together has led to one unforgettable memory after another. All of you are some of the brightest people I've met, with work ethics that are second to none.

And of course, none of this would have been possible without the love and support from my family. My dear wife, Kheng Ying, thank you for all the sacrifices that you had made in making sure my dreams became a reality. I genuinely admire your resilience and your faith in me.

Having to revolve your life around my busy schedule and moving to our new apartment with me in London, away from your family, friends, and the familiarity of Malaysia. I hope that you do not feel neglected in any way or form throughout our journey in creating this thesis. Your care and love have truly gotten me through many mental and emotional adversities. To my son, Quinton, you have made me stronger, better, and more rewarding than I could ever imagine. You are my inspiration to achieve greatness. I love you. You gave me the strength to persevere.

Finally, I would like to dedicate this work to my parents, without their upbringing and nurturing; I would not have been where or what I am today. I hope that I make both of you proud.

Ven Chian Quek

2019

Table of Contents

Chapter 1 Introduction

1.1 Background

Natural Gas (NG) is presently the third most-utilized form of fossil fuel energy and is widely used for electricity production, heat and transportation. In the reference case of the International Energy Outlook (International Energy Outlook, 2016), the world's NG consumption is expected to increase by 69% between 2012 and 2040, accounting for 29% of the energy consuming market, and surpassing coal as the second most utilized fuel by 2030. NG consists of a mixture of combustible hydrocarbon gases typically from methane (CH_4) to pentane (C_5H_{12}), with impurities such as carbon dioxide (CO_2). Removal of CO_2 from NG is vital for various reasons. The sales gas specification for NG typically imposes a CO_2 content lower than 2% (TransCanada, 2016). In liquefied natural gas (LNG) plants, CO_2 should be removed further to meet the tight specification of <50 ppmv, so as to avoid freezing in low-temperature chillers (liquefaction process); and in ammonia plants, CO_2 concentrations of <100 ppmv are needed to prevent catalyst poisoning (Boucif et al., 2012; Hoff, 2003). As far as pipeline transport is concerned, CO_2 removal avoids pumping any extra volume of gas and reduces the risk of corrosion when moisture is present in process equipment and pipelines. Regarding NG utilization lastly, the presence of CO_2 reduces the heating value of NG.

Figure 1.1 depicts the available CO_2 removal techniques based on physical and chemical principles, including absorption, adsorption, membrane separation, direct conversion, and cryogenic fractionation. The selection of these methods depends on several parameters such as the (i) CO_2 content and partial pressure in the feed stream; (ii) required CO_2 purity of the treated gas; (iii) nature of other components present in the feed stream; (iv) gas flowrate, pressure and temperature of the feed stream; and (v) capital and operating costs for the process. Figure 1.2 shows the general guidelines for process selection of CO_2 removal technologies.

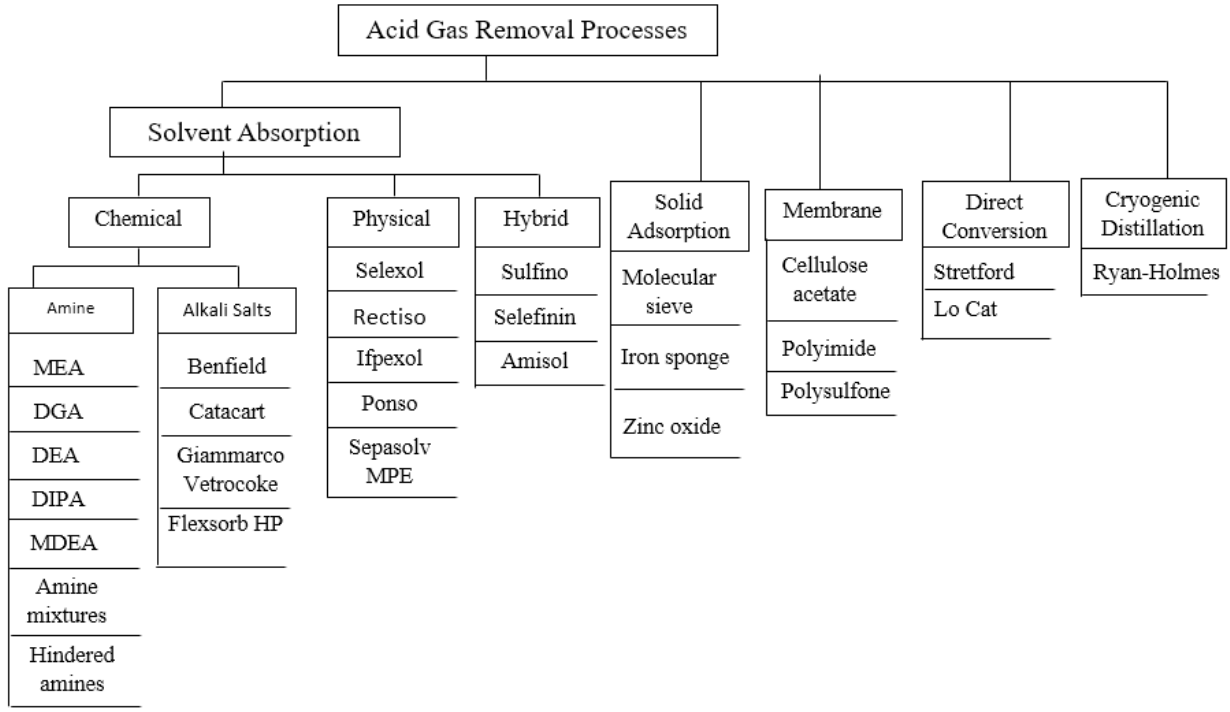

Figure 1.0.1: Available technologies for CO_2 removal (Kidnay and Parrish, 2006)

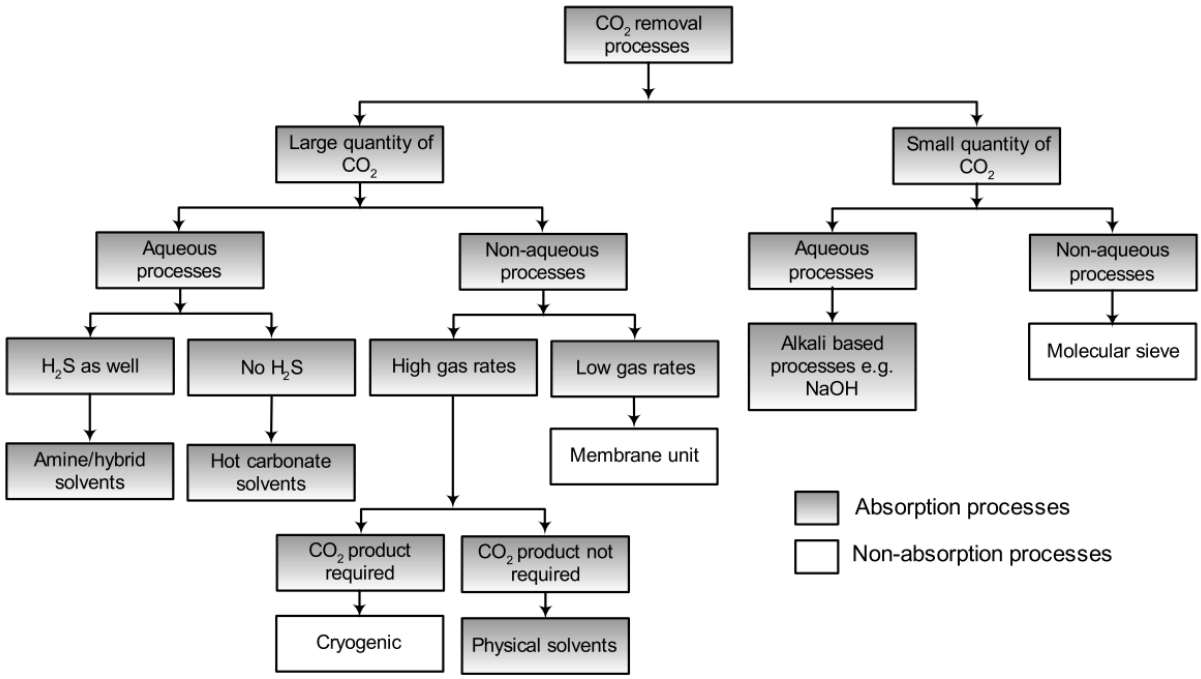

Figure 1.0.2: Guidelines for selection of CO_2 removal processes (Shaw and Hughes, 2001)

Both Figures 1.1 and 1.2 show that absorption using solvents is a commonly used process for CO_2 removal. In particular, chemical solvent absorption remains the most widely adopted technology to capture CO_2, using conventional packed, spray or bubble column absorption towers as depicted in Figure 1.3. These processes are based on the CO_2 chemical dissolution in an alkaline solvent, through its selective reaction with one or several of the solvent components. Then, the CO_2- rich solvent is regenerated via the application of heat producing a stream of lean solvent and a CO_2 gaseous stream (Wang et al., 2011). The lean solvent is then recycled back to the conventional absorption towers. About 90% of the acid gas treating processes in operation use alkanoamines solvents (alkaline), such as methylethanolamine (MEA), diethanolamine (DEA), and methyldiethanolamine (MDEA), due to their versatility and ability to remove acid gases to ppm levels (Paul et al., 2007). Nonetheless, conventional absorption towers have a high capital cost and a large physical footprint, and they are subject to operational problems such as flooding, channeling, foaming and liquid entrainment (Gabelman & Hwang, 1999).

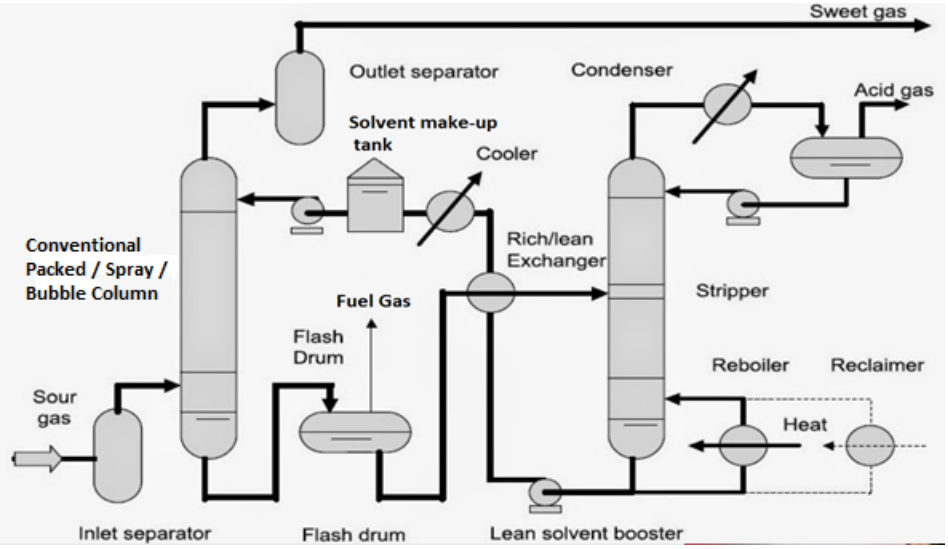

Figure 1.0.3: A typical NG sweetening by chemical solvent absorption. Adapted from: Gas Processors Suppliers Association (2004).

Membrane separation technology has been applied since the 1980s for CO_2 removal in large-scale applications, due to their potential to reduce the footprint and the capital and operating costs (He & Hägg, 2012). For membrane separation, CO_2 selectivity is provided by the membranes themselves. Their selectivity is related to the nature of the membrane material,

which usually consists of thin polymeric films such as cellulose acetate, and to the mixture itself based on the relative rates at which the constituent species permeate. The components dissolve in the polymer at one surface and are transported across the membrane as a result of a concentration gradient (Subhasish, 2017). The concentration gradient is maintained by the difference in the partial pressure of the components at either side of the membrane, as depicted in the left plot of Figure 1.4.

Unlike chemical solvent absorption, the selectivity of this separation process is low, which can lead to significant product loss. Furthermore, the purity of the captured CO_2 is low for the same reason (IEA, 2004; Wang et al., 2011). The right hand plot in Figure 1.4 shows a two-stage membrane separation process with intermediate re-compression in order to increase methane recovery to 98.7%. Greater levels of methane recovery or higher CO_2 purity at the permeate side can be achieved by the application of multistage separation, but can quickly become uneconomical due to the membrane cost and the recompression energy required (IEA, 2004; Kidnay and Parrish, 2006).

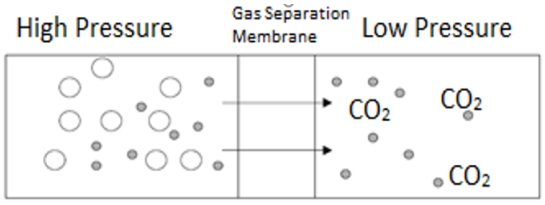

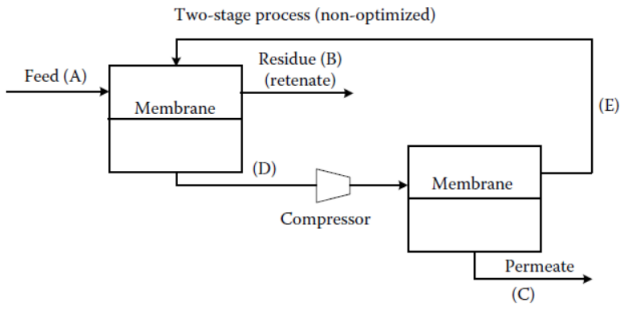

	A	B	C	D	E
Composition (mole %)					
Methane	93.0	98.0	18.9	63.4	93.0
Carbon dioxide	7.0	2.0	81.1	36.6	7.0
Flow rate (MMscfd)	20.00	18.74	1.26	3.16	1.90
Pressure (psig)	850	835	10	10	850

Methane recovery = 98.7%

Figure 1.0.4: Left: Principle of membrane separation (Adapted from Hoff, 2003); **Right:** A non-optimized two stage CO_2/CH_4 membrane separation process (Kidnay and Parrish, 2006).

As the worldwide demand for NG increases, it is paramount to improve the existing processes of NG sweetening. In recent years, alternative technologies have been developed to overcome the drawbacks of conventional technologies and improve their intensification potential in terms of energy requirements, weights and footprint at industrial scale; membrane gas absorption is one of them. Membrane gas absorption, also known as membrane contactor (MBC) is the

integration of a membrane with an absorption process, into a single unit operation. By combining membranes and solvents, MBC offers a unique way to perform gas-liquid absorption (Gabelman & Hwang, 1999). The microporous membrane acts as a non-selective phase barrier, allowing the liquid and gas phases to contact each other, yet without the dispersion of one phase into the other. This barrier prevents flooding or foaming issues from happening, thereby making MBC relatively simple to operate. Their packaging into hollow-fiber membrane (HFM) modules offers a higher mass transfer area compared with conventional packed columns, giving MBC a high intensification potential (Rangwala, 1996; Favre, 2011). This modularity also empowers a more flexible design and scale-up. The effectiveness of MBC for both pre- and post-combustion CO_2 capture, as well as NG sweetening and dehydration, has been extensively studied and compared with conventional techniques over the past decades; see, e.g., review papers by (Mansourizadeh and Ismail, 2009; Favre, 2011; He & Hägg, 2012; Hoff and Svendsen, 2014). In NG sweetening, for instance, Hoff and Svendsen (2013) reported a 75% size reduction using MBC compared to conventional packed columns. This technology has been embraced by the industry too, with recent patents on acid gas removal from NG granted to Petroliam Nasional Berhad (PETRONAS) (Quek et al., 2015) and the Gas Technology Institute (GTI) (Zhou & Meyer, 2014).

1.2 Research Aim

MBC is considered an immature technology for CO_2 removal at high pressure, and no literature to date has reported MBC as a commercially viable technology for CO_2 removal from NG. As such, the research aims to evaluate the intensification potential of MBC for NG sweetening application, with a view to bringing this technology into commercial operation.

1.2.1 Research Objectives

Mathematical models provide an effective tool to understand the CO_2 removal mechanisms in MBC, whereby a suitable approach to model CO_2 absorption in MBC utilizing solvent will be determined. The research will involve the development of the predictive MBC mathematical modeling taking into account the membrane wetting, rate of diffusion and chemical reaction in the gas and liquid phases, followed by verification of the lab-scale and pilot-scale experimental data. The impact of various parameters such as MBC's characteristics, operating parameters, and flow configurations on the CO_2 absorption performance is examined to enable MBC

optimization and process design. Then, the MBC model is integrated with other unit operations to develop a full-scale MBC based NG sweetening process model in order to analyze the effects of different conceptual designs and operational decisions for process scale-up and performance assessment.

1.2.2 Thesis outline

The thesis is structured as follows: in Chapter 2, a literature review on MBC for CO_2 removal is conducted for gas absorption using microporous, hydrophobic membranes. The literature review firstly focuses on membrane materials and characteristics as well as MBC's modes of operation. A guideline for various membrane-solvent combinations, MBC configurations and geometries are discussed. Then, the literature review of various modeling techniques for CO_2 capture in MBC utilizing amine solvent is conducted. Chapter 3 describes the development of the predictive mathematical modeling of high-pressure MBC for NG sweetening. The model predictions are verified against data from two experimental settings for a lean amine operation: a lab-scale MBC module and a pilot-scale MBC module operated under industrially relevant conditions at an NG processing plant in Malaysia. The impact of operating conditions, membrane characteristics, and module orientation are discussed, and remediation strategies are recommended. In Chapter 4, further development of the MBC model is conducted to include solvent losses from evaporation, energy balance, and hydrocarbon absorption into the solvent. The predictive capability of the model is then examined and verified with experimental data for both lab-scale and pilot-scale MBC modules for semi-lean amine operation, using a new membrane fiber compared to Chapter 3. Subsequently, in Chapter 5, for the first time, the MBC model is integrated with the solvent regeneration as a full-scale NG sweetening process model for process-wide design and operations. Again, the model predictions are verified against the pilot-scale MBC module in terms of overall energy consumption for lean and semi-lean amine operations. Model-based analysis on the pilot-scale MBC is conducted to determine (i) the solvent flowrate for lean and semi-lean operations and the impact on energy consumption; (ii) the optimum pressure at the rich solution flash drum for maximum fuel gas recovery; and iii) the amount and composition of the solvent make up required for continuous operation. Then, a model-based design scale-up of a multiple commercial MBCs for NG sweetening is conducted to assess its intensification potential based on the key performance indicators (KPIs) of an NG sweetening process. Lastly, the work presented in the thesis is summarized in Chapter 6, highlighting the contributions that have been made. Recommendations and directions for future work are also discussed.

Chapter 2 Literature Review

2.1 Membrane Contactor Technology

2.1.1 The principle of membrane contactors

In membrane contactors (MBC), the gas phase is separated from the liquid phase by a microporous hollow-fiber membrane (HFM), and selectivity for separation is provided by the absorption liquid which may be of similar type as in conventional absorption towers (i.e., physical or chemical solvent) (Mansourizadeh and Ismail, 2009; Boributh et al., 2012). The principle of MBC is illustrated in Figure 2.1.

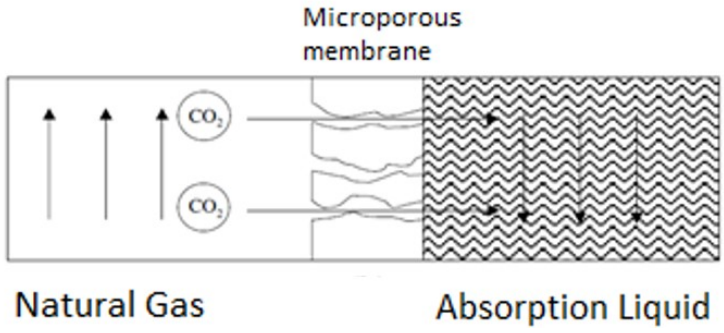

Figure 2.1: Principle of membrane contactor (MBC). Adapted from: (Hoff, 2003).

Hollow fibers are stacked into a membrane module, in order to achieve a very high compaction and therefore exchange area. A hollow-fiber MBC consists of three main sections, namely tube side, membrane side and shell side. Either fluids (i.e., gas or liquid absorbent) can flow in the tube or shell side, in a parallel or cross-flow configuration. An illustration of parallel counter-current flow configurations and pictures of lab scale MBC are shown in Figure 2.2 and 2.3.

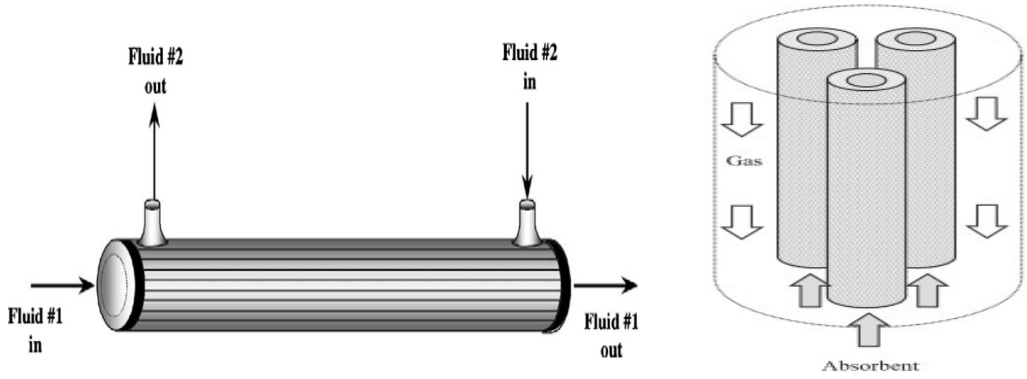

Figure 2.2: Schematic diagram of the parallel flow in horizontal (left) and vertical (right) MBC operation (Sohrabi et al., 2011; Rongwong et al., 2012).

Figure 2.3: Lab scale membrane contactors of various sizes.

2.1.2 Advantages and drawbacks of membrane contactors

This subsection presents the benefits of MBC that have been reported in the literature.

Economics from Process Intensification. Due to microporous and small diameters of HFM, MBC can provide up to 30 times higher contact area per unit volume compared to conventional columns as shown in Table 2.1 (Hoff et al., 2004; Mansourizadeh and Ismail, 2009; Rongwong et al., 2012; Hoff and Svendsen, 2013).

Table 2.0-1: Specific surface area for typical contactors (Mansourizadeh and Ismail, 2009).

Contactor	Specific surface area (m^2/m^3)
Free dispersion column	1–10
Packed column	100–800
Mechanically agitated column	50–150
Membrane contactor	1500–3000

Therefore, compact MBC units can be designed which result in significant savings in weight, volume, and footprint, hence better economically. Falk-Pedersen and Dannström (1997) reported that MBC could lead to a reduction by circa (ca.) 70% in size and ca. 88% in weight compared to conventional columns for CO_2 separation. Likewise, Hoff and Svendsen (2013) reported that a reduction in 75% of absorber size could be achieved for CO_2 removal from natural gas compared to a conventional packed column. These advantages enable the application of MBC to space-constrained environments, such as on offshore or floating liquid natural gas (FLNG). Also, mist-eliminator/demister which are used in conventional gas-liquid

contactors can be omitted in MBC since the gas and liquid do not disperse to one another (Dindore, 2003).

Operational flexibility MBC provides gas and liquid contact without phase dispersion, and the gas and liquid flowrates can be varied independently, unlike conventional packed and spray towers. The decoupling between gas and liquid phases prevents any momentum transfer from occurring across the phase boundary. As a consequence, the operational challenges faced by conventional absorption towers, such as foaming, channelling, entrainment and flooding, are eliminated (Li and Chen, 2005). MBC can furthermore also operate in horizontal or vertical orientation as described in Chapter 3 (Sec. 3.1) and Chapter 4 (Sec. 4.3).

Linear scale up Modular MBC can be designed whereby the diameter, length and number of fibers are fixed, thus having a constant interfacial area per module. This modularity of membrane modules simplifies the fabrication, design and enable a linear scale-up (Li and Chen, 2005) as described in Chapter 5 (Sec 5.6).

On the other hand, MBC has possible disadvantages as the membrane itself provides resistance to mass transfer. It can be said that the extra resistance from the microporous membrane can be minimized by proper membrane design or combination of membrane and solvent. In addition, due to the small diameter and pore sizes of hollow fibers, gas pre-treatment is required to remove particles, dust and liquid droplet to avoid clogging of the membrane module.

Accurate control of the pressure difference between the liquid and gas, also known as transmembrane pressure is vital in MBC to prevent membrane wetting, unwanted froth, foam and dispersion between the two phases, which ultimately could reduce mass transfer efficiency (Dindore, 2003). MBC may suffer from bypassing and dead zone formations on the shell side which also results in a loss of efficiency (Dindore, 2003). Membranes and the resins potting the membranes may have a considerably lower life span than conventional gas-liquid contactors or their parts (Dindore, 2003). Therefore, suitable and stable membrane material shall be selected to avoid the substantial cost of frequent membrane replacement.

2.1.3 Membrane Materials and Charaterization

In principle, different types of membrane can be used in MBC to separate both contacting phases. Membranes used in MBC are classified into two groups namely, organic (*i.e.* polymeric) and inorganic membranes (Mansourizadeh and Ismail, 2009). Polymeric membranes are mostly used in MBC research and development due to the possibility to modify their intrinsic properties, such as thermal, mechanical and porosity by a surface modification which can be carried out through different techniques such as photochemical modification, coating, etc. (Membrane Science & Technology, 2005; Mansourizadeh and Ismail, 2009). Examples of polymeric membranes are polyvinylidene fluoride (PVDF), polytetrafluoroethylene (PTFE), polyethylene (PE), polypropylene (PP), polysulfone (PS) and polyetheretherketone (PEEK). It can be said that PTFE, PVDF, and PP have similar properties and that they exhibit good to excellent thermal and chemical stability (Mansourizadeh and Ismail, 2009).

Thermal stability is an important parameter to ensure that the membrane material will not degrade or decompose under high temperatures. Change in the membrane material depends on the glass transition temperature, T_g , whereby higher T_g can enhance both its chemical and thermal stability (Mansourizadeh and Ismail, 2009). Table 2.2 shows the glass transition temperatures for commonly used polymers in gas absorption MBC.

Table 2.0-2: Glass transition temperature, T_g of selected polymers (Mansourizadeh and Ismail, 2009).

Polymer	T_g (deg C)
Polytetrafluoroethylene (PTFE)	126
Polypropylene (PP)	-15
Polyethylene (PE)	-120
Polyether sulfone (PES)	230
Polysulfone (PS)	190
Polyvinylidene fluoride (PVDF)	-40
Polyimide (PM)	300

Table 2.2 shows that PE and PP have very low T_g values, which could contribute to the instability and wetting problems, as reported by Kreulen et al. (1993) and Nishikawa et al. (1995). PTFE has a much higher T_g compared to PE and PP, which contributes to its higher stability. For NG sweetening, a membrane with moderate T_g can be selected as the separation can be carried out near ambient temperatures. On the other hand, a membrane with high T_g (possibly over 100°C) should be selected for CO_2 capture from flue gases which are typically emitted at high temperatures. (Mansourizadeh and Ismail, 2009).

PE, PP, and PTFE present a high chemical resistance and are usually manufactured by stretching and thermal methods as they cannot be dissolved in any common solvent. Therefore, relatively low porosity membranes are fabricated which limit the absorption flux (Mansourizadeh and Ismail, 2009).

PVDF is soluble in aprotic solvents such as dimethylformamide (DMF), dimethylacetamide (DAMC) and triethylphosphate (TEP). It is prepared via phase-inversion method and can provide relatively higher porosity membrane (Mansourizadeh and Ismail, 2009). Therefore, researchers have shown great interest in the preparation of PVDF and modified PVDF membranes for various membrane-based separation applications such as gas absorption MBC, membrane distillation and pervaporation (Deshmukh and Li, 1998; Wang et al., 2000; Yeow et al., 2004).

The choice of membrane material is driven not only by the thermal and chemical properties but also by the hydrophobicity of the material. PTFE, PP, PVDF, and PE are all polymers with high hydrophobicity and low surface energies (Dindore, 2003). Polymers with low surface energy will have a higher resistance towards wetting by the liquid solution. And when the material is hydrophobic, water cannot wet the membranes spontaneously (Mansourizadeh and Ismail, 2009). Table 2.3 below shows the surface energy of selected polymers that can be used in MBC.

Table 2.0-3: Surface energies of polymer materials (Mulder, 1996).

Polymer	Surface energy mN/m
Polytetraflouroethylene (PTFE)	19.1
Polytriflouroethylene	23.9
Polypropylene	30.0
Polyvinylideneflouride	30.3
Polyethylene	33.2

It can be seen that PTFE has significantly lower surface energy than other polymers. It was reported in various researches that PTFE membrane has high resistance to wetting after long hours of operation (Nishikawa et al., 1995; Falk-Pedersen and Dannström, 1997; deMontigny et al., 2006; Chan et al., 2013). A study by Falk-Pedersen and Dannström (1997) reported that PTFE is the only suitable membrane for use with alkanolamines. Nishikawa et al. (1995) also found PTFE to be chemically stable, have a high degree of hydrophobicity, and be effective for more than 6600 hours when CO_2 removal experiments were conducted with alkanolamine. On the other hand, Kreulen et al. (1993), Nishikawa et al. (1995), deMontigny et al. (2006), and Chan et al. (2013), reported that tests with CO_2 absorption into alkanolamine using PS, PVDF, PE, and PP membranes have shown a deterioration of the resistance to liquid penetration after a long period of operation. This is probably due to a combination of surface wetting and/or swelling of the polymer with time. Meyer et al. (2010) reported that super-hydrophobic PEEK membranes developed by GTI and PoroGen are compatible with alkanolamines to remove CO_2 based on laboratory tests.

Inorganic membranes such as ceramic membrane with better chemical and thermal stability and high mechanical strength, could be used as an alternative. However, these membranes are hydrophilic due to the presence of hydroxyl group (–OH) in the ceramic material. As a result, membrane surface modification is required to improve their hydrophobicity. This property is considered to be a disadvantage as membrane wetting creates additional membrane resistance for CO_2 mass transfer (Mansourizadeh and Ismail, 2009).

Relevant structural properties of a membrane consist of its thickness, pore size distribution, porosity, and tortuosity. A typical membrane is prepared from hydrophobic polymer materials with high porosity, inner diameter (ID) in the range of 200-1000 microns, outer diameter (OD) in the range 300-2000 microns, membrane thickness between 10-300 micron, pore sizes in the range of 0.1 to 1 micron and tortuosity in the range of 4-5 (Mansourizadeh and Ismail, 2009). Table 2.4 shows the typical characteristics of hollow fiber membranes used in MBC.

Table 2.0-4: Characteristics of hollow fiber used in MBC (Mansourizadeh and Ismail, 2009).

Membrane	ID (μm)	OD (μm)	Pore Size (μm)	Porosity%	Process
Polysulfone(PS)	200	400	0.05	–	SO_2 absorption with NaOH, Na_2CO_3, Na_2SO_3 and $NaHCO_3$ solutions
Polysulfone(PS)	560	880	0.102	–	H_2S absorption with NaOH solution
Polyethersulfone(PES)	460	850	–	–	H_2S absorption with NaOH solution
Polyethylene(PE)	482	706	–	0.82	CO_2 absorption with MEA solution
Polytetrafluoroethylene (PTFE)	1000	1700	–	0.40	CO_2 absorption with MEA solution
PP	600	1000	0.265	0.79	CO_2 absorption with CORAL 20 solution
PP	270	300	0.015	0.30	CO_2 absorption with water, DEA and NaOH solutions
PP	344	442	0.02–0.2	>0.45	CO_2 absorption with PG, MEA and MDEA solutions
Poly(vinylidene fluoride) (PVDF)	300	514	–	0.698	CO_2 absorption with pure water
PVDF	607	907	0.04	–	H_2S and CO_2 absorption with Na_2CO_3 solution
PP	244	300	–	0.35	CO_2 absorption with MEA and AMP
PTFE	1000	2000	–	0.50	CO_2 absorption with MEA and AMP

2.1.4 Mode of Operation and Breakthrough pressure

In principle, the mass transfer processes in a membrane contactor are three-fold, namely transfer from the gas phase to the membrane surface, transfer within the membrane pores, and lastly transfer from the liquid interface to the liquid bulk as shown in Figure 2.4 below.

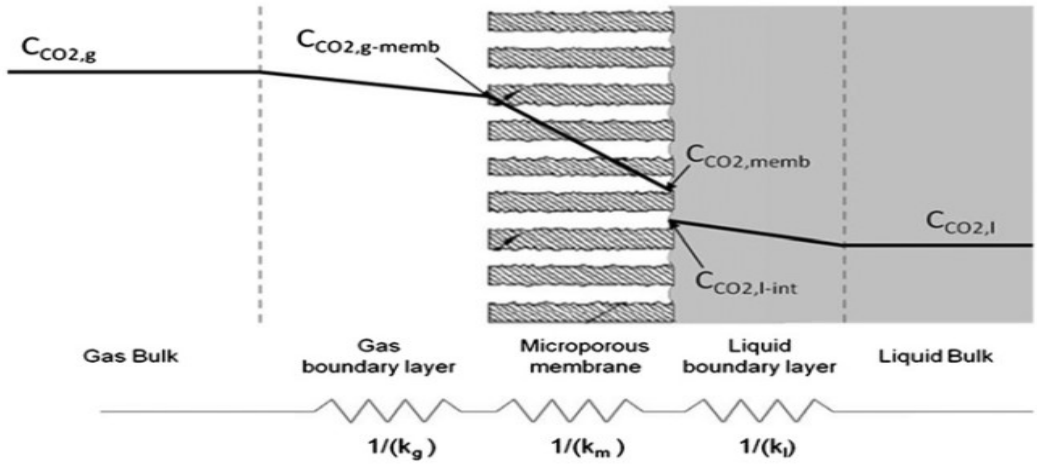

Figure 2.4: Schematic representation of mass transfer resistance in MBC (Chabanon et al., 2013).

Additionally, hydrophobic membranes can be wetted by organic solvents, either partially or fully. It is known that the operation of MBC can be classified into three modes, namely non-wetted (dry), partially wetted, and fully-wetted, as illustrated in Figure 2.5.

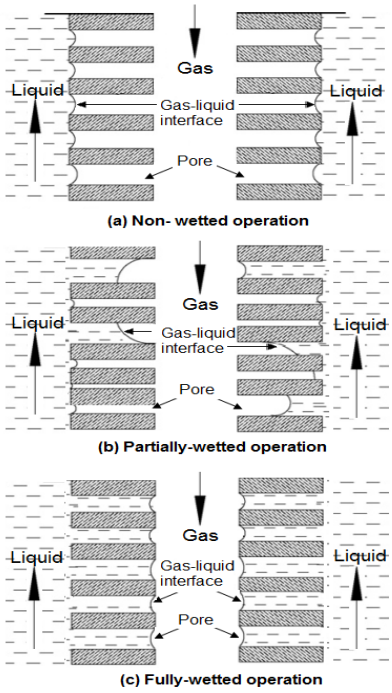

Figure 2.5: Different degrees of membrane wetting in MBC operation. Adapted from: Lu et al., (2008).

The non-wetted mode of MBC operation (Fig. 2.5a) is preferred since it presents a higher CO_2 absorption rate, while partially- or fully-wetted membranes (Fig. 2.5 b,c) can decrease the mass-transfer flux quite drastically, mainly due to a lower liquid diffusivity in the wetted membrane phase. For instance, Zhang et al. (2008) revealed that when the membrane was wetted by only 10% of its thickness, the ratio of the individual membrane resistance to overall mass transfer resistance increased sharply from 10% to 70%. Many researchers have reported the adverse effects of membrane wetting on process performance (Wang et al., 2005; Mavroudi et al., 2006; Lu et al., 2008; Khaisri et al., 2010; Cui et al.,2015).

In principle, membrane wetting could be prevented by keeping the transmembrane pressure difference below the breakthrough pressure, but partial-wetting may still occur in practice due to non-uniform membrane pore-sizes, with bigger pores being more easily wetted. Many factors are known to affect the degree of wetting, including the membrane properties and various operating parameters, such as the inlet liquid pressure, liquid velocity, liquid temperature, and amine concentrations (Lu et al., 2008; Mosadegh-Sedghi et al., 2012; Boributh et al., 2012; Rongwong et al., 2015). Moreover, the variation in liquid pressure along

the length of the HFM can affect membrane wetting considerably, e.g. due to pressure drops or the static head in a vertical MBC.

In partially-wetted operations, a hydrophobic membrane with a non-uniform pore size distribution exhibits a range of breakthrough pressures, with larger pores filled first, followed by smaller ones. According to the Laplace-Young equation, a pore is wetted when the transmembrane pressure difference ΔP_{TMPD} , is greater than the breakthrough pressure, ΔP_{c} given by

$$\Delta P_{\mathrm{c}}(\delta) = \frac{-2\,\gamma \cos\theta}{\delta} \tag{2.1}$$

where δ [m] denotes the pore radius; γ [N m^{-1}], the surface tension of the liquid phase; and θ [rad], the contact angle of the liquid on the membrane.

The transmembrane pressure is defined as the difference between the pressures in the liquid and gas phases, P_{l} and P_{g} [Pa], which is described in detail from Eq. (3.4) in Sec. 3.2.1.

It can be seen from Eq. (2.1) that a higher breakthrough pressure may be achieved by using solvents with high surface tension, reducing the pore size or increasing the contact angle. The desired situation is to operate at $\Delta P_{\mathrm{c}} > \Delta P_{\mathrm{TMPD}} > 0$ along the MBC to prevent membrane wetting. It should be noted that if $\Delta P_{\mathrm{TMPD}} < 0$, then gas bubbles will penetrate into the liquid phase, leading to large hydrocarbon loss. Therefore, it is common to operate at a slightly higher liquid pressure than gas pressure, $\Delta P_{\mathrm{TMPD}} > 0$ while remaining below ΔP_{c} to avoid gas bubble formation into the liquid phase (Kang et al., 2017).

Most solvents used for bulk CO_2 removal are organic and have relatively low surface tensions compared to water. These solvents may contain ionic species, complexes, or other impurities which that change the wetting characteristics of the membrane-liquid system.

It is reported that prolonged direct contact of the polymeric membrane surface with the solvent can lead to morphological change and gradual membrane wetting (Wang et al., 2004; Dahlquist et al., 2010). Hence, ensuring long-term stability and maintaining the gas removal efficiency requires a careful combination of solvent and membrane material.

2.1.5 Screening of Membrane-Solvent Combination

The critical parameters for solvent selection are the solubility of acid gases, thermal stability, non-toxicity, low vapour pressure, easy regenerability and commercial availability at low cost (Dindore, 2003; Mansourizadeh and Ismail, 2009). In addition, a solvent with low viscosity is preferred to avoid high-pressure drops along the fibers while a high viscous solution also reduces the mass transfer rates resulting into an increase in membrane area requirement. Table 2.5 outlines the properties and CO_2 solubility in terms of the distribution coefficient for various commercially available physical solvents used in CO_2 absorption processes using conventional contactors.

Table 2.0-5: Physical solvents for CO_2 absorption (at T=298K)(Dindore, 2003).

	Solvent	CO_2 solubility m#	Surface Tension mN/m	Viscosity cP	Selectivity CO_2/CH_4	Vapor Pressure Pa
1	Propylene Carbonate	3.50	41.5	2.5	26.31	11.33
2	Selexol	3.60	33.5	5.8	14.92	0.097
3	N-methyl pyrrodilone	4.56	34.4	1.7	13.88	53.33
4	Dimethyl formamide	4.86	30.2	0.8	-	-
5	Tributyl phosphate	2.50	27.5	3.4	25.00	-
6	Glycerol triacetate	3.70	35.8	3.5	20.55	0.13
7	n-Formyl morpholine	3.15	49.1	6.7	-	869.31
8	water	0.82	72.3	1.0	23.5	3167.20

$m = (C_L / C_G)_{equilibrium}$

For membrane selection, the initial screening is based on the hydrophobicity of the membrane. Membranes having a high hydrophobicity and low surface energy such as PTFE, PP, PVDF, PS, and polyethersulfone (PES) are suitable. Some research has been conducted on the compatibility of membranes and solvents (Kamo et al., 1992; Barbe et al., 2000; Khaisri et al., 2009; Chan et al., 2013). Dindore (2003) performed stability testing on several membranes and by keeping them in contact with different solvents over a period of time. Then, the membranes were investigated for the immediate spreading of a solvent and the damage caused by that solvent to the membrane. Table 2.6 shows their results in terms of compatibility between solvent and membrane material.

Table 2.0-6: Membrane-solvent compatibility (Dindore, 2003).

Solvent	PTFE	PP	PVDF	PES	PS
Water	√	√	√	√	√
Propylene Carbonate	√	√	x	x	x
Selexol	√	x	x	x	x
N-methylpyrrodilone	x	x	x	x	x
Dimethyl formamide	x	x	x	x	x
Tributyl phosphate	x	x	x	x	x
Glycerol triacetate	√	x	x	x	x
n-Formyl morpholine	√	√	x	x	x

√ = compatible combination x = incompatible combination

Only PTFE and PP membranes were found to be compatible with certain solvents. The rest of the membranes showed incompatibility with the selected solvents chosen in terms of morphological damage, swelling, shrinkages, color change or dissolution (Dindore, 2003).

Chan et al. (2013) reported that PTFE, PVDF, and PS are stable with alkanolamine such as activated MDEA. They characterized the diameter, thickness, porosity, pore sizes, contact angle and liquid entry pressure of these three membranes after immersion in activated MDEA. They also reported that, even though the contact angles of membranes remain unchanged after immersion in activated MDEA, PS could be wetted in activated MDEA after a few days while PVDF was more resistant to wetting. In addition, PTFE was found to be highly resistant to wetting even after immersion in activated MDEA solution during one month, making it suitable for long term operation in MBC. Nishikawa et al. (1995), Falk-Pedersen and Dannström, (1997), deMontigny et al. (2006) and Chan et al. (2013) also reported that PTFE maintained CO_2 removal performance after a prolonged period of operation (i.e. more than 85 hours) with alkanolamines, while other membranes suffered a loss in performance over the same period. Likewise, Khaisri et al. (2009) had reported that PTFE membranes maintained their absorption performance, while PVDF membranes did not maintain their absorption performance over the same operation period.

2.1.6 Module Configurations and Flow Patterns in MBC Modules

2.1.6.1 Types of Membrane Contactor

A successful MBC process design does not only consider membrane chemistry and structure, but also module configuration (i.e., type and design/geometry) and flow pattern. Conventional membrane module configurations can be adopted for gas-liquid MBC, which are generally classified into two types, namely i) flat sheet MBC and ii) tubular MBC. Flat sheet membranes are used in plate-and-frame or in spiral wound MBC, whereas tubular membranes are used in hollow fiber membrane and coiled tubular membrane configurations. The basic principle governing a module design is to achieve the largest possible membrane surface area per unit volume (i.e specific surface area). However, additional criteria are considered, such as the type of separation, ease of operation, size of each unit, maintenance and cleaning requirements as well as the cost. The characteristics of all module designs are compared in Table 2.7.

Table 2.0-7: Qualitative comparison of various membrane configurations (Constantinou, 2011).

	Tubular	Plate-and-frame	Spiral-wound	Capillary	Hollow fiber
Packing density	Low	– – – – – – – – – – – – →			Very high
Investment	High	– – – – – – – – – – – – →			Low
Fouling tendency	Low	– – – – – – – – – – – – →			Very high
Cleaning	Good	– – – – – – – – – – – – →			Poor
Membrane replacement	Yes/no	Yes	No	No	No

A hollow-fiber membrane module is a bundle of porous hollow fibers packed in parallel alignment into a shell, similar in configuration to a shell and tube heat exchanger as shown in Figures 2.2 and 2.3. Hollow-fiber membrane contactors are widely used due to higher interfacial area compared to flat sheet membranes, and have been extensively used in gas-liquid or liquid-liquid separation processes, such as gas absorption/stripping, extraction and membrane distillation. (Mansourizadeh and Ismail, 2009; Constantinou, 2011). The fibers are packed randomly on the shell side which may lead to non-uniform fiber distribution. As a result, it may cause severe uneven flow distribution due to fluid channeling and bypassing on the shell side, that lead to a decrease in mass transfer. The small fiber internal diameter can

also limit mass transfer at the lumen side. Much research has been conducted to improve features such as the homogeneity of fibers, packing density and the relative flow directions, i.e., co-currently and counter currently, and cross-flows of the two phases (Mansourizadeh and Ismail, 2009).

The remainder of this subsection discusses three types of hollow fiber membrane contactors, namely longitudinal (parallel), cross flow and coiled modules.

2.1.6.2 Longitudinal Modules

In longitudinal modules, the gas and liquid phases flow parallel (either co-currently or counter-currently) to each other on the opposite sides of the fibers. A schematic diagram of this type of module is given in Figure 2.6.

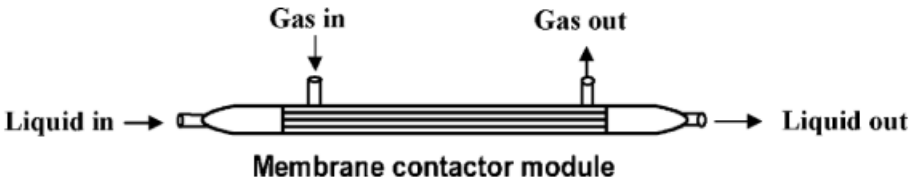

Figure 2.6: A parallel-flow hollow fiber MBC in co-current operation (Mansourizadeh and Ismail, 2009).

Much research on membrane gas absorption has been conducted at the laboratory scale on this type of membrane module (Nishikawa et al., 1995; Falk-Pedersen and Dannström, 1997; Lu et al., 2005; Boributh et al., 2012; Chan et al., 2013; Kang et al., 2017). The simplicity of their manufacturing, well-known fluid dynamics in shell and tube side, and relatively easy mass transfer estimation are the main advantages of this module. On the other hand, its main drawback is a lower efficiency in mass transfer compared with the cross-flow module (Mansourizadeh and Ismail, 2009). The choice between co-current and counter-current operation is determined by the variation in transmembrane pressure, ΔP_{TMPD} along the hollow fiber membrane. It is known that the countercurrent process leads to a higher variation in ΔP_{TMPD}, which can lead to partial membrane wetting and reduced mass transfer rates if the breakthrough pressure, ΔP_c is low. If the variation of transmembrane pressure ΔP_{TMPD} is lower

than breakthrough pressure $\Delta P_{c,}$ then counter-current is preferred as it offers higher average concentration driving force compared to co-current and is preferred in situations where membrane or fiber-side mass transfer resistance dominates (Wang and Cussler, 1993). In the case of parallel flow, the overall mass transfer rate can be significantly reduced if the shell-side mass transfer resistance is significant. In such instances cross flow configurations are attractive as flow in the direction perpendicular to the fibers leads to higher shell-side mass transfer coefficients. This is mainly due to the concentration boundary layer breaking up via continuous splitting and remixing of the fluid flowing perpendicular to the fiber.

2.1.6.3 Cross-Flow Modules

In cross-flow modules, the flow of one of the fluids is perpendicular to the axis of the fiber, and the other fluid flows parallel to the axis of the fiber. Therefore, the two fluids flow at right angles/normal to each other. A schematic diagram of this type of module is given in Figure 2.7.

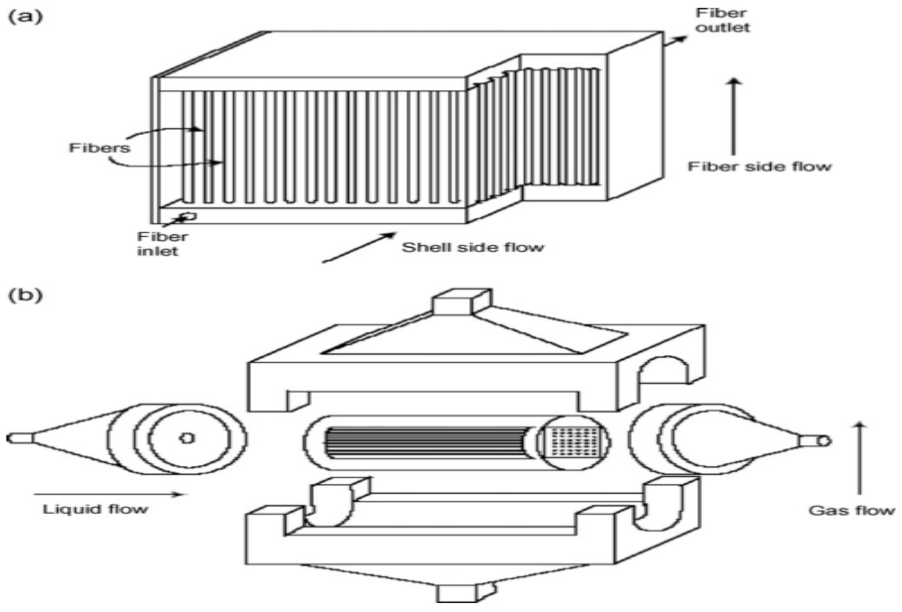

Figure 2.7: Cross-flow MBC (a) TNO-MEP (b) Dire and Versteeg (Mansourizadeh and Ismail, 2009).

In general, the cross-flow operation of hollow-fiber membrane contactors is preferred as it offers several advantages such as higher mass transfer coefficients, minimal shell-side channeling and lower shell-side pressure drop compared with parallel flow contactors. Dindore

and Versteeg (2005) carried out experiments to study the effect of various parameters, including gas and liquid flow rates, and solute concentration in the feed stream, on the CO_2 removal performance using water in a rectangular cross-flow gas-liquid membrane contactor. It should be noted that the analysis of a cross-flow membrane contactor is complicated due to the change in concentrations of both phases in the flow direction as well as in the direction perpendicular to the flow (Dindore and Versteeg, 2005).

2.1.6.4 Coiled Modules

Coiled modules have attracted attention in ultrafiltration and nanofiltration membrane applications (Mansourizadeh and Ismail, 2009). The curved channels of the hollow-fiber membranes are used to create secondary flow (Dean Vortices) in the fluid within the tube, which promotes fluid mixing and therefore improve mass transfer. A schematic diagram of this type of module is given in Figure 2.8.

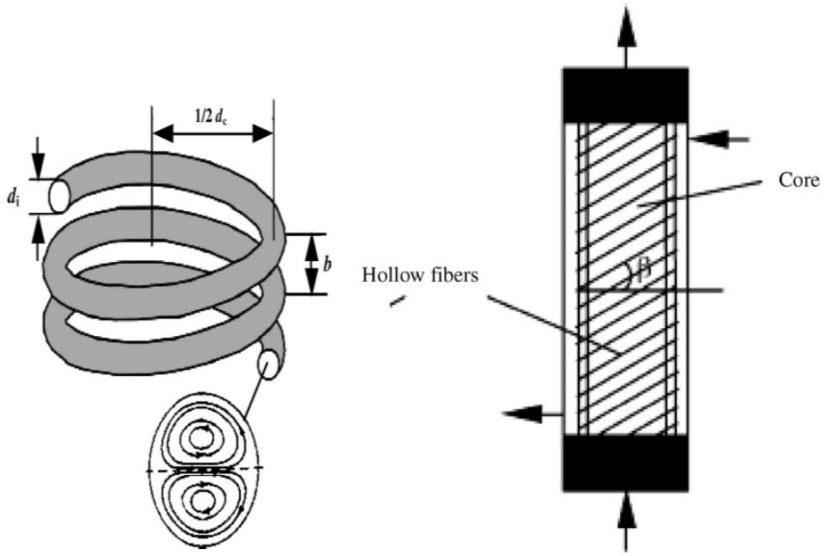

Figure 2.8: Schematic representation of a coiled module (Liu, Li, Ding, et al., 2005).

A critical advantage of coiled modules over other techniques is their capability to simultaneous improve mass transfer at both the lumen and shell sides (Liu et al., 2005). Liu et al. (2005) examined mass transfer performances for stripping dissolved oxygen from water in coiled hollow-fiber membrane modules. They found that, compared with the conventional straight

module, the mass transfer at both tube and shell sides of the coiled hollow-fiber module were doubled. These improvements can be attributed to the created secondary flows (known as Dean Vortices) inside the coiled fibers and the extra turbulence at the shell side. Moulin et al. (1996) investigated a helically wound hollow-fiber membrane module in an oxygenation operation with water flowing in the laminar regime inside the tube. They compared it with a conventional module with straight hollow-fiber membranes aligned in parallel. They showed that the presence of vortices can improve the mass transfer rate by a factor of 2–4. Therefore, coiled module can be considered as an alternative to improve mass transfer in hollow fiber membrane contactors. However, few studies have been devoted to this type of modules so far.

2.2 Mathematical Modeling of Membrane Contactor

Mathematical models provide an effective tool to help understand the CO_2 removal mechanisms in MBC, and thus enable a better assessment and optimization of their performance. They can be used to investigate the acid gas absorption mechanisms and the impact of various parameters, such as the membrane's physical properties/characteristics, operating parameters, and flow configurations. In turn, systematic optimization and scale-up studies can be conducted to determine design options for superior CO_2 removal performance in MBC.

A large number of publications on modeling of MBC for CO_2 capture have reported a good agreement of the model results with experimental data, even though different modeling strategies were adopted. (Zhang Qi and Cussler, 1985a, 1985b; Malek et al., 1997; Wang et al., 2004; Hoff et al., 2004; Lu et al., 2005; M. Al-Marzouqi et al., 2008; Keshavarz et al., 2008; Khaisri et al., 2010; Faiz, El-Naas and Al-Marzouqi, 2011; Eslami et al., 2011; Boucif et al., 2012; Chabanon et al., 2013; Boucif et al., 2015; Goyal et al., 2015). Chabanon et al. (2013) conducted a comparison of different modeling approaches for CO_2 absorption with MBC, from the simplest constant K_L to the more complex 2D model, where they adjusted single parameter, namely the membrane mass transfer coefficient k_m. Table 2.8 summarizes the main types of modeling strategies and corresponding assumptions for a hollow fiber MBC in parallel counter-current flow configuration.

Table 2.0-1: Overview of different types of modeling strategies reported in the literature and corresponding assumptions.

Modeling strategy	Assumptions	References
Constant overall mass transfer model	1. Plug flow for the gas phase in the membrane contactor. 2. Constant gas velocity in the axial direction. 3. Negligible CO_2 concentration in the liquid phase. 4. Isothermal conditions and steady state. 5. Negligible pressure drop in gas phase. 6. Adjustable overall mass transfer coefficient or membrane mass transfer coefficient.	(Zhang Qi and Cussler, 1985a; Wickramasinghe et al., 1992; Bottino et al., 2008; Chabanon et al., 2013)
2D model with gas-liquid equilibrium	1. 2D modeling of the gas and liquid phases. 2. Cylindrical geometry. 3. Ideal gas behaviour. 4. Account for axial and radial diffusions in both phases. 5. Negligible convective mass transfer in membrane pores because of small pore size. 6. Isothermal conditions and steady state. 7. Laminar liquid and gas flow with fully developed velocity profiles. 8. Constant physical properties. 9. Henry's law describing the gas-liquid equilibrium. 10. Non-wetted membrane, all except Al-Marzouqi et al. (2008), Faiz and Al-Marzouqi (2010) and Goyal et al. (2015) who consider partially wetted membranes. 11. Constant gas velocities along the axial direction for diluted system, all except Faiz et al. (2011) who consider a concentrated system.	(Al-Marzouqi et al., 2008; Faiz and Al-Marzouqi, 2010; Faiz et al., 2011;Eslami et al., 2011; Chabanon et al., 2013; Goyal et al., 2015)
2D model with mass transfer coefficient	1. 2D modeling in gas or liquid phase. 2. Mass transfer based on resistance in series concept. 3. Cylindrical geometry. 4. Steady state. 5. Ideal gas behaviour.	(Hoff et al., 2004; Wang et al., 2004;

	6. Account for axial and radial diffusions, all except Hoff et al. (2004) and Boucif et al. (2015) who neglect axial diffusion. 7. Isothermal conditions, all except Hoff et al. (2004). 8. Laminar liquid and gas flow with fully developed velocity profiles, all except Hoff et al. (2004) and Boucif et al. (2015). 9. Constant physical properties, all except Hoff et al. (2004) and Boucif et al. (2015). 10. Henry's law describing the gas-liquid equilibrium. 11. Consider partially wetted membranes. 12. Constant gas velocities along the axial direction for a diluted system.	Lu et al., 2005; Keshavarz et al., 2008; Boucif et al., 2012; Boucif et al., 2015)

Almost all investigations were performed assuming liquid feed with fresh lean solvent and isothermal conditions, except Hoff et al. (2004) who included initially loaded solutions and accounted for temperature variations, leading to varying physicochemical properties. The study revealed that the primary mass transfer resistance was located in the liquid phase. Recently, Hoff and Svendsen (2013) made several improvements to their 2D model in a liquid phase by using better thermodynamic models for the MEA and MDEA based systems, and better models of the gas and liquid side pressure drops. Keshavarz et al. (2008) and Al-Marzouqi et al. (2008) took into account the influence of partial membrane wetting for CO_2 absorption using alkanolamines. They concluded that membrane wetting, even at very low fractions, can decrease the absorption flux significantly. Boucif et al. (2012) proposed a 2D model where the velocity is characterized by Navier–Stokes momentum conservation equations and complex reaction kinetic models are used in the liquid phase. Their results indicated that the performance is dependent on the gas velocity and the module geometry. It should be said that many papers present model validation using experimental data for binary mixtures of CO_2/N_2 or CO_2/CH_4, from laboratory-scale modules at atmospheric pressure except Faiz and Al-Marzouqi (2010) who perfomed the experiments up to 50 bar. All three modeling approaches outlined in Table 2.8 will now be detailed in the following subsections.

2.2.1 Constant overall mass transfer coefficient models

Early publications (Zhang Qi and Cussler, 1985a; Wickramasinghe et al., 1992; Bottino et al., 2008) considered a constant overall mass transfer coefficient K_{L}, which is a function of different mass transfer coefficients. Based on the assumptions listed in Table 2.8, a CO_2 mass balance on the gas phase can be expressed as

$$v_{\mathrm{g}} \frac{dC_{\mathrm{CO_2}}}{dz} = -K_{\mathrm{L}} a C_{\mathrm{CO_2}} \tag{2.2}$$

where v_{g} is the gas velocity (m s^{-1}); $C_{\mathrm{CO_2}}$, the CO_2 concentration in the gas phase [mol m^{-3}]; K_L, the overall mass transfer coefficient (m s^{-1}), which is assumed to be constant; a, the specific interfacial area (m^{-1}); and z, the axial contactor coordinate (m). For a membrane contactor of length L [m], the CO_2 capture ratio after integration can be expressed (Chabanon et al., 2013), as

$$\eta = 1 - \exp\left(\frac{-K_{\mathrm{L}} a L}{v_{\mathrm{g}}}\right) \tag{2.3}$$

The term $K_{\mathrm{L}} a$ [s^{-1}] is one of the key process performance parameter used to compare between different gas absorption technologies (Chabanon et al., 2013). When capture ratio, η and gas velocity, v_{g} are experimentally determined, K_{L} is the only unknown being used to fit the data. This model is advantageous as it enables process performances to be quickly assessed, but, it lacks details on the three different mass transfer domains such as the mass transfer coefficients for the gas, membrane and, liquid, respectively.

2.2.1.1 Mass transfer coefficient model

The overall mass transfer considers the three different mass transfer regions as shown in Figure 2.4. A resistance in series model can be used to describe the gas absorption into the solvent as:

$$\frac{1}{K_{\mathrm{L}}} = \frac{1}{k_{\mathrm{l}}} + \frac{1}{k_{\mathrm{m}}} + \frac{1}{k_{\mathrm{g}}} \tag{2.4}$$

where K_L is the overall mass transfer coefficient and k_l, k_m, and k_g are the mass transfer coefficients of liquid, membrane and gas in [m s^{-1}], respectively. At equilibrium, the CO_2 mass transfer flux, J_{CO_2} [mol m^{-2} s^{-1}] for a non-wetted mode is given as:

$$\begin{aligned} J_{CO_2} &= k_g\left(C_{CO_2,g} - C_{CO_2,g,m}\right) \\ &= k_m\left(C_{CO_2,g,m} - C_{CO_2,l,eq}\right) \\ &= k_l\left(C_{CO_2,l,eq} - C_{CO_2,l}\right) \\ &= K_L\left(C_{CO_2,g} - C_{CO_2,l}\right) \end{aligned} \quad (2.5)$$

where $C_{CO_2,l,eq}$ is the CO_2 concentration in liquid phase in equilibrium with the bulk concentration of CO_2 in gas phase.

For chemical absorption, $k_l = k_l^o E$, where E is enhancement factor due to chemical reaction and k_l^o is the physical mass transfer coefficient. The enhancement factor, E can be calculated from Eq (2.6) using the conventional mass-transfer model. Other methods of calculation for E can be found in the literature (van Swaaij and Versteeg, 1992).

$$E = \frac{H_a}{\tanh H_a} \quad (2.6)$$

where the Hatta number, H_a is given by

$$H_a = \frac{\sqrt{k_{ov} D_{i,l}}}{k_l^o} \quad (2.7)$$

For $H_a > 3$, tanh H_a is approaching 1; thus, E is approximately equal to H_a. The reaction of CO_2 with an aqueous solution of MDEA or activated MDEA can be treated as a fast pseudo-first-order reaction (Lu et al., 2005). In Eq. (2.8), k_{ov} is the overall pseudo-first-order reaction rate constant. When MDEA is the absorbent, then:

$$k_{ov} = k_{MDEA} C_{MDEA} \quad (2.8)$$

where C_{MDEA} is the concentration of the solvent and the reaction rate constant, k_{MDEA} is determined as:

$$k_{\mathrm{MDEA}} = 4.01 \times 10^{8} \exp(-\frac{5400}{T}) \tag{2.9}$$

If piperazine (PZ) is used as activator in MDEA, the reaction of CO_2 with PZ can be regarded as the rapid pseudo-first- order reaction that is in parallel with that of CO_2 with MDEA. The k_{ov} is then expressed as:

$$k_{\mathrm{ov}} = k_{\mathrm{MDEA}} C_{\mathrm{MDEA}} + k_{\mathrm{PZ}} C_{\mathrm{PZ}} \tag{2.10}$$

where C_{PZ} is the concentration of piperazine in the solution and the reaction rate constant, k_{PZ} is determined as:

$$k_{\mathrm{PZ}} = 4.49 \times 10^{12} \exp(-\frac{5712}{T}) \tag{2.11}$$

The next paragraphs discuss the individual mass transfer on the membrane, shell side and tube side.

Membrane mass transfer

For a partially wetted membrane, the membrane mass transfer coefficient, k_{m} (Paul et al., 2007; Lu et al., 2008; Mansourizadeh and Ismail, 2009; Boributh et al., 2012) can be calculated by the following equation:

$$\frac{1}{k_{\mathrm{m}}} = \frac{\tau\, r_{\mathrm{dry}}}{D_{\mathrm{CO_2,g}}\, \varepsilon} + \frac{\tau\, r_{\mathrm{w}}}{D_{\mathrm{CO_2,l}}\, \varepsilon} \tag{2.12}$$

where $D_{\mathrm{CO_2,g}}$ and $D_{\mathrm{CO_2,l}}$ are CO_2 diffusion coefficients in the gas and liquid [m^2 s], respectively and where τ , ε are the membrane tortuosity and membrane porosity, respectively. $r_{\mathrm{dry}} = l_m(1-$ ʒ) and $r_{\mathrm{w}} =$ ʒl_m are the dry thickness and wet thickness of the membrane, where the wetting ratio, ʒ is defined as the ratio of pore length wetted by liquid, r_{w}, to the overall pore length/membrane thickness, l_m. Figure 2.9 illustrates partial wetting in a membrane pore.

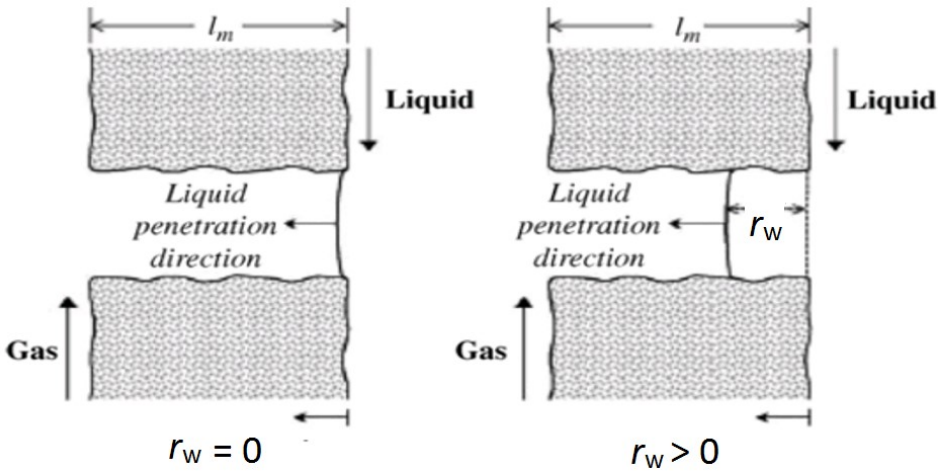

Figure 2.9: Membrane pore partial wetting. Adapted from: Mansourizadeh and Ismail (2009).

If the pore-size distribution of the membrane is known, the value of ʒ can be estimated by incorporating the Laplace equation, Eq. (2.1) into the following equation (Goyal et al., 2015):

$$ʒ(z) = \frac{\int_{-2\gamma cos\theta/\Delta P_{TMPD}}^{\delta_{max}} \delta^2 \, f(\delta) \, d\delta}{\int_0^{\delta_{max}} \delta^2 \, f(\delta) \, d\delta} \tag{2.13}$$

where ΔP_{TMPD} is the transmembrane pressure; γ is the surface tension of the liquid; θ the contact angle between the fluid phase and the membrane ; δ denotes the pore radius; and $f(\delta)$ is the equation of pore size distribution of membrane. Otherwise, the wetting ratio ʒ can be estimated as an adjustable parameter in mathematical model to fit experimental data.

The $D_{CO_2,g}$ can be estimated from empirical correlations based on kinetic gas theory (Bird et al., 1960; Cussler, 2009):

$$D_{CO_2,g} = \frac{T^{1.75}\left(\frac{1}{M_{CO_2}}+\frac{1}{M_{NG}}\right)^{1/2}}{10^5 \, P\left[\left(\sum V_{CO_2}\right)^{1/3}+\left(\sum V_{NG}\right)^{1/3}\right]^2} \tag{2.14}$$

where M_{CO_2} and M_{NG} stand for the molecular weights of CO_2 and NG; and the summations of atomic diffusion volumes for the species of the CO_2-NG gas mixture are taken as $\sum V_{CO_2} = 26.9$ and $\sum V_{NG} = 24.42$.

The $D_{CO_2,l}$ can be also estimated based on the analogy of N_2O diffusivity in solution (Versteeg and Van-Swaaij, 1988):

$$D_{CO_2,l} = D_{N_2O,l} \frac{D_{CO_2,H_2O}}{D_{N_2O,H_2O}} \quad (2.15)$$

Shell-side mass transfer

Shell side mass transfer correlations for hollow fiber modules have been established in a number of studies. One such correlation is in the form of Sh = fn (Re, Sc, ϕ, d_h, L), where Sh is Sherwood number, Re, Sc, ϕ, d_h, L are the Reynolds, Schmidt numbers, packing density, hydraulic meter and module length, respectively. The Sherwood number for shell side is defined by Eq. (2.16a) and Table 2.9 presents mass transfer correlations for parallel and cross flow configurations in shell (Mansourizadeh and Ismail, 2009).

$$\text{Shell side} \quad : \quad \text{Sh} = \frac{k d_h}{D_{i,\text{shell}}} \quad = \quad \text{fn (Re, Sc, } \phi, d_h, L) \quad (2.16a)$$

where k is mass transfer coefficient [m s^{-1}], $D_{i,\text{shell}}$ is the diffusivity of component i in the shell [m^2 s^{-1}], d_h is the hydraulic diameter [m], $d_h = \frac{d_s^2 - n d_o^2}{N d_o}$ (Li, 2015), where d_s is the module shell diameter, N the number of fiber strands, and d_o the outer diameter of the fibers [m], respectively.

Table 2.0-2: Shell-side mass transfer correlations for hollow fiber membrane modules (Mansourizadeh and Ismail, 2009)

Flow	Correlation	Condition
Parallel	$Sh = 1.25(Re\ d_h/L^*)^{0.93} Sc^{0.33}$	$0.5<Re<500;\ \varphi = 0.03$
	$Sh = 5.85(1-\varphi)(d_h/L)\ Re^{0.6}\ Sc^{0.33}$	$0<Re<500;\ 0.04<\varphi<0.4$
	$Sh = (0.53 - 0.58\varphi)\ Re^{0.53}\ Sc^{0.33}$	$21<Re<324;\ 0.32<\varphi<0.76$
	$Sh = (0.3045\varphi^2 - 0.3421\varphi + 0.0015)\ Re^{0.9}\ Sc^{0.33}$	$32<Re<1287;\ 0.1<\varphi<0.7$
Cross	$Sh = 1.38 Re^{0.34}\ Sc^{0.33}$	$1<Re<25;\ \varphi = 0.7$
	$Sh = 0.90 Re^{0.40}\ Sc^{0.33}$	$1<Re<25;\ \varphi = 0.07$
	$Sh = 0.61 Re^{0.363}\ Sc^{0.333}$	$0.6<Re<49;\ \varphi = 0.003$

* d_h is hydraulic diameter (m) and L is module length (m).

Tube-side mass transfer

The mass transfer coefficient, k on the tube side [m s^{-1}], is mainly determined by the geometry of the MBC and the hydrodynamic conditions. The Sherwood number for tube side is defined by Eq. (2.16b), and an overview of the fiber side mass transfer coefficient correlations are presented in Table 2.10.

$$\text{Tube side : Sh} = \frac{k d_i}{D_{i,\text{tube}}} = \text{fn (Re, Sc, d}_{\text{i}}, L) \quad (2.16b)$$

where d_o the inner diameter of the fibers [m] and $D_{i,\text{tube}}$ is the diffusivity of component i in the tube [m^2 s^{-1}].

Table 2.0-3: Tube-side mass transfer correlations (Dindore, 2003).

Equation	Comment
$Sh = 1.62(Gz)^{0.33}$ Gz > 20 $Sh = 3.67$ Gz < 10	Analogy of theoretical laminar heat transfer flux
$Sh = 1.86(Gz)^{0.33}$ Gz > 100	Analogy of empirical laminar heat transfer flux
$Sh = 1.64(Gz)^{0.33}$ 30 < Gz < 2000	Empirical equation for gas-liquid absorption in hollow fiber module.
$Sh = 1.5(Gz)^{0.33}$	Empirical equation for liquid-liquid extraction in hollow fiber module.
$Sh = 1.4(Gz)^{0.33}$ 50 < Gz < 1000	Empirical equation for liquid-liquid extraction in hollow fiber.
$Sh = 0.2\,\text{Re}\left(Sc\frac{d_i}{L}\right)^{0.33}$ Gz < 65	Empirical equation for liquid-liquid extraction in hollow fiber module.

$$\text{Where Graetz, Gz} = \frac{d_i}{L}\text{Re. Sc} \quad (2.17)$$

In general, the liquid phase shows significant mass-transfer resistance. Therefore a more detailed investigation such as the 2D model of the CO_2 and solvent concentration profile in liquid provides a better description and understanding of the system (Chabanon et al., 2013).

2.2.2 Two-Dimensional Models

Two-dimensional (2D) models of various complexities have also been proposed by several authors to describe CO_2 absorption in MBC (Al-Marzouqi et al., 2008; Faiz and Al-Marzouqi, 2010; Faiz et al., 2011;Eslami et al., 2011; Chabanon et al., 2013; Goyal et al.,2015). This approach leads to a more complex set of equations as convection and diffusion contributions in both phases as well as reaction contribution in the liquid phase are taken into account in the axial and radial directions. In the 2D approach, a cylindrical representation as shown in Figure 2.10 is used to reflect hollow fiber geometry.

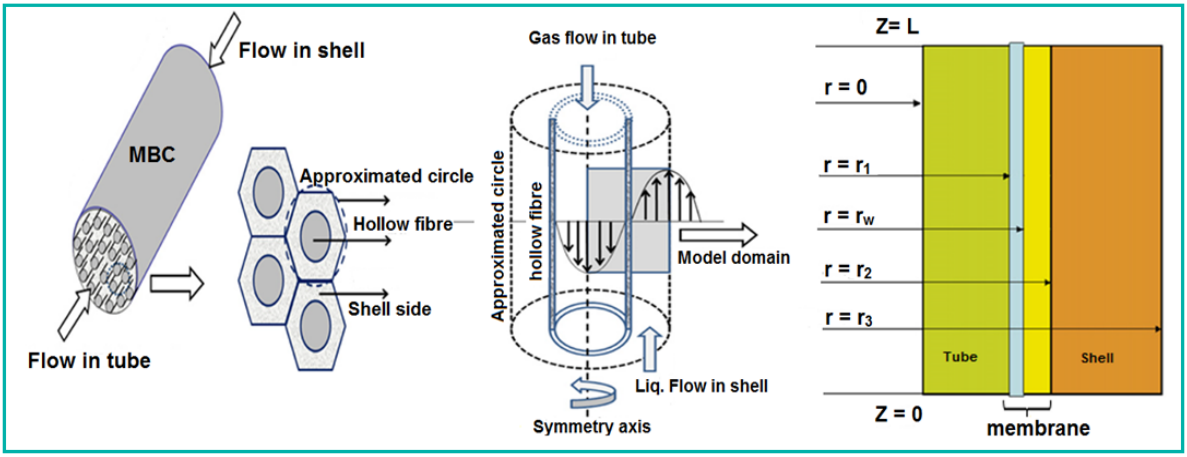

Figure 2.10: Modeling framework for a counter-current, follow fiber MBC module. Left: cylindrical approximation around each fiber. Centre: single piece of hollow fiber. Right: spatial domains in MBC model.

2.2.2.1 Mass-Balance Equations

The model considers the CO_2 concentration gradient in both phases, solvent concentration gradient in the liquid phase, the chemical reaction between CO_2 and solvent in the liquid phase, and the gas velocity changes due to CO_2 absorption for concentrated system.

A common assumption is that the cross-section flows of gas and liquid flowrates are homogeneous at the lumen and shell sides. As such, the concentration profiles in the tubes are all identical, and the model can be developed for a single hollow-fiber. The average fluid velocities in the tube and shell are obtained by dividing the flowrates with the corresponding

cross-section area (Lu et al., 2005; M. Al-Marzouqi et al., 2008; M. H. Al-Marzouqi et al., 2008; Faiz and Al-Marzouqi, 2010; Wang et al., 2013).

For a reactive absorption system, the continuity equation for each species during the simultaneous mass transfer and chemical reaction in terms of molar units can be expressed as:

$$\frac{\partial C_i}{\partial t} = -\nabla . N_i + R_i \tag{2.18}$$

where C_i, N_i, R_i, are the concentration, flux and reaction rate of species *i*, respectively. It should be noted that the molar flux N_i is resultant of two vector quantities:

$$N_i = J_i + C_i V \tag{2.19}$$

where the first term J_i, is molar flux based on Fick's law resulting from the concentration gradient due to diffusion; and the second term, $C_i V$ is the molar flux resulting from the bulk motion of the fluid convection. Fick's Law of Diffusion can be used for the determination of the flux J_i, giving:

$$N_i = -D_i \nabla C_i + C_i V \tag{2.20}$$

where D_i and V are the diffusion coefficient and velocity vector. Combining Eqs. (2.18) and (2.19), leads to the following general equation for mass transfer of species *i*:

$$\frac{\partial C_i}{\partial t} = D_i \nabla^2 C_i - \nabla . C_i V + R_i \tag{2.21}$$

As the hollow fiber membrane contactor system is cylindrical, Eq (2.21) can be written in cylindrical coordinates system as:

$$\frac{\partial C_i}{\partial t} = D_i \left(\frac{\partial^2 C_i}{\partial r^2} + \frac{1}{r}\frac{\partial C_i}{\partial r} + \frac{1}{r^2}\frac{\partial^2 C_i}{\partial \theta^2} + \frac{\partial^2 C_i}{\partial z^2} \right) - \frac{v_r \partial C_i}{\partial r} - \frac{v_\theta}{r}\frac{\partial C_i}{\partial \theta} - \frac{v_z \partial C_i}{\partial z} + R_i \tag{2.22}$$

As it is assumed to be at steady state and not have angular flow, the terms $\frac{\partial C_i}{\partial t}$, $\frac{\partial^2 C_i}{\partial \theta^2}$, $\frac{\partial C_i}{\partial \theta}$, and v_θ are all zero, and Eq (2.22) simplifies to :

$$\frac{v_r \partial C_i}{\partial r} + \frac{v_z \partial C_i}{\partial z} = D_i \left(\frac{\partial^2 C_i}{\partial r^2} + \frac{1}{r} \frac{\partial C_i}{\partial r} + \frac{\partial^2 C_i}{\partial z^2} \right) + R_i \tag{2.23}$$

It should be noted that the velocity terms v_r and v_z represent the bulk and convection flow in the radial and axial direction, respectively. A common assumption for dilute systems, such as gas mixtures containing less than 10% CO_2, is that the bulk flow contribution v_r is negligible. Therefore, the velocity profile in the membrane module solely consists of the convection velocity in the axial direction (Faiz et al., 2011). The resulting general equation for mass transfer for species *i* in hollow fiber MBC can be used to describe the gas, membrane and liquid sections:

$$\frac{v_z \partial C_i}{\partial z} = D_i \left(\frac{\partial^2 C_i}{\partial r^2} + \frac{1}{r} \frac{\partial C_i}{\partial r} + \frac{\partial^2 C_i}{\partial z^2} \right) + R_i \tag{2.24}$$

When partially- or fully-wetted operation is considered, the degree of membrane wetting (or a related parameter r_w, see Figure 2.9) is typically used as a tuning parameter in order for the model predictions to fit given experimental data (Al-Marzouqi et al., 2008; Faiz and Al-Marzouqi, 2010). In recent years, the studies by Boributh et al. (2011) and Goyal et al. (2015) in particular, have exploited knowledge about a membrane's pore-size distribution to predict the degree of wetting in MBC operating at atmospheric pressure.

The mass conservation equations for CO_2 and solvent with chemical reaction in the liquid phase are given by:

$$\frac{v_{z,\mathrm{l}} \partial C_{\mathrm{CO_2,l}}}{\partial z} = D_{\mathrm{CO_2,l}} \left(\frac{\partial^2 C_{\mathrm{CO_2,l}}}{\partial r^2} + \frac{1}{r} \frac{\partial C_{\mathrm{CO_2,l}}}{\partial r} + \frac{\partial^2 C_{\mathrm{CO_2,l}}}{\partial z^2} \right) + R_{\mathrm{CO_2}} \tag{2.25}$$

$$\frac{v_{z,\mathrm{l}} \partial C_{\mathrm{sol,l}}}{\partial z} = D_{\mathrm{sol,l}} \left(\frac{\partial^2 C_{\mathrm{sol,l}}}{\partial r^2} + \frac{1}{r} \frac{\partial C_{\mathrm{sol,l}}}{\partial r} + \frac{\partial^2 C_{\mathrm{sol,l}}}{\partial z^2} \right) + R_{\mathrm{Sol}} \tag{2.26}$$

where $C_{\mathrm{CO_2,l}}$ is the CO_2 concentration in the liquid phase [mol m^{-3}]; $R_{\mathrm{CO_2}}$, the reaction rate of CO_2 with solvent [mol m^{-3} s^{-1}]; $D_{\mathrm{sol,l}}$, is the solvent diffusion coefficient in the liquid phase [m^2 s^{-1}]; and $v_{z,\mathrm{l}}$, the interstitial liquid velocity [m s^{-1}]. In a laminar flow, the fully developed velocity profile in the fibers, $v_{z,\mathrm{tube}}$ can be described as:

$$v_{z,\text{tube}} = 2\bar{v}_{\text{tube}}\left[1 - \left(\frac{r}{r_1}\right)^2\right] \tag{2.27}$$

where $\bar{v}_{\text{tube}}$ and r_1 are the average velocity in the lumen and inner radius of the fiber, respectively. A set of boundary conditions are detailed on Figure 2.11.

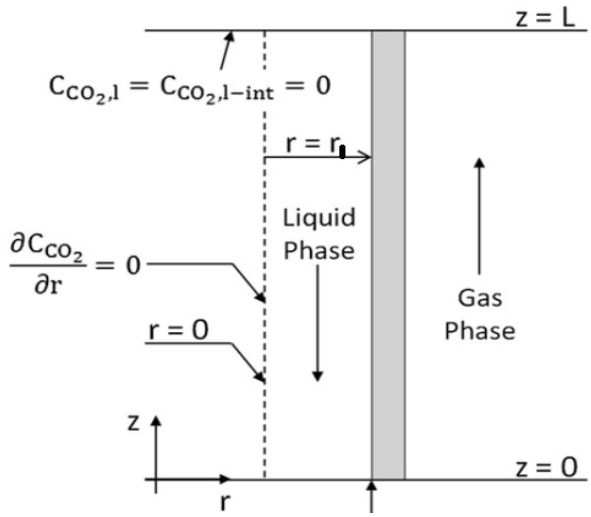

Figure 2.11: Boundary conditions for liquid in tube section (Chabanon et al., 2013).

At the membrane-gas interface $r = r_1$, the flux of CO_2 from the gas phase is equal to the flux of CO_2 into the liquid phase at steady-state. This leads to the following boundary condition:

$$D_{CO_2,l}\frac{\partial C_{CO_2,l}}{\partial r}\bigg|_{r=r_1} = k_{\text{ext}}\left(C_{CO_2,g} - C_{CO_2,g,\text{int}}\right) \tag{2.28}$$

where k_{ext} the external mass transfer coefficient [m s^{-1}] is defined by $1/k_{\text{ext}} = 1/k_g + 1/k_m$ The mass transfer coefficients can be estimated as described in Section 2.2.1.1. In practise, the membrane mass transfer coefficient k_m is often considered as the adjustable parameter.

When equilibrium is attained at the gas-liquid interface, Henry's law gives:

$$C_{CO_2,l,\text{int}} = mC_{CO_2,g,\text{int}} \tag{2.29}$$

where $C_{CO_2,l,\text{int}}$ is the CO_2 concentration at the liquid–membrane interface [mol m^{-3}] and m is the dimensionless distribution coefficient.

2.3 Conclusions

The potential advantages of gas absorption MBC over conventional acid gas removal technologies have been widely recognized. Various experimental and modeling studies have reported on the performance of CO_2 removal using MBC, with a view to better understanding the limitations and promoting the industrial application of MBC technology. Many such studies were conducted using hollow-fiber modules with different membrane types (hydrophobic porous polymers such as PP, PVDF, PTFE) and operating conditions (gas and liquid velocities) with sodium hydroxide or low concentrated carbonates or alkanolamines as the solvent at atmospheric pressure. As far as high-pressure MBC operation is concerned, e.g. for NG sweetening applications, limited studies have been published to date.

Several studies have reported the negative effects of membrane wetting on the MBC performance. Therefore, a suitable membrane-solvent combination that considers the chemical and thermal stability as well as solvent surface tension, contact angle and pore size is paramount. Several studies reported that PTFE exhibits high hydrophobicity, chemical, and thermal stability as evidenced by high CO_2 removal performance in MBC after a prolonged period of operation with alkanolamines. It should be noted that most studies were at the laboratory scale, and very few studies have conducted MBC scale up for industrial applications such as NG sweetening. In view of the technical-commercial requirement to achieve low CO_2 outlet specification and prolonged operation stability, PTFE membrane in combination with alkanolamines as CO_2 absorption liquid seems to be a good choice for membrane-solvent combinations. However, it should be noted that the cost of PTFE membranes in comparison with other membrane materials was not factored into the analysis.

Many lab scale studies were conducted on counter-current longitudinal/parallel MBC due to the simplicity in manufacturing, well-known fluid dynamics in shell and tube side and relative ease of mass transfer estimation. However, other studies have shown that cross-flow modules offer higher mass transfer coefficients, minimal shell side channeling, and lower shell side pressure drop. The mass transfer was also found to double in coiled hollow fiber module compared with longitudinal membrane contactor although limited research has been conducted for this type of module so far.

Throughout this thesis, the longitudinal MBC module with PTFE hollow fiber-alkanolamines solvent operating in the counter-current fluid flow configuration is selected for use in the lab-scale and pilot-scale MBC test rigs.

Mathematical models of MBC of increasing complexity are being applied to understand the CO_2 removal mechanism better and to predict the behavior of the system more accurately. Several numbers of modelling studies of MBC for CO_2 capture have reported a good agreement of the model predictions against experimental data, ranging from a simple constant overall mass transfer coefficient K_L, to sophisticated 2D modelling consisting of convection, diffusion and reaction phenomena.

The assumptions of steady state and isothermal operation are common in these models apart from a few studies that account for the temperature increase due to heat of absorption. Moreover, most studies conducted lab-scale experiments using binary mixtures such as CO_2/N_2 or CO_2/CH_4; experiments with multi-component gas mixtures, (such as natural gas) have not reported to verify the CO_2 absorption performance. None of the work has included water as a transferable component between the gas and the liquid phase.

Finally, no commercial CO_2-removal process from natural gas using MBC technology is presently in operation. It is expected that the development of a predictive MBC model will enable systematic optimization and scale-up for industrial applications such as high-pressure natural gas sweetening. The development, experimental verificaition and analysis of such a model are the focus of the following three contribution chapters.

Chapter 3 Predictive Mathematical Modeling of High-Pressure Membrane Contactors*

3.1 Introduction

Notwithstanding their high potential, as highlighted in Chapter 2, MBC can present a rather low mass-transfer rate under undisturbed, laminar flow in the liquid phase. The hydrophobic membranes in MBC can become wetted by organic solvents, either partially or fully. The non-wetted mode of MBC operation (Figure 3.1a) is preferred since it presents a higher CO_2 absorption rate. Operating with partially- or fully-wetted membranes (Figure 3.1b,c) can decrease the mass-transfer flux quite drastically, due to a lower gas diffusivity in the wetted membrane phase.

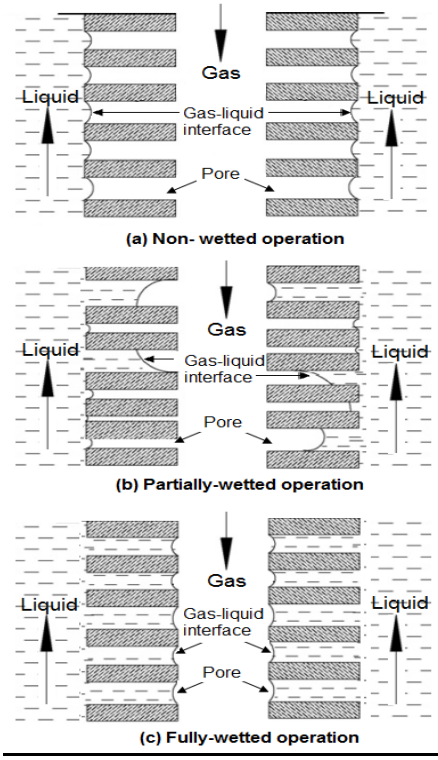

Figure 3.1: Different degrees of membrane wetting in MBC operation. Adapted from: Lu et al. (2008).

For instance, Wang et al. (2005) reported that a change in the degree of wetting as small as 5% could lead to a 20% reduction in mass transfer rate. In principle, membrane wetting could be prevented by keeping the operating pressure below a critical value, the so-called breakthrough

*This chapter is based upon material published in Chemical Engineering Research and Design. Institution of Chemical Engineers, 132, pp. 1005–1019. doi: 10.1016/j.cherd.2018.01.033.

pressure; but partial-wetting may still occur in practice due to non-uniform membrane pore sizes, with bigger pores being more easily wetted.

Many factors are known to affect the degree of wetting, including the membrane properties and various operating parameters, such as the inlet liquid pressure, liquid velocity, liquid temperature, and amine concentrations (Lu et al., 2008; Mosadegh-Sedghi et al., 2012; Rongwong et al., 2015). Moreover, the variation in liquid pressure along the length of the HFM can affect membrane wetting considerably, e.g. due to pressure drops or the static head in a vertical MBC.

Mathematical models provide an effective tool to help understand the CO_2 removal mechanisms in MBC, and thus enable a better assessment and optimization of their performance. Many modeling and simulation studies in the literature assume a non-wetted mode of operation, e.g. for MBC operating at or near atmospheric pressure (Hoff et al., 2004; Al-Marzouqi et al., 2008; Rezakazemi et al., 2011; Hoff & Svendsen, 2014). When partially- or fully-wetted operation is considered, the degree of membrane wetting (or a related parameter) is typically used as a tuning parameter in order for the model predictions to fit given experimental data. For instance, Chabanon et al. [2013] compared several modeling approaches for predicting CO_2 absorption in MBC, ranging from constant mass-transfer coefficient models to 1-d or 2-d convection-diffusion models, and with the membrane mass-transfer coefficient used as the single tuning parameter. They found that the use of convection-diffusion models is justified to obtain accurate predictions, in particular when large amine solvent conversions take place. Other studies showing a good agreement between experimental data and the predictions of a 2-d convection-diffusion model by adjusting the degree of membrane wetting can be found in Lu et al. (2008) and Cui et al. (2015). As far as high-pressure MBC operation is concerned, e.g. for NG sweetening applications, limited modeling studies have been published to date. For instance, Faiz & Al-Marzouqi (2010) studied the removal of CO_2 from NG in high-pressure MBC between 10-50 bar. They reported a good agreement between a 2-d model and experiments when adjusting the degree of wetting, which also they found to be highly sensitive.

Because of this high sensitivity of the membrane wetting to different operating conditions, analyzing or optimizing the performance of an MBC under the assumption of a constant membrane wetting could lead to erroneous (over-optimistic) results. In response to this, approaches to predicting the degree of membrane wetting in MBC have started to appear in

recent years. The studies by Boributh et al. (2011) and Goyal et al. (2015) in particular, exploit knowledge about a membrane's pore-size distribution to predict the degree of wetting in MBC operating at atmospheric pressure.

The main contribution of this chapter is the development of a predictive mathematical model of high-pressure MBC for NG sweetening applications, on the basis of which model-based parametric studies and optimization can be conducted. Building upon previous modeling studies, a combination of 1-d and 2-d mass-balance equations is considered to predict the CO_2 absorption flux, whereby the degree of membrane wetting itself is calculated using the Laplace-Young equation based upon knowledge of the membrane pore-size distribution, real gas behavior is also accounted for at high-pressure operation. The predictive capability of this model is tested against data from two experimental settings: a lab-scale MBC module, where the purification was conducted using binary gas mixtures of CH_4/CO_2 and N_2/CO_2 at 11 bar; and a pilot-scale MBC module operated under industrially relevant conditions at a natural gas processing plant in Malaysia. All of the experiments were conducted with aqueous mixtures of MDEA and piperazine (PZ) as the chemical solvent, under lean solvent condition, and with vertically oriented MBC modules. The ability to predict the variation in membrane wetting along the fiber length makes it possible to analyze the effects of various design and operational decisions on the MBC performance, including the membrane properties, module characteristics, gas and liquid flow rates, and operating pressures and temperatures.

The rest of the chapter is organized as follows. The mathematical model of a counter-current hollow-fiber MBC module is presented in Sec. 3.2, followed by a description of both experimental set-ups, corresponding model parameters, and computational methods in Sec. 3.3. Results of the experimental model verification are presented and discussed in Sec. 3.4. Then, a model-based analysis is conducted in Sec. 3.5, with a view to quantifying the effects of module orientation and high-pressure operation on a module's CO_2 removal efficiency. Finally, Sec. 3.6 concludes the chapter.

3.2 Modeling of High-Pressure Hollow-Fiber MBC

This section describes a comprehensive mathematical model for predicting the CO_2 removal efficiency in a high-pressure, hollow-fiber MBC module, as depicted on the left panel in Figure 3.2. The NG gas mixture containing CO_2 flows through the membrane fibers, while the amine solvent flows inside the shell, in a counter-current arrangement. The gas mixture diffuses from the tube side through the fiber walls into the shell, where CO_2 dissolves in the solvent before reacting with the solvent in order to enhance the removal rate.

The shell area between the fibers depends on the packing density, $\emptyset$ defined as

$$\emptyset = N\frac{r_2^2}{R_{\mathrm{m}}^2}, \tag{3.1}$$

where N is the number of fibers in the MBC module; R_{m} [m] is the inner radius of the module; and r_2 [m] is the outer radius of the fibers. Following Happel (1959), the domain of fluid surrounding each fiber can be conveniently approximated by a cylinder with cross-section radius, r_3 [m] given by

$$r_3 = r_2\sqrt{1/\emptyset}\,. \tag{3.2}$$

It is thus sufficient to consider a piece of hollow fiber in order to model the MBC module, as shown on the center panel in Figure 3.2.

In order to describe the degree of membrane wetting, a so-called wetted radius is introduced, r_{w} [m], a conceptual variable representing the average fraction of membrane pores filled with liquid; see Sec. 3.2.1 below for details. The non-wetted and fully-wetted modes of operation thus correspond to $r_{\mathrm{w}} = r_2$ and $r_{\mathrm{w}} = r_1$, respectively, with r_1 the inner radius of the fibers. On exploiting symmetry, the spatial domain to model a piece of hollow fiber can be taken as $(r, z) \in [0, r_3] \times [0, L]$, which is further partitioned into four subdomains as shown on the right panel in Figure 3.2: (i) tube, $0 \le r \le r_1$; (ii) membrane-dry, $r_1 \le r \le r_{\mathrm{w}}(z)$; (iii) membrane-wet, $r_{\mathrm{w}}(z) \le r \le r_2$; and (iv) shell, $r_2 \le r \le r_3$. Notice that the geometry of the wetted and non-wetted membrane subdomains is complicated by the dependence of the wetted radius on

the axial position, z. In this counter-current configuration, the solvent and the gas are fed a $z = 0$ and $z = L$, respectively. Mass conservation equations and a corresponding set of boundary conditions are detailed in Sec. 3.2.2.

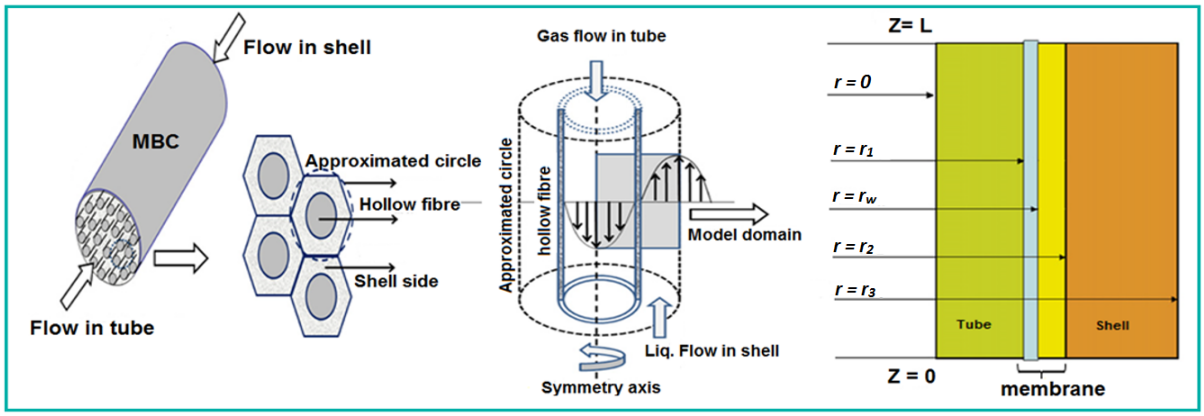

Figure 3.2: Modeling framework for a counter-current, hollow fiber MBC module. **Left:** cylindrical approximation around each fiber. **Centre:** single piece of hollow fiber. **Right:** spatial domains in MBC model.

3.2.1 Modeling of Membrane Wetting

In partially-wetted operations, a hydrophobic membrane with a non-uniform pore size distribution exhibits a range of breakthrough pressures, with larger pores filled first, followed by smaller ones. According to the Laplace-Young equation, a pore is wetted when the transmembrane pressure difference ΔP_{TMPD} [Pa], is greater than the breakthrough pressure, ΔP_{c} [Pa] given by

$$\Delta P_{\mathrm{c}}(\delta) = \frac{-2\,\gamma \cos\theta}{\delta}, \tag{3.3}$$

where δ [m] denotes the pore radius; γ [N m^{-1}], the surface tension of the liquid phase; and θ [rad], the contact angle of the liquid on the membrane.

The transmembrane pressure, namely the difference between the pressures in the liquid and gas phases, P_{l} and P_{g} [Pa], is such that

$$\Delta P_{\mathrm{TMPD}}(z) = P_{\mathrm{l}}(z) - P_{\mathrm{g}}(z) = \begin{cases} P_{\mathrm{l}}^{\mathrm{out}} - \frac{\Delta P_{\mathrm{l}}}{\Delta z}(L-z) - P_{\mathrm{g}}^{\mathrm{in}} & \text{horizontal} \\ P_{\mathrm{l}}^{\mathrm{out}} - \frac{\Delta P_{\mathrm{l}}}{\Delta z}(L-z) + \rho_{\mathrm{l}} g (L-z) - P_{\mathrm{g}}^{\mathrm{in}} & \text{vertical} \end{cases} \tag{3.4}$$

where $P_{\mathrm{g}}^{\mathrm{in}}$ [Pa] is the inlet gas pressure; $P_{\mathrm{l}}^{\mathrm{out}}$ [Pa], the outlet liquid pressure; $\frac{\Delta P_{\mathrm{l}}}{\Delta z}$ [Pa m^{-1}], the pressure gradient along the shell axis; ρ_{l} [kg m^{-3}], the liquid density; and $g = 9.81$ m s^{-2} is the gravitational acceleration. Notice the additional contribution of the liquid static head in a vertical orientation compared with a horizontal MBC. Moreover, the pressure of the gas phase is considered constant in Eq. (3.4), i.e. the effects of the pressure drop and static head are neglected.

One way of expressing the pressure drop in the shell is by using an analogy with viscous flow through assemblages of cylinders. Under the assumption of a constant pressure drop in the flow direction and a no-slip condition on the cylinders, Happel (1959) showed that the pressure drop may be computed as

$$\frac{\Delta P_{\mathrm{l}}}{\Delta z} = -8\mu_{\mathrm{l}}\overline{v}_{\mathrm{l}} \frac{r_3^2 - r_2^2}{4r_2^2 r_3^2 - r_2^4 - 3r_3^4 - 4r_3^4 \ln\left(\frac{r_2}{r_3}\right)}, \tag{3.5}$$

where μ_{l} [kg m^{-1} s^{-1}] is the dynamic viscosity of the liquid phases; and the average liquid velocity, $\overline{v}_{\mathrm{l}}$ [m s^{-1}] is given by

$$\overline{v}_{\mathrm{l}} = \frac{F_{\mathrm{l}}^{\mathrm{in}}}{\pi R_{\mathrm{m}}^2 (1-\emptyset)}, \tag{3.6}$$

with $F_{\mathrm{l}}^{\mathrm{in}}$ [m^3 s^{-1}] the liquid volumetric flowrate at the shell inlet $z = 0$.

In order to prevent membrane wetting and bubble formation, an MBC should ideally be operated such that

$$\Delta P_{\mathrm{c}}(\delta) \geq \Delta P_{\mathrm{TMPD}}(z) \geq 0, \tag{3.7}$$

for all pore radii and all axial positions. If partial wetting occurs at a given position $0 \leq z \leq L$, the wet pores are those having a radius larger than δ_{w} [m], given by

$$\delta_{\mathrm{w}}(z) = \frac{-2\,\gamma\cos\theta}{\Delta P_{\mathrm{TMPD}}(z)}\,. \tag{3.8}$$

In practice, the degree of wetting is often described in terms of the wetting ratio, $\mathfrak{z}$, which represents the ratio between the porous-volume occupied by liquid phase and the total porous-volume. Under the assumption that the wetted pores are completely filled with liquid - see Goyal et al. (2015) for a discussion - the wetting ratio may be computed as

$$\mathfrak{z}(z) = \frac{\int_{\delta_{\mathrm{w}}(z)}^{\delta_{\max}} \delta^2\, f(\delta)\, d\delta}{\int_{0}^{\delta_{\max}} \delta^2\, f(\delta)\, d\delta}\ , \tag{3.9}$$

for a given pore size distribution (PSD) function f, and a maximal pore radius, $\delta_{\max}$ [m]. Then, the conceptual wetted radius r_{w} representing the average fraction of a pore filled with liquid at a certain position z -see right panel in Figure 3.2- is related to the wetting ratio $\mathfrak{z}$ in the following way

$$r_{\mathrm{w}}(z) = r_2 - [r_2 - r_1]\,\mathfrak{z}(z)\,. \tag{3.10}$$

3.2.2 Mass Conservation Equations

The mathematical model presented hereafter is based on steady-state and isothermal operation in all of the phases – see Sec. 3.4 for further discussions about the effect of temperature. The mass conservation equations in the gas, liquid and membrane phases are detailed in the following paragraphs, together with the corresponding boundary conditions and the main modeling assumptions.

Gas Phase in Tube, $(\boldsymbol{r}, \boldsymbol{z}) \in [\mathbf{0}, \boldsymbol{r_1}] \times [\mathbf{0}, \boldsymbol{L}]$

The gas phase in the lumen is described using a simple plug flow, assuming homogeneous concentrations in each cross-section and neglecting the gas diffusivity (Péclet $>10^6$) and pressure drops along the fiber axis. These assumptions have been validated through previous studies in MBC modeling (Rezakazemi et al, 2011; Goyal et al., 2015). Moreover, due to operation at elevated pressures, real gas behaviour is accounted using a compressibility factor correction, calculated with the Peng-Robinson (PR) equation of state.

Mass conservation in the tube expresses the fact that the reduction in flux along the fiber axis is equal to the flux passing through the membrane. The differential equations describing the average velocity of the gas phase, $\overline{v_g}$ [m s^{-1}] and the average CO_2 concentration, $\overline{C_{CO_2}}$ [mol m^{-3}] are

$$\frac{d\overline{v_g}(z)}{\partial z} = -\frac{2\,D_{CO_2,md}}{r_1}\,\frac{ZRT_g^{in}}{P_g^{in}}\,\frac{\partial C_{CO_2}(r,z)}{\partial r}\Big|_{r=r_1^+}, \tag{3.11}$$

$$\frac{d\overline{C_{CO_2}}(z)}{\partial z} = -\frac{2\,D_{CO_2,md}}{\overline{v_g}(z)r_1}\left[1-\frac{ZRT_g\overline{C_{CO_2}}(z)}{P_g^{in}}\right]\frac{\partial C_{CO_2}(r,z)}{\partial r}\Big|_{r=r_1^+}, \tag{3.12}$$

where r_1^+ indicates the gas-membrane interface at the pore side; T_g^{in} [K] is the temperature of the gas; Z [−], the compressibility factor; $R = 8.3145$ J mol^{-1} K^{-1}, the ideal gas constant; and $D_{CO_2,md}$ [m^2 s] denotes the effective CO_2 diffusion coefficient in the dry part of the membrane, such that

$$D_{CO_2,md} = \frac{\varepsilon}{\tau} D_{CO_2,g}, \tag{3.13}$$

with $D_{CO_2,g}$ [m^2 s], the diffusion coefficient of CO_2 in the gas phase; and ε, τ, the porosity and tortuosity of the membrane, respectively. Initial conditions at the inlet $z = L$ of the fiber are given by

$$\overline{v_g}(L) = \overline{v_g}^{in} = \frac{M_g^{in}}{N\pi r_1^2 \rho_g}, \tag{3.14}$$

$$\overline{C_{CO_2}}(L) = C_{CO_2}^{in} = \frac{y_{CO_2,g}^{in} P_g^{in}}{ZRT_g}, \tag{3.15}$$

where M_g^{in} [kg s^{-1}] is the inlet mass flowrate of gas; $y_{CO_2,g}^{in}$ [−], the inlet molar fraction of CO_2; and ρ_g [kg m^{-3}], the density of the gas phase.

Liquid Phase in Shell, $(r, z) \in [r_2, r_3] \times [0, L]$

The liquid flow in the shell is laminar (Reynolds <10), and the velocity profile is assumed to be fully developed, following Happel's free surface model (Happel, 1959). Moreover, axial

diffusivity in the liquid phase (Péclet >10^7) is neglected, and the liquid phase is incompressible and that the reaction between CO_2 and the solvent does not incur any change in volume.

The general transport equation for a species $i \in \{\mathrm{CO_2}, \mathrm{sol}\}$ at steady state in the 2-d cylindrical coordinate system (r, z), taking into account convection, radial diffusion and reaction, reads (Cussler, 2009):

$$v_{\mathrm{l}}(r)\frac{\partial C_i(r,z)}{\partial z} = D_{i,\mathrm{l}}\left[\frac{\partial^2 C_i(r,z)}{\partial r^2} + \frac{1}{r}\frac{\partial C_i(r,z)}{\partial r} + \frac{\partial^2 C_i(r,z)}{\partial z^2}\right] + R_i(C_i(r,z))\,, \tag{3.16}$$

where $D_{i,\mathrm{l}}$ [m^2 s] and R_i [mol m^{-3} s^{-1}] denote the diffusion coefficient and the reaction rate of the species i in the liquid phase, respectively; and v_{l} [m s^{-1}] is the local fluid velocity, which by analogy with viscous flow in an assemblage of cylinders—compare Eq. (3.5)—may be computed as (Happel, 1959)

$$v_{\mathrm{l}}(r) = -\frac{1}{4\mu_{\mathrm{l}}}\left[r^2 - r_2^2 + 2r_3^2\ln\left(\frac{r_2}{r}\right)\right]\frac{\Delta P_{\mathrm{l}}}{\Delta z} = 2\overline{v}_{\mathrm{l}}(r_3^2 - r_2^2)\frac{r^2 - r_2^2 + 2r_3^2\ln\left(\frac{r_2}{r}\right)}{4r_2^2r_3^2 - r_2^4 - 3r_3^4 - 4r_3^4\ln\left(\frac{r_2}{r_3}\right)} \tag{3.17}$$

The distribution of the CO_2 and solvent at the shell inlet are supposed to be uniform,

$$C_{\mathrm{CO_2}}(r,0) = f_{\mathrm{CO_2,l}}^{\mathrm{in}}C_{\mathrm{sol}}^{\mathrm{in}}\,, \tag{3.18}$$

$$C_{\mathrm{sol}}(r,0) = C_{\mathrm{sol}}^{\mathrm{in}}\,, \tag{3.19}$$

with $C_{\mathrm{sol}}^{\mathrm{in}}$ $\left[\mathrm{mol\ m^{-3}}\right]$ the solvent concentration in the liquid feed; and $f_{\mathrm{CO_2,l}}^{\mathrm{in}}$ $\left[\mathrm{mol\ mol^{-1}}\right]$, the CO_2 loading in solvent. At the shell outlet, a no-dispersion condition is imposed as

$$\left.\frac{\partial C_i(r,z)}{\partial z}\right|_{z=L} = 0\,, \quad i \in \{\mathrm{CO_2}, \mathrm{sol}\}\,. \tag{3.20}$$

The condition of axisymmetric flow condition at $r = r_3$ gives

$$\left.\frac{\partial C_i(r,z)}{\partial r}\right|_{r=r_3} = 0\,, \quad i \in \{\mathrm{CO_2}, \mathrm{sol}\}\,, \tag{3.21}$$

and continuity of the concentrations and fluxes at the membrane surface, $r = r_2$ imposes

$$C_i(r_2^+, z) = C_i(r_2^-, z)\,, \quad i \in \{\mathrm{CO_2}, \mathrm{sol}\}\,, \tag{3.22}$$

$$D_{i,\mathrm{l}} \frac{\partial C_i(r,z)}{\partial r}\Big|_{r=r_2^+} = D_{i,\mathrm{mw}} \frac{\partial C_i(r,z)}{\partial r}\Big|_{r=r_2^-}\,, \quad i \in \{\mathrm{CO_2}, \mathrm{sol}\}\,, \tag{3.23}$$

where the radial positions r_2^+ and r_2^- correspond to either sides of the liquid-membrane interface; and $D_{i,\mathrm{mw}}$ [$\mathrm{m^2\ s}$] denotes the effective diffusion coefficient of a species i in the wetted part of the membrane, such that

$$D_{i,\mathrm{mw}} = \frac{\varepsilon}{\tau} D_{i,\mathrm{l}}\,. \tag{3.24}$$

Membrane Phase, $(\boldsymbol{r}, \boldsymbol{z}) \in [\boldsymbol{r_1}, \boldsymbol{r_2}] \times [\boldsymbol{0}, \boldsymbol{L}]$

The membrane properties are considered to be uniform along the fiber axis, including pore size distribution, tortuosity, porosity, thickness, and hydrophobicity. The mass transfer inside the membrane is assumed to be driven by radial diffusion only, considering the gas and liquid phases to be stagnant therein, and that Henry's law is applicable at the gas–liquid interface. The dissolution of gas species other than CO_2 into the liquid phase is neglected while the amine solvent is considered to be non-volatile.

The partial differential equations describing the transport of CO_2 and solvent inside the membrane are given by

$$D_{\mathrm{CO_2,md}} \left[\frac{\partial^2 C_{\mathrm{CO_2}}(r,z)}{\partial r^2} + \frac{1}{r}\frac{\partial C_{\mathrm{CO_2}}(r,z)}{\partial r}\right] = 0 \quad \text{if } r_1^+ \le r \le r_{\mathrm{w}}^-(z)\,, \tag{3.25}$$

$$D_{\mathrm{i,mw}} \left[\frac{\partial^2 C_i(r,z)}{\partial r^2} + \frac{1}{r}\frac{\partial C_i(r,z)}{\partial r}\right] + R_i(C_i(r,z)) = 0, \quad i \in \{\mathrm{CO_2}, \mathrm{sol}\} \quad \text{if } r_{\mathrm{w}}^+(z) \le r \le r_2^- \tag{3.26}$$

The equilibrium condition at the gas-liquid interface, $r = r_{\mathrm{w}}(z)$ inside the membrane is expressed as

$$C_{\mathrm{CO_2}}(r_{\mathrm{w}}^-(z), z) = \frac{H_{\mathrm{CO_2,l}}}{ZRT_{\mathrm{g}}} C_{\mathrm{CO_2}}(r_{\mathrm{w}}^+(z), z)\,, \tag{3.27}$$

where r_w^+ and r_w^- indicate either sides of the gas-liquid interface inside the membrane; $H_{CO_{2,l}}$ $\left[m^3\ Pa\ mol^{-1}\right]$ stands for Henry's constant for CO_2 in amine solution. At this interface, the flux of solvent is equal to zero, while the flux of CO_2 is continuous,

$$D_{CO_2,md} \frac{\partial C_{CO_2}(r,z)}{\partial r}\Big|_{r=r_w^-(z)} = D_{CO_2,mw} \frac{\partial C_{CO_2}(r,z)}{\partial r}\Big|_{r=r_w^+(z)}, \tag{3.28}$$

$$\frac{\partial C_{sol}(r,z)}{\partial r}\Big|_{r=r_w^+(z)} = 0. \tag{3.29}$$

At the membrane-gas interface, $r = r_1$, the CO_2 concentration is continuous,

$$C_{CO_2}(r_1^+, z) = \overline{C_{CO_2}}(z), \tag{3.30}$$

and the CO_2 flux continuity was already expressed in Eq. (3.12). The concentration and flux continuity conditions at the membrane-liquid interface, $r = r_2$ were already expressed in Eqs. (3.22) - (3.23) above.

3.3 Material and Methods

3.3.1 Experimental Setups

The lab-scale module experiments were conducted with two binary feed gas mixtures of CH_4/CO_2 and N_2/CO_2 at 11 bar. The pilot module was up-scaled by a factor of about 800 (i.e., membrane area), and operated under industrially relevant conditions at 54 bar in a natural gas processing plant in Malaysia. Both modules are shown in Figure 3.3. In both cases, aqueous mixtures of methyldiethanolamine (MDEA) and piperazine (PZ) were used as the chemical solvent. The corresponding operating conditions are summarized in Table 3.1. The experimental set-ups for lab- and pilot-scale testing are depicted in Figure 3.4 and 3.5, with further details given thereafter.

Table 3.1: Operating conditions in the lab and pilot-scale modules.

Parameters	N_2/CO_2 (Lab)	CH_4/CO_2 (Lab)	NG (Pilot)
CO_2 inlet, $y^{in}_{CO_2,g}$ [mol%]	8	8.55	5.1-5.3
MDEA/PZ inlet, [wt%]	39/5	39/5	39/5
Inlet gas pressure, P_g^{in} [kPa]	1100	1100	5400
Outlet liquid pressure, P_l^{out} [kPa]	1130	1130	5430
Gas mass flowrate, M_g^{in} $[kg\ h^{-1}]$	0.04-0.2	0.05-0.1	57-75
Liquid volumetric flowrate, F_l^{in} $[L\ h^{-1}]$	0.6-1.8	1.2	190-280
Gas temperature, T_g^{in} [K]	293	293	298-313
Liquid temperature, T_l^{in} [K]	293	308	308-313
CO_2 loading in solvent, $f^{in}_{CO_2,l}$ $[mol\ mol^{-1}]$	0	0.07	0.01

Figure 3.3: Vertical MBC operation. **Left:** lab scale MBC; **Right:** pilot scale MBC.

Lab-Scale MBC Module

Pressurized gas cylinders were used to supply mixtures of CH_4/CO_2 or N_2/CO_2 to the tube side of the lab-scale module, while the lean amine solvent was pumped through the shell side, in a counter-current and vertical configuration. The feed gas and solvent flow rates were controlled using a mass flow controller (MFC) and pump stroke, respectively, whereby the flowrates are recorded every 30 seconds. The compositions of the feed gas and treated gas were analyzed and recorded using gas chromatography (GC7900, Shanghai Tech- comp Instruments Co., Ltd) every 6 minutes, after the system had reached steady state as indicated by a constant CO_2 composition in the outlet gas stream of the module. The treated gas from the MBC module was then depressurized and vented to a safe location. A transmembrane pressure of $\Delta P_{TMPD} =$ 30 kPa was maintained at any point along the fibers to prevent gas bubbling (Kang et al., 2017). The fluid flowrates and gas compositions values were averaged hourly to minimize noise before comparing with model predictions.

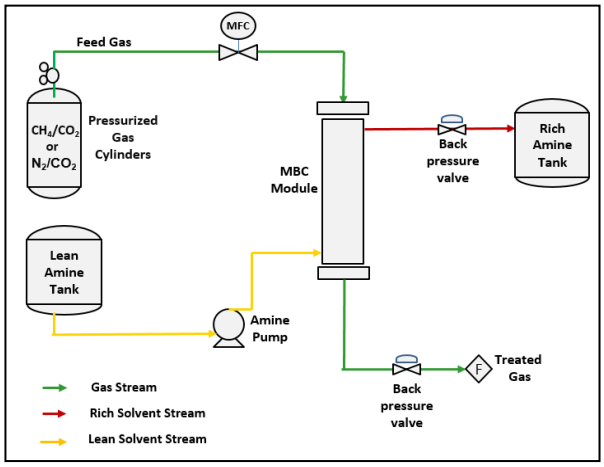

Figure 3.4: Schematic of the lab-scale setup for CO_2 removal using high pressure MBC.

Pilot-Scale MBC Module

The CO_2-rich natural gas was fed to the tube side of the MBC, while the lean amine was pressurized to ca. 54 bar and fed to the shell side, in a counter-current and vertical configuration. The feed gas and liquid flow rates were controlled using a mass flow controller and a pump stroke, respectively, whereby the flowrates are recorded every 30 seconds. The flowrate of the treated gas at the MBC outlet was measured with a mass flowmeter before sending it to the flare header. The enriched amine solvent collected from the MBC shell outlet was directed to a flash drum, whereby the degassing rate of the dissolved light hydrocarbons was measured by the flowmeter before sending it to the flare header. The gas compositions in the MBC feed and outlet as well as the flash outlet were analyzed and recorded using gas chromatography (PGC1000 Gas Chromatograph, ABB) every 6 minutes, after the system had reached steady state. The flash liquid outlet stream was heated by cross exchange with hot lean solvent, and then fed to the solvent regenerator where it was stripped of acid gas by rising stream vapors generated by the reboiler. The acid gas leaving the top of the regenerator was cooled and sent to a reflux drum to separate the condensed water from the acid gas. The condensed water was then returned to the top of the regenerator, while the acid gas was sent to the flare header. The lean solvent from the regenerator was then cooled by the lean-rich exchanger, lean solution cooler and amine chiller before recycling to the MBC absorber. Because the solvent regenerator was designed up to 10-times larger capacity than the MBC module. The excess lean solvent from the LP amine pump was recycled back to the solvent regenerator. The lean solvent was sampled to analyze/monitor the amine concentration in the solvent. Demineralized water or amine solvent is fed into amine tank periodically to make up for losses of solvent due to evaporation in MBC and regeneration column. The fluid flowrates and gas compositions values were averaged hourly and compared with model predictions.

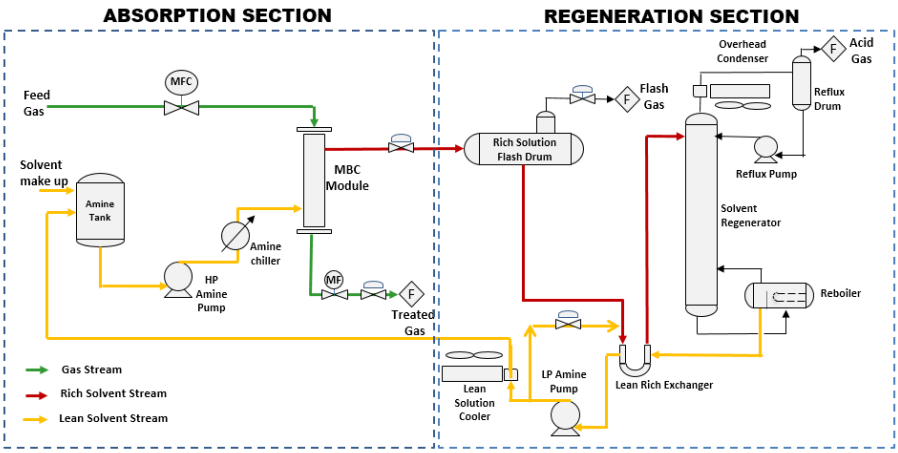

Figure 3.5: Schematic of the pilot-plant setup for CO_2 removal using high pressure MBC.

3.3.2 Membrane and Module Characteristics

The high pressure MBC modules were packed with hydrophobic, Polytetrafluoroethylene (PTFE) hollow fiber. Table 3.2 reports the main characteristics of these membranes, alongside design properties of the MBC modules used for lab- and pilot-scale testing.

Table 3.2: Specifications of the hollow-fiber membranes and the lab- and pilot-scale modules.

Parameters	**Lab module**	**Pilot module**	**Source**
Fiber length, L [m]	0.3	2	(PRSB, 2014)
Fiber inner radius, r_1 [μm]	431	431	(PRSB, 2014)
Fiber outer radius, r_2 [μm]	846	846	(PRSB, 2014)
Membrane porosity, ε [$-$]	0.41	0.41	(PRSB, 2014)
Membrane tortuosity, τ [$-$]	6.1	6.1	Eq. (3.31)
Max. pore radius, $\delta_{\max}$ [μm]	0.44	0.44	(PRSB, 2014)
Mean pore radius, $\bar{\delta}$ [μm]	0.08	0.08	Eq. (3.32)
Relative pore standard deviation, σ [$-$]	0.26	0.26	Eq. (3.32)
Contact angle, θ [°]	92.5 - 95.3	92.5	(PRSB, 2014)
Packing density, $\emptyset$ [$-$]	0.26	0.55	(PRSB, 2014)
Module inner radius, R_{m} [m]	0.015	0.115	(PRSB, 2014)
Membrane module area, A_{m} [m^2]	0.128	106.5	(PRSB, 2014)
No of fibers, N [$-$]	80	10,007	(PRSB, 2014)
Specific surface area [m^{-1}]	600	1300	(PRSB, 2014)

Following Iversen et al. (1997), a first approximation of the membrane tortuosity in Table 3.2 was obtained as

$$\tau = \frac{(2-\varepsilon)^2}{\varepsilon}. \tag{3.31}$$

In order to determine the wetting ratio in Eq. (9) needed for simulating the MBC model, pore-size distribution (PSD) data from the manufacturer (PRSB, 2014) were used to fit the following log-normal distribution (Zydney et al., 1994; Lu et al., 2008),

$$f(\delta) = \frac{1}{\sqrt{2\pi \ln(1+\sigma^2)}\bar{\delta}} \exp\left(-\frac{\left(\ln \delta/\bar{\delta}\right)^2 (1+\sigma^2)}{2\ln(1+\sigma^2)}\right), \tag{3.32}$$

where $\bar{\delta}$ and σ stand for the mean pore radius and relative pore standard deviation, respectively. The resulting least-squares fit on the left plot in Figure 3.6 shows an excellent agreement with the data, and the estimated values for $\bar{\delta}$ and σ can be found in Table 3.2. In turn, a surrogate relationship for the wetting ratio $\mathfrak{z}$ as a function of the critical pore radius δ_w in the range $[0, \delta_{max}]$ could be obtained in the form

$$\mathfrak{z}(\delta_w) = \frac{1+\tanh\left(a_0 + a_1 \delta_w/\bar{\delta} + a_2\left(\delta_w/\bar{\delta}\right)^2 + a_3\left(\delta_w/\bar{\delta}\right)^3\right)}{2}, \tag{3.33}$$

with $a_0 = 7.966$, $a_1 = -14.08$, $a_2 = 8.418$, and $a_3 = -2.041$. A comparison between the solution of Eq. (3.9) and the surrogate in Eq. (3.33) is shown on the right plot in Figure 3.6.

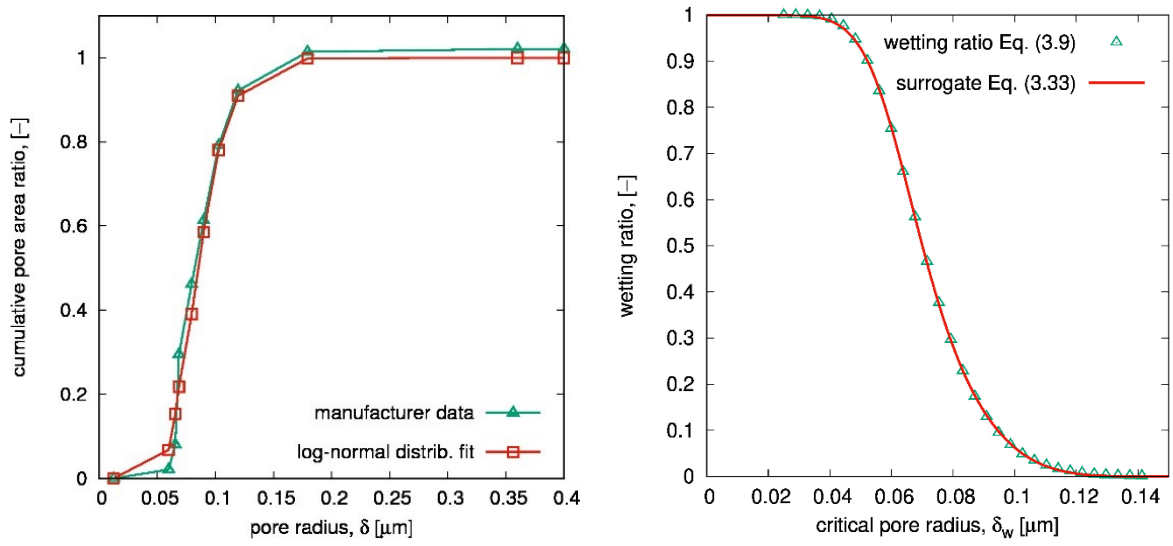

Figure 3.6: Left: Comparison of cumulative pore area ratio distribution based on the log-normal pore size distribution in Eq. (3.32) using the parameters in Table 3.2, against the manufacturer (PRSB, 2014) data. **Right:** Comparison of the wetting ratio expression in Eq. (3.9) with the surrogate expression in Eq. (3.33) in terms of the critical pore radius, δ_w.

3.3.3 Thermo-Physical, Transport, and Reaction Kinetic Data

A key parameter in the model is Henry's constant in amine solvent. In this chapter, the estimation of the Henry's constant in lean amine solvent at various temperatures is based on N_2O analogy (Versteeg and Van-Swaaij, 1988; Wang et al., 2013),

$$H_{CO_2,l} = H_{N_2O,l} \frac{H_{CO_2,H_2O}}{H_{N_2O,H_2O}}, \tag{3.34}$$

Henry's constants for N_2O and CO_2 in water, respectively H_{CO_2,H_2O} and H_{N_2O,H_2O} are taken as (Versteeg and Van-Swaaij, 1988)

$$H_{CO_2,H_2O} = 2.82 \times 10^6 \exp\left(-\frac{2044}{T_l^{in}}\right), \tag{3.35}$$

$$H_{N_2O,H_2O} = 8.55 \times 10^6 \exp\left(-\frac{2284}{T_l^{in}}\right), \tag{3.36}$$

Henry's constant for N_2O in lean amine solution, $H_{N_2O,l}$ is described by a semi-empirical model correlating the excess Henry's coefficient as (Bensetiti et al., 1999)

$$\ln H_{N_2O,l} = \phi_{MDEA} \ln H_{N_2O,MDEA} + \phi_{PZ} \ln H_{N_2O,PZ} + \phi_{H_2O} \ln H_{N_2O,H_2O} + \phi_{MDEA}\phi_{H_2O}\left[-2.899 + \frac{1405.43}{T_l^{in}}\right] \tag{3.37}$$

with ϕ_i the volume fraction of species i; and the solubility of N_2O in pure amine solvent $i \in$ {MDEA,PZ} taken as (Wang et al., 1992)

$$H_{N_2O,MDEA} = H_{N_2O,PZ} = 1.52 \times 10^5 \exp\left(-\frac{1312.7}{T_l^{in}}\right). \tag{3.38}$$

Other temperature-dependent expressions for (i) the macroscopic reaction rates of CO_2 with MDEA and PZ; and (ii) the diffusivity coefficients of the various species in gas or liquid mixtures are reported in Appendix A for completeness. Values for the other thermo-physical and transport parameters were obtained by interfacing gPROMS with the property packages 'Advanced Peng Robinson' and 'UNIQUAC-RK'.

3.3.4 Numerical Simulation

The mixed set of algebraic, ordinary differential and partial differential equations was implemented in the gPROMS modeling language (Oh and Pantelides, 1996), using ModelBuilder v5.0. A second-order centered finite difference scheme was used to discretize the differential equations, after a rescaling of the radial dimension in the partial differential equations in order for the membrane dry and wet spatial subdomains to be rectangular as outlined in Appendix B (Table B.1). A uniform mesh grid consisting of 70 elements was chosen to perform the simulations herein, which provides solutions within <1% of finer discretizations, while retaining computational tractability. With this discretization, a steady-state simulation takes up to few minutes to complete on a desktop computer running Windows 7 with Intel® CoreTM i7-4790 CPU at 3.60GHz and 32GB of RAM.

3.4 Experimental Model Verification

3.4.1 Lab-Scale MBC Module

A comparison between measured and predicted CO_2 removals in the lab-scale MBC is presented in Figure 3.7, in terms of the CO_2 absorption flux, Φ [mol m^{-2} s^{-1}] computed as

$$\Phi = \frac{\pi r_1^2 N}{A_m}\left[\overline{v}_g(L)\,\overline{C_{CO_2}}(L) - \overline{v}_g(0)\,\overline{C_{CO_2}}(0)\right]. \tag{3.39}$$

The experimental data are for several flow rates of the two gas mixtures N_2/CO_2 and CH_4/CO_2 (see Table 3.1), and also correspond to different flow rates of the amine solvent. Overall, the predictions are in excellent agreement with the measurements, showing errors lower than 5%. Notice that such an agreement is quite remarkable given that none of the model parameters are adjusted here, thereby providing a first validation of the main modeling assumptions.

The MBC model correctly predicts the increase in CO_2 absorption flux with a larger inlet gas flowrate, driven by a larger amount of CO_2 in the gas feed. As far as membrane wetting is concerned, non-wetted operation is predicted for all three N_2/CO_2 experiments in Figure 3.7A-C, whereas a wetting ratio in the range 5-11% is predicted for the CH_4/CO_2 experiment. This

difference between both gas mixtures can be attributed to a higher contact angle in the experiment with N_2/CO_2 ($\theta = 95.3°$) compared with CH_4/CO_2 ($\theta = 92.5°$).

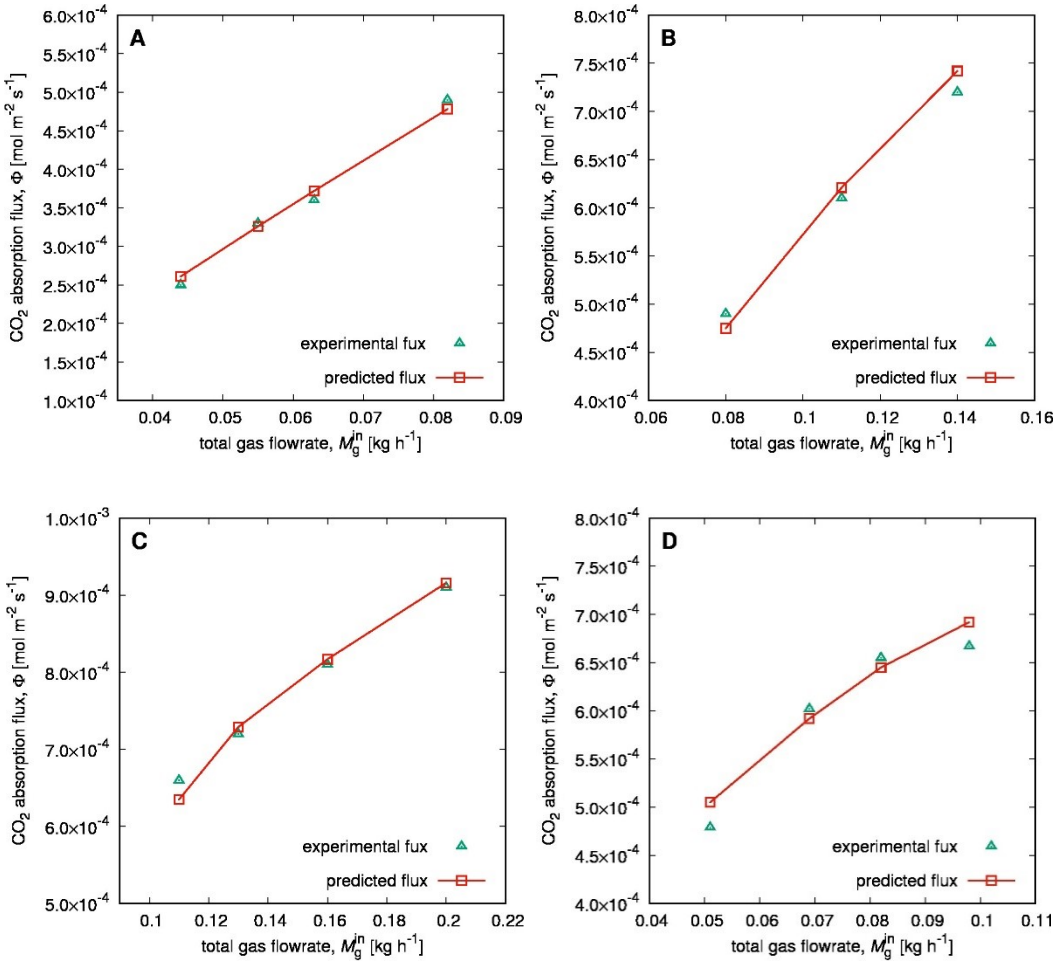

Figure 3.7: Predicted CO_2 absorption fluxes against experimental measurements in lab-scale MBC module. **A,B,C:** effect of N_2/CO_2 gas flowrate for fixed solvent flowrates of 0.6 L h^{-1}, 1.2 L h^{-1}, and 1.8 L h^{-1}, respectively; **D:** effect of CH_4/CO_2 gas flowrate for a fixed solvent flowrate of 1.2 L h^{-1}.

3.4.2 Pilot-Scale MBC Module

A comparison between measured and predicted CO_2 removals in the pilot-scale MBC module is presented in Figure 3.8, also in terms of the CO_2 absorption flux Φ defined in Eq. (3.39). The experimental data correspond to different flow rates of the amine solvent and of the NG mixture (see Table 3.1). The MBC model predictions are in good agreement with the measurements, albeit showing larger and more systematic errors, up to 10% overestimation, as compared with the lab-scale results in Figure 3.8. A possible explanation for such systematic offsets between the predictions and measurements, could be due to the model currently

neglecting the heat generated from the reaction between CO_2 and the amines, which causes the liquid temperature to rise. This scenario is analyzed in Sec. 3.4.3 below. Another contribution to this offset could be underestimating the mass-transfer resistance near the membrane-liquid interface, especially at lower liquid flow rates, e.g. due to the formation of a boundary film.

The model correctly captures the improvement in CO_2 absorption flux on increasing the solvent flowrate in Figure 3.8A, and it also predicts a corresponding small increase in the membrane wetting. This extra wetting is due to a higher pressure drop in the shell, and therefore a higher transmembrane pressure, as described in Eqs. (3.4) and (3.5). On balance however, the effect of a larger wetting remain small in comparison with the effect of a leaner amine (and hence a larger concentration gradient) in terms of the overall CO_2 mass transfer. These results are also a confirmation that the MBC performance is, to a large extent, dominated by the physicochemical processes taking place in the liquid phase, a behavior that has been reported elsewhere in the literature (Boributh et al., 2011; Goyal et al., 2015).

The model also correctly captures the increase in CO_2 absorption flux for increasing inlet gas flowrates in Figure 3.8B, as driven by a larger amount of CO_2 in the gas feed. Also note that, since the pressure drops in the tubes is negligible – see Eq. (3.4) – increasing the inlet gas flowrate has essentially no effect on the wetting ratio.

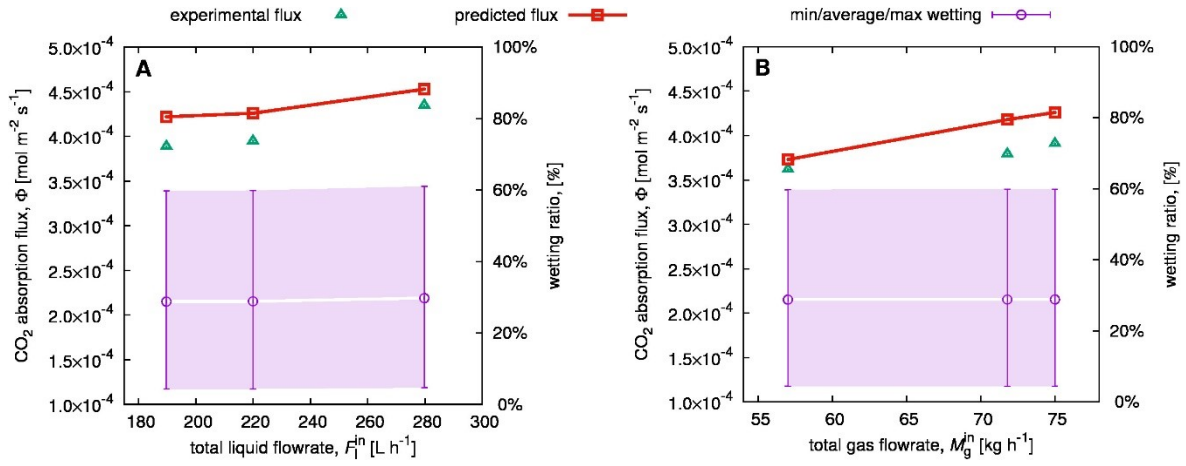

Figure 3.8: Predicted CO_2 absorption fluxes against experimental measurements in pilot-scale MBC module, together with predicted membrane wetting. **A:** effect of solvent flowrate for a fixed NG flowrate of 75 kg h^{-1}. **B:** effect of NG flowrate for a fixed solvent flowrate of 220 L h^{-1}.

3.4.3 Temperature Correction

This subsection quantifies the effect of a rise in the solvent temperature due to the exothermic reaction between CO_2 and the amines. An increase in the solvent temperature leads to a reduction in surface tension, therefore causing extra wetting of the membrane according to Eq. (3.3) and a reduction in the CO_2 flux through the membrane. The temperature difference, ΔT_l [K] between the lean amine fed to the MBC module and the enriched amine outlet can be estimated by means of a lumped energy balance under adiabatic conditions (Li et al., 2017),

$$\rho_l F_l^{in} C_p \, \Delta T_l = \Phi A_m \, \Delta H_r \, . \tag{3.40}$$

where the term ΦA_m [mol s^{-1}] describes the overall rate of CO_2 removal; and the specific heat capacity of the amine solvent and the enthalpy of reaction are set to $C_p = 3600$ J kg^{-1} K^{-1} (Weiland et al., 1997) and $\Delta H_r = -60000$ J mol^{-1} (Kabadi, 2007), respectively, in a first approximation which are assumed to be independent of temperature.

Based on Eq. (3.40) and the data in Table 3.1, the solvent temperature in the pilot-scale MBC module is predicted to increase by 10-14 K. This rise, in turn, corresponds to a reduction in the solvent surface tension from 0.046 N m^{-1} to about 0.044 N m^{-1}. The results of the MBC model simulations with the corrected surface tension values are presented in Figure 3.9. The predicted CO_2 absorption fluxes are now in close agreement with the measured efficiencies, after an increase in the predicted membrane wetting. By contrast, the solvent temperature in the lab-scale MBC module is predicted to increase by a few degrees only, which have a minor impact on the computed fluxes in Figure 3.7. The larger temperature rise in the pilot-scale module is due to the liquid-to-CO_2-gas-absorbed (L/G) ratio thereof being only one-third of the L/G ratio in the lab-scale module. A low L/G ratio as in the pilot-scale module is comparable to conventional packed columns, and is typically preferred in practice since it reduces the energy needed for solvent regeneration (Liebenthal et al., 2013). In sum, this cursory analysis confirms that one should not neglect the temperature rise in the solvent to empower more accurate performance predictions in pilot-scale (or larger-scale) MBC modules. Clearly, this calls for the development of a detailed energy balance alongside the mass balance equations in the MBC model, which will be addressed as part of Chapter 4.

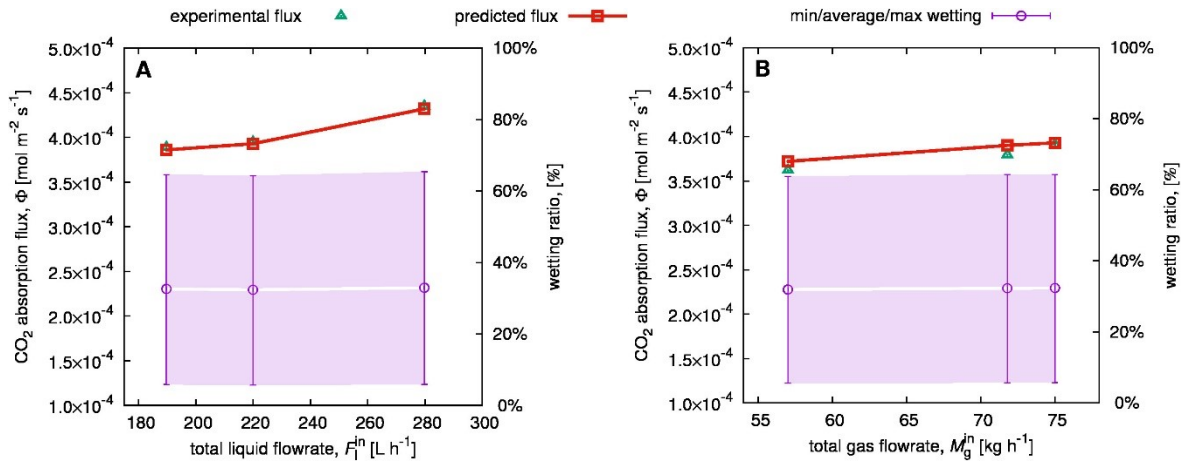

Figure 3.9: Temperature-corrected predictions of CO_2 absorption fluxes against experimental measurements in pilot-scale MBC module, together with predicted membrane wetting. **A:** variation of the solvent flowrate for a fixed NG flowrate of 75 kg h^{-1}; **B:** variation of the NG flowrate for a fixed solvent flowrate of 220 L h^{-1}.

3.5 Model-Based Analysis

This section of the chapter presents a model-based analysis of MBC for natural gas sweetening, with a focus on high-pressure operation and membrane wetting. The analysis is conducted for the pilot-scale MBC module, and applies the temperature correction discussed earlier.

3.5.1 Effect of High Pressure MBC Operation on CO_2 Removal Efficiency

The benefits of atmospheric MBC operation for CO_2 removal are well established (Mansourizadeh and Ismail, 2009; Zhang and Wang, 2013). This section investigates whether or not high-pressure operation is advantageous to the MBC performance in terms of CO_2 removal. Physically, the diffusivity of CO_2 in NG is known to decrease at higher pressure, thus increasing the overall mass transfer resistance; whereas an increase in the CO_2 partial pressure will enhance the mass transfer, and so will a lower gas velocity by increasing the residence time of the gas. Predicting the net effect of raising the operating pressure on the CO_2 absorption flux and the CO_2 removal efficiency is therefore challenging.

The graph in Figure 3.10A shows the effect of varying the operating pressure in the (vertical) pilot-scale MBC on the CO_2 removal efficiency, η [−] given by

$$\eta = 1 - \frac{\overline{v_g}(0)\,\overline{C_{CO_2}}(0)}{\overline{v_g}(L)\,\overline{C_{CO_2}}(L)}. \tag{3.41}$$

The MBC model predicts an improvement in CO_2 removal efficiency from about 60% to 80% in increasing both the gas and liquid pressures from 1400 kPa to 5400kPa (maintaining a transmembrane pressure of $\Delta P_{TMPD} = 30$ kPa along the fibers in order to prevent gas bubbling). This corresponds to an improvement in CO_2 absorption flux Φ by nearly 40%. On balance, the increase in mass transfer driving force and the longer residence time thus clearly dominate over the lower diffusivity in terms of CO_2 absorption and removal efficiency. These results are consistent with those previously reported by Faiz and Al-Marzouqi (2010), although their model could not predict the effect of varying operating conditions on membrane wetting or the evolution of membrane wetting along a hollow fiber. In particular, the model only predicts small variations in the wetting ratio in operating the MBC at different pressures, and therefore the performance improvement at high pressure is not associated with a reduction in membrane wetting.

From a process engineering standpoint, higher efficiency in terms of CO_2 removal in high-pressure MBC compared with atmospheric operation could enable a reduction of the absorber volume (*i.e.*, lower membrane area and module size) and/or a lower solvent flowrate (*i.e.,* lower solvent regeneration and pumping energy) in order to meet a certain CO_2 purity specification.

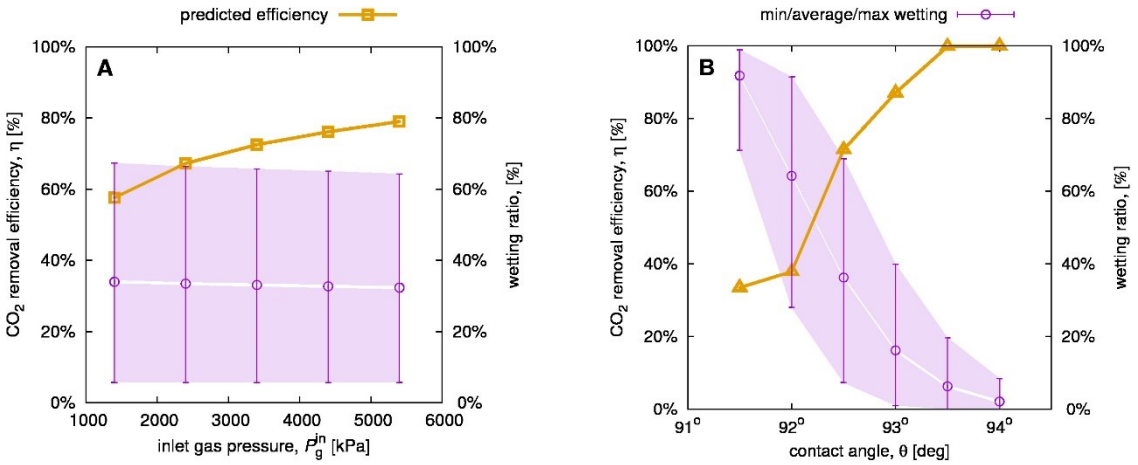

Figure 3.10: Model-based analysis of (vertical) pilot-scale MBC module. The NG gas and solvent flowrates are 75 kg h^{-1} and 220 L h^{-1}, respectively. The solvent temperature is corrected using Eq. (3.40). **A:** effect of operating pressure. **B:** effect of the contact angle.

.

3.5.2 Effect of MBC Module Orientation on CO_2 Removal Efficiency

The concentration profiles of CO_2 and amines around a single fiber are shown in Figure 3.11A, for the pilot-scale module in vertical orientation, operated under 5400 kPa and with other conditions as given in Table 3.1. The three graphs show that the wetting ratio ζ (or, equivalently, the wetting radius r_w) varies significantly along the fiber axis, from about 6% at the gas inlet to over 64% at the gas outlet. This variation is mainly due to the static head in the liquid phase, while the pressure drops remain small in comparison.

On the left graph in Figure 3.11A, the CO_2 concentration in the tube is the highest at the gas inlet, $z = 2$ m, and decreases along the fiber. In this vertical configuration, the predicted CO_2 removal efficiency is rather low, around $\eta \approx 79\%$, due to significant wetting of the membrane. Recall also that the gas phase is uniform in each tube cross-section per the modeling assumptions in Sec. 3.2.2. In the dry part of the membrane, the CO_2 concentration is decreasing slightly in the radial direction due to diffusive transfer limitation, and then shows a discontinuity at gas-liquid interface, with a near-zero CO_2 concentration across the liquid phase.

The center and right graphs in Figure 3.11A show that the MDEA and PZ amine concentrations in the shell are the highest at the liquid inlet, $z = 0$ m, and decrease along the fiber axis due to the reactions with CO_2. It is noticeable that the PZ concentration decreases faster than the MDEA concentration, due to PZ having a higher reactivity with CO_2 than MDEA. These plots also depict steep gradients in MDEA and PZ concentrations across the wetted-part of the membrane, as well as some variations across the liquid phase, which justify the use of 2-d modeling to describe radial diffusive mass transfer in the membrane and shell sections.

For comparison, the concentration profiles shown in Figure 3.11B are for the same pilot-scale module, now in horizontal orientation. The wetting ratio is predicted to be much smaller and about constant along the fiber length, around 6%, due to the transmembrane pressure difference no longer being subject to the liquid static head; see Eq. (3.4). Consequently, the predicted CO_2 removal efficiency in horizontal orientation improves enormously, reaching 99.99% (residual concentration of $\overline{C_{CO_2}}(0) \approx 1.5 \times 10^{-2}$ mol m^{-3}), as compared with a mere 79% removal in vertical orientation. Also notice that a majority of the PZ amine is depleted at the horizontal module outlet. By contrast, the performance of the lab-scale module, whose length is much

shorter than the pilot-scale one (see Table 3.2), does not improve significantly in changing the orientation to horizontal (results not shown).

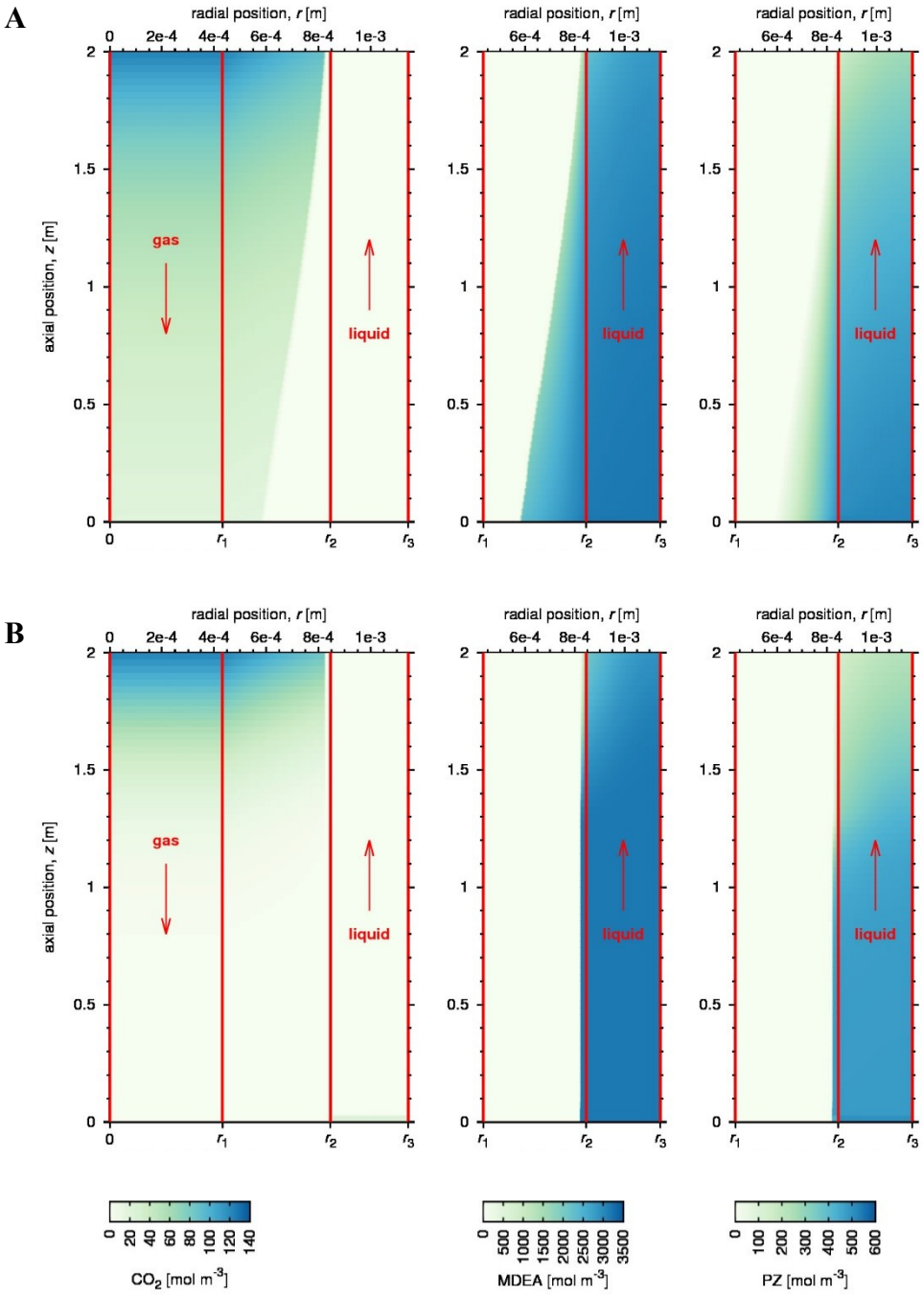

Figure 3.11: Concentration profiles of CO_2 **(left)**, MDEA **(center)** and PZ **(right)** for a single fiber of the pilot-scale MBC module. The NG and solvent flowrates are 75 kg h^{-1} and 220 L h^{-1}, respectively. The solvent temperature is corrected using Eq. (3.40). **A:** vertical module orientation. **B:** horizontal module orientation.

Overall, this analysis suggests that, for the PTFE hollow-fiber membrane at hand, the vertical mode of operation might not be viable in pilot-scale and larger-scale applications where the fibers are several meters long. For such tall modules, the effect of liquid static head could result in the bottom section of the membrane being fully wetted, thereby reducing the CO_2 absorption flux dramatically, or even making it infeasible to reach CO_2 purities down to the ppm level. The vertical mode of operation is nonetheless advantageous in practice since it has a much lower physical footprint than horizontal operation, especially on an offshore platform (Quek et al., 2018). As part of future work, it would be interesting, to use the MBC model for targeting improvements in the membrane material, amine solvent and operating conditions all together, in order for the vertical mode of operation to become viable in full-scale industrial applications. For instance, the graph in Figure 3.10B reports predictions of the CO_2 removal efficiency for (hypothetical) membranes having contact angles with the amine solvent in the range between 91.5º-94.0º. The efficiency increases steeply over this range, as a driven by a large reduction in membrane wetting. Moreover, the MBC model predicts that CO_2 removal efficiencies as large as those obtained in horizontal orientation could be obtained in the vertical pilot-scale module by using a PTFE membranes with higher hydrophobicity/contact angle.

3.6 Conclusions

This chapter has developed a mathematical model of high-pressure MBC using chemical solvents, which describes the effect of membrane pore-size distribution and operating conditions on membrane wetting and CO_2 absorption. A verification of the model has been conducted for both lab-scale and pilot-scale MBC modules, showing a close agreement of the predictions with measured CO_2 absorption flux at various gas and liquid flowrate, subject to a temperature correction to account for the heat of reaction in the liquid phase. Next, a model-based analysis of MBC for natural gas sweetening has been presented, with a focus on high-pressure operation and the effect of membrane wetting. The results confirm the advantages of a pressurized operation in terms of CO_2 removal efficiency. Moreover, a comparison between vertical and horizontal modes of operation has shown that the CO_2 removal efficiency in the latter can be vastly superior as it is not subject to the liquid static head. A vertical mode of operation could nonetheless become competitive if membrane materials with improved hydrophobicity were used.

A natural continuation of this work entails the development of MBC-based NG sweetening process model possible to analyze the effects of various absorption/desorption design configurations and operational decisions. These developments are the main focus in the following chapters of the thesis.

Chapter 4 Modeling of High-Pressure Membrane Contactors for Process-Wide Design and Operations.

4.1 Introduction

Chapter 3 has introduced a predictive mathematical model of high-pressure MBC using amine solvent and has experimentally verified its prediction under lean amine conditions. A natural continuation therefore entails using this model to predict the performance of a complete MBC-based process for NG sweetening, including solvent regeneration and losses, as well as hydrocarbon (HC) losses, in order to drive better process design and operation. Such an application of the MBC model, however, calls for further developments in order to accurately describe semi-lean operation, and a more systematic account of temperature variations in the MBC.

Most research work to date has neglected the effect of solvent evaporation on the MBC process performance. In practice, the gradual loss of solvent to the treated gas in the MBC can change the CO_2 absorption rate. So solvent make-up is required to maintain the desired solvent concentration, which can play an important role on the process economics. Ghasem et al. (2013) developed an MBC model that considers the amount of water evaporated from the solvent at various inlet absorbent temperatures and the corresponding latent heat of vaporization at atmospheric pressure. To the best of knowledge, no research to date has accounted for the solvent evaporation in the form of water, MDEA and PZ in MBC at high pressure. Therefore, the amount and the composition required for solvent make-up cannot be accurately quantified.

The amount of water evaporated from the solvent leads to a temperature drop of the solvent. Such a drop in the solvent temperature was predicted to increase with the inlet solvent temperature by Ghasem et al. (2013), due to the increased amount of water evaporated and latent heat of vaporization. Therefore, it is of interest to investigate the net effect of solvent evaporation and the exothermic reaction between CO_2 and the amines on the solvent temperature, especially in high-pressure MBC. The ability to predict the solvent temperature exiting the MBC is essential to design the heat exchangers at the solvent regeneration process accurately. Such modelling can also be used to identify potential temperature bulge along the MBC length, which is a phenomenon frequently observed in conventional CO_2 absorption

towers. Krishna and Wesselingh (1997) and Al-Baghli et al. (2001) reported that a temperature bulge is commonly located at the bottom of conventional absorber column, while Kvamsdal and Rochelle (2008) reported a temperature bulge located in the middle of the column, which might affect the mass transfer performance. Important factors like the CO_2 capture capacity and the corrosion rate directly depend on the temperature of the column.

The effectiveness of amines for CO_2 removal is well established (Paul et al., 2007; MacDowell et al., 2010). The Gas Processors Suppliers Association (2004) recommends maintaining the lean solution temperature at least 5°C above the hydrocarbon dew point temperature of the treated gas. The reason for this guideline is to prevent the condensation of hydrocarbons in the contactor and to avoid subsequent problems that a second liquid phase causes in an NG sweetening plant. Addington and Ness (2010) propose the same rule of thumb to prevent hydrocarbon condensation in the amine sweetening unit by keeping a minimum temperature difference of 5°C. Although HC condensation can be avoided, the physical absorption of the hydrocarbons into the amine solution is inevitable in practise (Carroll et al., 1998; Sánchez et al., 2009; Hatcher et al., 2013). Although usually quite small, any HC absorbed by the amine solvent that is not recovered will end up in the waste acid gas stream and therefore represents product loss. The presence of hydrocarbons in the acid gas stream also cause problems downstream of the MBC process, such as catalyst fouling in Clause reactors (Carroll et al., 1998).

Although the solubility of light HCs such as methane, ethane, and propane into the amine solvent is negligible at or near atmospheric pressure, it is known to increase by 10-30 fold when the pressure increases to 60 bar (Carroll et al., 1998). This finding is consistent with experiment result conducted by Kang et al. (2017), where the solubility of CH_4 in amine operating in MBC increase dramatically from 1 to 60 bar. To the best of knowledge, no research to date has considered HC absorption in MBC using amine solvent within mathematical models (Faiz & Al-Marzouqi 2010; Rezakazemi et al. 2011). Therefore, the extent of HC loss cannot be quantified accurately.

The main contribution of this chapter is a refinement of the model in Chapter 3 in order to enable the development of a plantwide model for an MBC-based process for NG sweetening. This refinement entails the modeling of solvent evaporation rate, energy balance, and hydrocarbon solubility in amine solvent. For the first time, the evaporation losses of water,

MDEA and PZ are distinguished, which is essential to identify and quantify the amount of solvent make-up required to maintain the concentration of the solvent in the MBC process and the subsequent scale-up and technical assessment (see Sec. 5.6 in Chapter 5). An energy balance is solved alongside the mass balance in the MBC model, that accounts for heat losses from solvent evaporation and the exothermic reaction between CO_2 and the amines. In addition, simple, conservative approach to estimating the physical absorption of methane, ethane and propane in amine solvent at different temperatures, pressures and concentrations is proposed using solubility data from the literature.

The predictive capability of this refined model is again tested against data from two experimental settings: a lab-scale MBC module, where the purification was conducted using binary gas mixtures of N_2/CO_2 at 54 bar; and a pilot-scale MBC module operated under industrially relevant conditions at a natural gas processing facility in Malaysia. All of the experiments were conducted with aqueous mixtures of MDEA and piperazine (PZ) as the chemical solvent and in a horizontal operation (Figure 4.1) based on the recommendations in Chapter 3. But compared to Chapter 3, a new hollow fiber membrane (HFM) was used in both the lab-scale and pilot-scale modules, which has a smaller outer radius and is braided to increase fiber length.

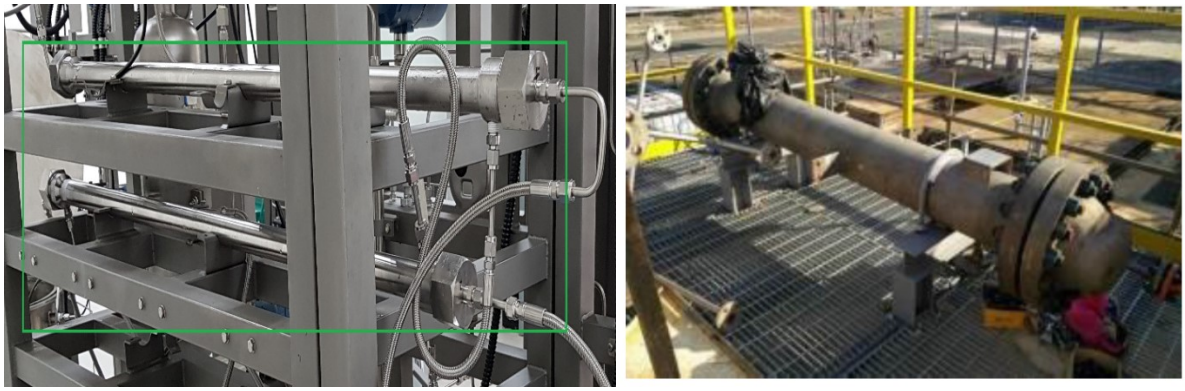

Figure 4.1: Horizontal MBC operation. **Left:** lab scale MBC; **Right:** pilot scale MBC

The rest of this chapter is organized as follows. The mathematical model of a horizontal counter-current hollow-fiber MBC module is summarized in Sec. 4.2, with a focus on the new developments to model the hydrocarbon absortive, solvent evaporative losses, and the temperaturate variations inside the MBC. A description of both experimental set-ups, corresponding model parameters, model-based design of the pilot-scale MBC, and

computational methods is given in Sec. 4.3. Results of the experimental model verification are presented and discussed in Sec. 4.4. Finally, Sec. 4.5 concludes the chapter.

4.2 Refinement and Extension of Hollow-Fiber MBC Model

The hollow-fiber MBC module under consideration is shown in the left-hand panel of Figure 4.2. The NG gas mixture containing CO_2 flows through the membrane fibers (at $z = L$), while the solvent flows inside the shell (at $z = 0$), in a counter-current configuration. The gas mixture diffuses from the tube side through the fiber walls into the shell, where CO_2 is chemically absorbed by the solvent to enhance the removal rate.

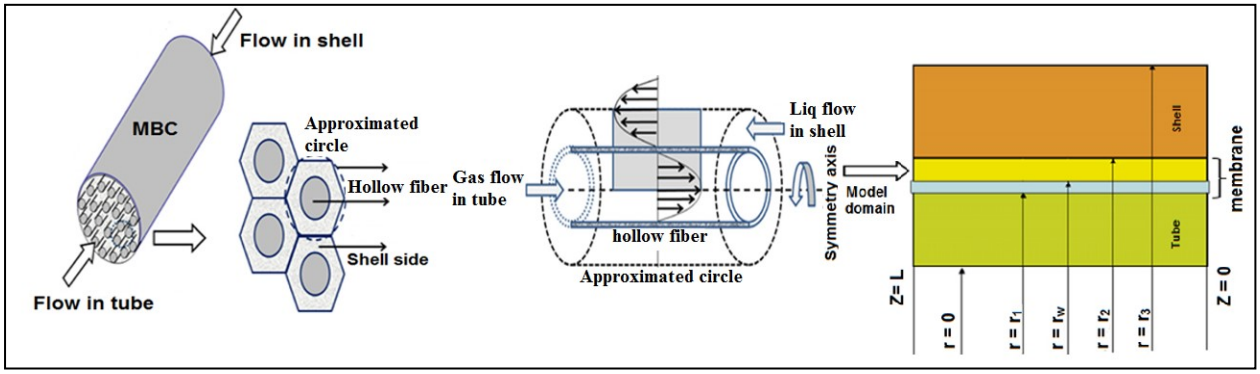

Figure 4.2: Schematic diagram of horizontal MBC with the four conceptual domains. **Left:** cylindrical approximation around each fiber. **Centre:** a single piece of the hollow fiber. **Right:** spatial domains in the MBC model.

4.2.1 Background

A full description of the modelling of membrane wetting and the underlying assumption was given in Sec. 3.2.1 of Chapter 3. A conceptual variable called wetted radius (r_w[m]) is introduced to represent the average fraction of membrane pores filled with liquid, in order to describe the degree of membrane wetting. Thus, the non-wetted and fully-wetted modes of operation correspond to $r_w = r_2$ and $r_w = r_1$, respectively, with r_1 and r_2 the inner and outer radius of the fibers. On exploiting symmetry, the spatial domain to model a piece of hollow fiber can be taken as $(r, z) \in [0, r_3] \times [0, L]$, which is further partitioned into four subdomains as shown on the right panel in Figure 4.2: (i) tube, $0 \le r \le r_1$; (ii) membrane-dry, $r_1 \le r \le r_w(z)$; (iii) membrane-wet, $r_w(z) \le r \le r_2$; and (iv) shell, $r_2 \le r \le r_3$. Notice that the geometry of the wetted and non-wetted membrane subdomains is complicated by the

dependence of the wetted radius on the axial position, z. As explained in Chapter 3, many factors are known to affect the degree of wetting, including the membrane-solvent combination, membrane properties such as contact angle (CA) and various operating parameters. In principle, membrane wetting could be prevented by keeping transmembrane pressure below a critical breakthrough pressure.

Mass conservation equations in the tube, membrane and shell sections of the MBC, together with the associated boundary conditions and underlying assumptions, were detailed in Sec. 3.2.2 of Chapter 3. These equations consider steady-state and isothermal operation in all phases, and are summarized in Table 4.1 for convenience. The following subsections detail the modeling of hydrocarbon absorption in solvent and solvent evaporative losses, and the energy balance to describe temperature variation inside the MBC. Full model equations for modeling of MBC in Chapter 4 are summarized in Appendix B (Table B.2).

4.2.2 Modeling of Light Hydrocarbon Losses

A first approximation, the solvent is assumed to be saturated with hydrocarbons at the MBC liquid outlet ($z = L$) and Henry's Law is used to estimate their concentrations:

$$C_{i,\mathrm{l}}^{\mathrm{out}} = \frac{\mathrm{y}_{i,\mathrm{g}}^{\mathrm{in}} P_{\mathrm{g}}}{H_{i,\mathrm{l}}}, \quad i \in \{\mathrm{CH_4}, \mathrm{C_2H_6}, \mathrm{C_3H_8}\}, \tag{4.1}$$

with the Henry's constant $H_{i,\mathrm{l}}$ $\left[\mathrm{m^3\ Pa\ mol^{-1}}\right]$, corresponding to the outlet solvent temperature, pressure and composition. Since the solvent inlet stream to the MBC does not contain any hydrocarbon, the loss rate in light hydrocarbons to the solvent is considered at the overall mass balance level (lumped) and readily obtained from

$$N_{i,\mathrm{l}}^{\mathrm{out}} = C_{i,\mathrm{l}}^{\mathrm{out}} F_{\mathrm{l}}, \quad i \in \{\mathrm{CH_4}, \mathrm{C_2H_6}, \mathrm{C_3H_8}\}, \tag{4.2}$$

The loss rate in Eq. (4.2) provides a worst-case scenario in estimating the amount of HC that is potentially lost if not recovered in the downstream flash drum. It is useful for benchmarking the HC losses compared to other conventional CO_2 removal technologies. The prediction of the $H_{i,\mathrm{l}}$ is detailed later in Material and Methods section (Sec 4.3.4.1) and the modeling approach is then verified experimentally in Results section (Sec. 4.4.2.2).

Table 4.1: Summary of mass conservation equations and boundary conditions.

Section	Material Balances
Gas Phase $(r,z) \in [0,r_1] \times [0,L]$:	$\frac{d\overline{C_{\mathrm{CO_2}}}(z)}{\partial z} = -\frac{2\,D_{\mathrm{CO_2,md}}}{\overline{v}_{\mathrm{g}}(z) r_1}\left[1 - \frac{ZRT_{\mathrm{g}}^{\mathrm{in}}\overline{C_{\mathrm{CO_2}}}(z)}{P_{\mathrm{g}}^{\mathrm{in}}}\right]\frac{\partial C_{\mathrm{CO_2}}(r,z)}{\partial r}\Big\vert_{r=r_1^+}$ $\frac{d\overline{v}_{\mathrm{g}}(z)}{\partial z} = -\frac{2\,D_{\mathrm{CO_2,md}}}{r_1}\frac{ZRT_{\mathrm{g}}^{\mathrm{in}}}{P_{\mathrm{g}}^{\mathrm{in}}}\frac{\partial C_{\mathrm{CO_2}}(r,z)}{\partial r}\Big\vert_{r=r_1^+}$
Membrane-Dry Phase $(r,z) \in [r_1, r_{\mathrm{w}}(z)] \times [0,L]$:	$D_{\mathrm{CO_2,md}}\left[\frac{\partial^2 C_{\mathrm{CO_2}}(r,z)}{\partial r^2} + \frac{1}{r}\frac{\partial C_{\mathrm{CO_2}}(r,z)}{\partial r}\right] = 0$
Membrane-Wet Phase $(r,z) \in [r_{\mathrm{w}}(z), r_2] \times [0,L]$:	$D_{\mathrm{i,mw}}\left[\frac{\partial^2 C_i(r,z)}{\partial r^2} + \frac{1}{r}\frac{\partial C_i(r,z)}{\partial r}\right] + R_i(C_i(r,z)) = 0, \quad i \in \{\mathrm{CO_2}, \mathrm{sol}\}$
Liquid Phase $(r,z) \in [r_2, r_3] \times [0,L]$:	$v_{\mathrm{l}}(r)\frac{\partial C_i(r,z)}{\partial z} = D_{i,\mathrm{l}}\left[\frac{\partial^2 C_i(r,z)}{\partial r^2} + \frac{1}{r}\frac{\partial C_i(r,z)}{\partial r} + \frac{\partial^2 C_i(r,z)}{\partial z^2}\right] + R_i(C_i(r,z)),$ $i \in \{\mathrm{CO_2}, \mathrm{sol}\}$ $v_{\mathrm{l}}(r) = 2\overline{v}_{\mathrm{l}}(r_3^2 - r_2^2)\frac{r^2 - r_2^2 + 2r_3^2 \ln\left(\frac{r_2}{r}\right)}{4r_2^2 r_3^2 - r_2^4 - 3r_3^4 - 4r_3^4 \ln\left(\frac{r_2}{r_3}\right)}, \quad \overline{v}_{\mathrm{l}} = \frac{F_{\mathrm{l}}^{\mathrm{in}}}{\pi R_{\mathrm{m}}^2(1-\emptyset)}$
Boundary Conditions	
Gas inlet, z=L:	$\overline{v}_{\mathrm{g}}(L) = \frac{M_{\mathrm{g}}^{\mathrm{in}}}{N\pi r_1^2 \rho_{\mathrm{g}}}, \qquad \overline{C_{\mathrm{CO_2}}}(L) = \frac{y_{\mathrm{CO_2,g}}^{\mathrm{in}} P_{\mathrm{g}}^{\mathrm{in}}}{ZRT_{\mathrm{g}}}$
Liquid inlet, z=0, $r \in [r_2, r_3]$:	$C_{\mathrm{CO_2}}(r,0) = f_{\mathrm{CO_2,l}}^{\mathrm{in}} C_{\mathrm{sol}}^{\mathrm{in}}, \quad C_{\mathrm{sol}}(r,0) = C_{\mathrm{sol}}^{\mathrm{in}}$
Liquid outlet z=L, $r \in [r_2, r_3]$:	$\frac{\partial C_i(r,z)}{\partial z}\Big\vert_{z=L} = 0 \qquad i \in \{\mathrm{CO_2}, \mathrm{sol}\}$
Gas-membrane Interface r=r_1, $z \in [0,L]$:	$C_{\mathrm{CO_2}}(r_1^+, z) = \overline{C_{\mathrm{CO_2}}}(z)$
Gas-liquid Interface r=$r_w(z)$, $z \in [0,L]$:	$C_{\mathrm{CO_2}}(r_{\mathrm{w}}^-(z), z) = \frac{H_{\mathrm{CO_2,l}}}{ZRT_{\mathrm{g}}} C_{\mathrm{CO_2}}(r_{\mathrm{w}}^+(z), z), \qquad \frac{\partial C_{\mathrm{sol}}(r,z)}{\partial r}\Big\vert_{r=r_{\mathrm{w}}^+(z)} = 0$ $D_{\mathrm{CO_2,md}}\frac{\partial C_{\mathrm{CO_2}}(r,z)}{\partial r}\Big\vert_{r=r_{\mathrm{w}}^-(z)} = D_{\mathrm{CO_2,mw}}\frac{\partial C_{\mathrm{CO_2}}(r,z)}{\partial r}\Big\vert_{r=r_{\mathrm{w}}^+(z)}$
Liquid-membrane Interface r=r_2, $z \in [0,L]$:	$C_i(r_2^+, z) = C_i(r_2^-, z), \quad i \in \{\mathrm{CO_2}, \mathrm{sol}\}$ $D_{i,\mathrm{l}}\frac{\partial C_i(r,z)}{\partial r}\Big\vert_{r=r_2^+} = D_{i,\mathrm{mw}}\frac{\partial C_i(r,z)}{\partial r}\Big\vert_{r=r_2^-}, \; i \in \{\mathrm{CO_2}, \mathrm{sol}\}$
Liquid Boundary r=r_3, $z \in [0,L]$:	$\frac{\partial C_i(r,z)}{\partial r}\Big\vert_{r=r_3}, \; i \in \{\mathrm{CO_2}, \mathrm{sol}\}$

4.2.3 Modeling of Solvent Evaporation in Treated Gas

Like with hydrocarbon losses before, it is assumed herein that the treated gas at the MBC outlet ($z = 0$) is saturated with solvent and the solvent evaporation rate is considered at the overall mass balance level (lumped). This assumption may overpredict the solvent evaporation rate due to the gas residence time being shorter than necessary to reach its equilibrium. Nevertheless, it is interesting to model the worst-case solvent evaporation rate to investigate the solvent loss in treated gas with respect to solvent circulation rate (See Sec. 4.4.3 for further discussion) and to benchmark the solvent rate loses in MBC system with a conventional packed column system (See Sec. 5.5.3 in Chapter 5).

For the vapour-liquid equilibrium at $z = 0$, Raoult's Law can be used to approximate the molar fraction of solvent in the gas outlet, $y_{i,\mathrm{g}}^{\mathrm{out}}\,[-]$ as

$$y_{i,\mathrm{g}}^{\mathrm{out}} = \frac{x_{i,\mathrm{l}}^{\mathrm{in}}\, P_i^{\mathrm{vap,in}}}{P_{\mathrm{g}}^{\mathrm{out}}}, \qquad i \in \{\mathrm{H_2O}, \mathrm{MDEA}, \mathrm{PZ}\} \tag{4.3}$$

where the terms $x_{i,\mathrm{l}}^{\mathrm{in}}[-]$, $P_i^{\mathrm{vap,in}}[\mathrm{kPa}]$, and $P_{\mathrm{g}}^{\mathrm{out}}[\mathrm{kPa}]$ are the molar fraction, the vapour pressures of species $i \in \{\mathrm{H_2O}, \mathrm{MDEA}, \mathrm{PZ}\}$ at liquid inlet, and the gas outlet pressure, respectively.

Since the gas inlet in a counter-current flow MBC is solvent free, the solvent loss rate, $N_{i,\mathrm{g}}^{\mathrm{out}}[\mathrm{mol\ s^{-1}}]$ is calculated as

$$N_{\mathrm{i,g}}^{\mathrm{out}} = N\pi r_1^2 \bar{v}_{\mathrm{g}}(0)\frac{y_{i,\mathrm{g}}^{\mathrm{out}} P_{\mathrm{g}}}{ZRT_{\mathrm{g}}}, \qquad i \in \{\mathrm{H_2O}, \mathrm{MDEA}, \mathrm{PZ}\} \tag{4.4}$$

4.2.4 Modeling of Solvent Temperature

Instead of using a simple temperature correction based on a lumped energy balance as in Chapter 3, a spatial distributed modelling of the solvent temperature is conducted here. This modelling accounts for heat losses due to solvent evaporation as discussed earlier in Sec. 4.2.3 and the exothermic reaction between CO_2 and the amines under adiabatic condition. For simplicity, the assumption is made that the solvent evaporation occurs at the liquid inlet (z =

0) before the solvent reacts with the CO_2 along the fiber length. It is noted that while solvent evaporation decreases the solvent temperature, CO_2 absorption increases the solvent temperature. Therefore, modeling of solvent temperature will provide insight on the relative contribution of each effect on solvent temperature. An experimental verification will confirm the validity of the modeling assumptions later in Sec. 4.4.1.

Based on the solvent evaporation rate determined in Eq. (4.4), the energy consumed for solvent evaporation, Q_{vap} [J s^{-1}] and the solvent temperature at shell inlet, $T_{\mathrm{l}}(0)$ can be determined as follows

$$Q_{\mathrm{vap}} = F_{\mathrm{l}}^{\mathrm{in}}\,\rho_{\mathrm{l}}\,C_{\mathrm{p}}\left(T_{\mathrm{l}}^{\mathrm{in}} - T_{\mathrm{l}}(0)\right) = \overline{v_{\mathrm{g}}}(0)N\pi r_1^2 \sum \frac{x_{i,\mathrm{l}}^{\mathrm{in}}\,P_i^{\mathrm{vap,in}}}{ZRT_{\mathrm{g}}}\,\Delta H_i^{\mathrm{vap}}\left(T_{\mathrm{l}}^{\mathrm{in}}\right) \tag{4.5}$$

where $F_{\mathrm{l}}^{\mathrm{in}}$ [$\mathrm{m}^3\ \mathrm{s}^{-1}$] ρ_{l} [kg m^{-3}], C_{p}[J kg^{-1} K^{-1}] , $T_{\mathrm{l}}^{\mathrm{in}}$ [K] and $\Delta H_i^{\mathrm{vap}}$ [J mol^{-1}] , are solvent inlet volumetric flowrate, density, specific heat capacity, inlet temperature and the latent heat of vaporization of species $i \in \{\mathrm{H_2O}, \mathrm{MDEA}, \mathrm{PZ}\}$, respectively. The specific heat capacity of the amine solvent and the latent heat of vaporization are set to $C_{\mathrm{p}} = 3600$ J kg^{-1} K^{-1} (Weiland, Dingman, Cronin, *et al.*, 1997) and $\Delta H_{\mathrm{H_2O}}^{\mathrm{vap}} = 12688$, $\Delta H_{\mathrm{MDEA}}^{\mathrm{vap}} = 62120$, and $\Delta H_{\mathrm{PZ}}^{\mathrm{vap}} = 38750$ J mol^{-1}(Engineering ToolBox, 2010; Chemeo, 2017), respectively.

Diffusive heat transfer in the shell is fast enough (Péclet > 10^4), and therefore thermal diffusion along the axis may be neglected. Furthermore,the solvent temperature is assumed to be homogeneous in the radial direction. This leads to the following energy balance for quantifying the solvent temperature rise, $T_{\mathrm{l}}(z)$ along the fiber length by accounting for the exothermic CO_2 absorption reaction under adiabatic conditions:

$$F_{\mathrm{l}}^{\mathrm{in}}\,\rho_{\mathrm{l}}\,C_{\mathrm{p}}\,\frac{dT_{\mathrm{l}}(z)}{dz} = -\pi r_1^2 N\,\frac{d\left(\overline{v_{\mathrm{g}}}(z)\overline{C_{\mathrm{CO_2}}}(z)\right)}{dz}\Delta H_{\mathrm{r}} \tag{4.6}$$

where the enthalpy of reaction is set to $\Delta H_{\mathrm{r}} = -60000$ J mol^{-1} (Kabadi, 2007).

Notice that Eq. (4.6), which is now refined to be in spatial distributed modelling compared to the lumped-energy balance in Eq. (3.40) used in Chapter 3. The predicted value of $T_l(0)$ in Eq. (4.5) provides the boundary condition at $z = 0$ for Eq. (4.6).

4.3 Material and Methods

4.3.1 Experimental Setups

The lab-scale module experiments were conducted with a binary feed gas mixture of N_2/CO_2 at 54 bar. The pilot module was operated under industrially relevant operating conditions, also at 54 bar in a natural gas processing plant in Malaysia. In both cases, aqueous mixtures of methyldiethanolamine (MDEA) and piperazine (PZ) were used as the chemical solvent. The corresponding operating and design conditions in the lab and the pilot plant are summarized in Table 4.2.

Table 4.2: Operating and design conditions in the lab and pilot plant

Parameters	N_2/CO_2 (Lab)	NG (Pilot)
CO_2 inlet, $y^{in}_{CO_2,g}$ [mol%]	20-24	5-18
MDEA/PZ inlet, [wt%]	37/6	39/5
Inlet gas pressure, P_g^{in} [kPa]	5400	5400
Outlet liquid pressure, P_l^{out} [kPa]	5430	5430
Gas mass flowrate, M_g^{in} $[kg\ h^{-1}]$	2-3	50-75
Liquid volumetric flowrate, F_l^{in} $[L\ h^{-1}]$	8-10	175-275
Gas temperature, T_g^{in} [K]	293	298
Liquid temperature, T_l^{in} [K]	310-313	303-308
CO_2 loading in solvent, $f^{in}_{CO_2,l}$ $[mol\ mol^{-1}]$	0.01-0.23	0.01-0.23

Lab-Scale MBC Module

The experimental setup for lab-scale testing is identical to the set-up detailed earlier in Sec. 3.3.1. The main difference is that the MBC is now oriented horizontally, based on the findings in Chapter 3 (see Figures 4.3).

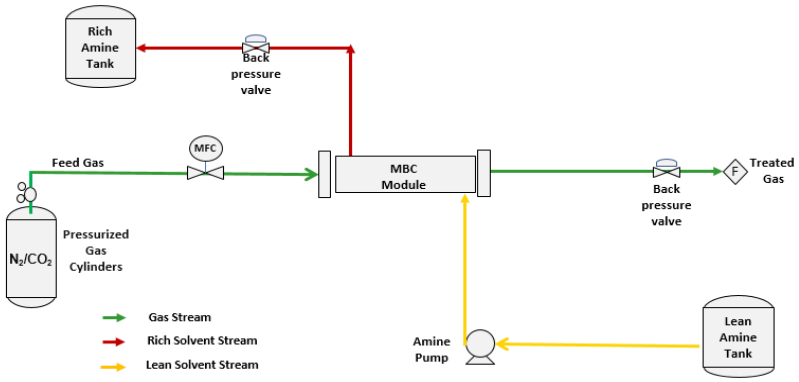

Figure 4.3: Schematic of the lab-scale setup for CO_2 removal using a horizontal MBC.

Pilot-Scale MBC Module

The experimental setup for pilot-scale testing is also similar to the setup described in Sec. 3.3.1, again with the difference of a horizontal MBC module (see Figure 4.4). The CO_2 loading was increased gradually during the experiments, starting with lean operation ($f^{in}_{CO_2,l} = 0.01$). This was achieved by reducing the heat input into the electrical reboiler to obtain a higher CO_2 loading in the solvent. Once the plant had reached a steady-state at a particular reboiler energy duty, the lean amine was sampled and analyzed for its CO_2 content and loading before reducing the reboiler energy duty further. During the experiments, parameters such as CO_2 inlet, feed gas and amine flowrates were kept constant and the gas compositions in the MBC feed, outlet and the flash gas were analyzed and recorded using gas chromatography (PGC1000 Gas Chromatograph, ABB) every 6 minutes, after the system had reached steady state. In addition, pure CO_2 from a pack of cylinders was blended into the feed gas line to enable high CO_2 experiments (up to 18%). The fluid flowrates and gas compositions values were averaged hourly and compared with model predictions.

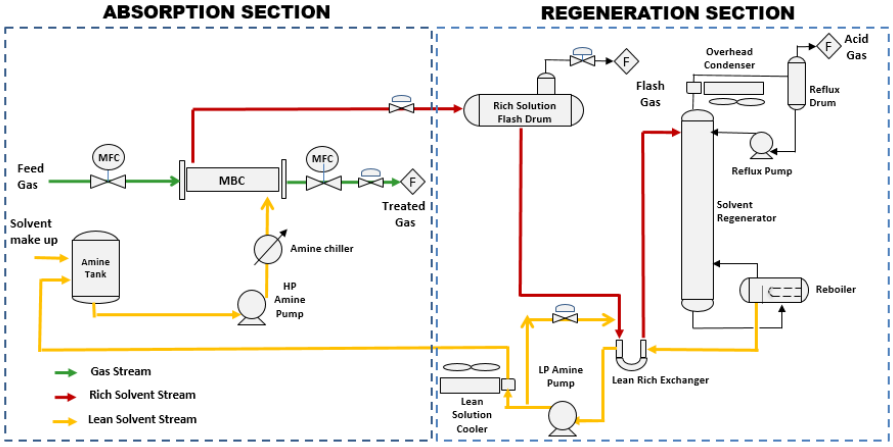

Figure 4.4: Schematic of the pilot-plant setup for CO_2 removal using a horizontal MBC.

4.3.2 Membrane Characteristics

The high-pressure MBC modules were packed with hydrophobic, Polytetrafluoroethylene (PTFE) hollow fiber. Table 4.3 reports the main characteristics and geometrical properties of the MBC used for lab- and pilot-scale testing.

It is important to note that a new hollow fiber membrane (HFM) was used to conduct the lab and pilot scale experiments in this chapter, compared to the HFM in Chapter 3. The new membrane has a smaller fiber outer radius and membrane thickness, and the length of the fibers is also increased by about 15% due to braiding of the fibers inside the MBC module – see Table 3.2 and Table 4.3 for comparison.

Table 4.3: Specifications of the lab- and pilot-scale membranes.

Parameters	**Lab module**	**Pilot module**	**Source**
Fiber length, L [m]	2.3	2.3	(PRSB, 2016)
Fiber inner radius, r_1 [μm]	225	225	(PRSB, 2016)
Fiber outer radius, r_2 [μm]	550	550	(PRSB, 2016)
Membrane porosity, ε [$-$]	0.41	0.41	(PRSB, 2016)
Membrane tortuosity, τ [$-$]	6.1	6.1	Eq. (3.31)
Max. pore radius, $\delta_{\max}$ [μm]	0.18	0.18	(PRSB, 2016)
Mean pore radius, $\bar{\delta}$ [μm]	0.06	0.06	Eq. (3.32)
Pore standard deviation, σ [$-$]	0.24	0.24	Eq. (3.32)
Contact angle, θ [°]	92.4	92.4	(PRSB, 2016)
Packing density, $\emptyset$ [$-$]	0.40	0.38	Sec. 4.3.3
Module inner radius, R_{m} [m]	0.0125	0.115	(PRSB, 2016)
Membrane area, A_{m} [m^2]	1.67	68	Sec. 4.3.3
No of fibers, N	209	8400	(PRSB, 2016)
Specific surface area [m^{-1}]	1700	1600	(PRSB, 2016)
Outer radius of tube insert, R_{t} [m]	N/A	0.08	Sec. 4.3.3

Following the same approach as in Sec. 3.3.2, pore-size distribution (PSD) data from the manufacturer (PRSB, 2014) were used to fit the log-normal distribution in Eq. (3.32). The resulting least-squares fit in Figure 4.5A shows an excellent agreement with the data, and the corresponding estimate for $\bar{\delta}$ and σ can be found in Table 4.3. In turn, a surrogate relationship for the wetting ratio $\mathfrak{z}$ as a function of the critical pore radius δ_w in the range $[0, \delta_{max}]$ could be obtained in the form of Eq. (3.33), with $a_0 = 9.029$, $a_1 = -17.209$, $a_2 = 11.222$, and $a_3 = -2.938$. A comparison between the actual wetting ratios in Eq. (3.9) and the fitted surrogate in Eq. (3.33) is shown on Figure 4.5B.

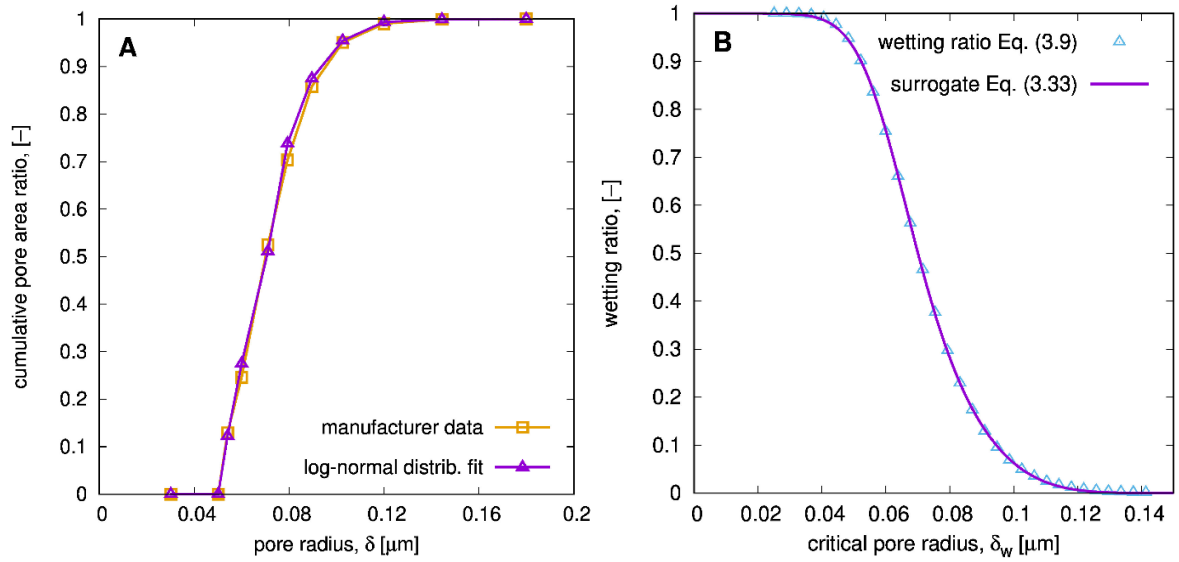

Figure 4.5: A: Comparison of cumulative pore area ratio distribution based on the log-normal pore size distribution in Eq. (3.32) using the parameters in Table 4.3, against the manufacturer (PRSB, 2014) data. **B:** Comparison of the wetting ratio expression in Eq. (3.9) with the fitted surrogate expression in Eq. (3.33) in terms of the critical pore radius δ_w.

4.3.3 Pilot-scale Module Design

The characteristics of the new HFM as well as the braiding (see Figure 4.6A) are expected to greatly increase the pilot-scale gas treating capacity due to an increase in specific surface area from ca. 1300 m^{-1} (see Table 3.2) to ca. 2300 m^{-1} for the same packing density ($\emptyset = 0.55$). However, the pilot plant cannot operate at a gas flowrate higher than 75 kg hr^{-1} due to limitations in other parts of the plant. As a result, operating the pilot plant at design capacity with the new membrane in a horizontal operation (see Sec. 3.5.2) would result in CO_2 removal efficiency close to 100% in most experiments. Therefore, this subsection seeks to design a new pilot module, that would achieve a CO_2 purity of 50 ppmv at the full capacity. In order to

maintain packing density in the new module close to 0.55, the module cross-sectional area was scaled down by inserting a steel tube at the center of the module (see Figure 4.6B). The packing density, $\emptyset$ and membrane area, A_m are given by

$$\emptyset = \frac{r_2^2 N}{R_m^2 - R_t^2} \quad , \tag{4.7}$$

$$A_m = 2\pi r_2 L N \quad , \tag{4.8}$$

where N is the number of fibers in the MBC module; R_m [m] and R_t [m] are the inner radius of the module and the outer radius of the steel tube insert, respectively; and L is the fiber length.

Figure 4.6: A: Braided HFM to increase the fiber length by 15% (i.e., from 2 to 2.3 m); **B:** cross-section of pilot-scale module with steel tube insert in the center to reduce the total membrane area.

Figure 4.7A shows the required outer radius of the steel tube insert for different membrane areas in order to maintain a packing density of 0.55. The results in Figure 4.7B show the predicted CO_2 absorption flux, Φ [mol m^{-2} s^{-1}] and CO_2 outlet gas purity, $y_{CO_2,g}^{out}$ [ppmv] for different membrane areas at the maximum pilot capacity (M_g^{in} = 75 kg h^{-1}, F_l^{in} = 275 L h^{-1}, $y_{CO_2,g}^{in}$ = 5 mol%). These predictions are computed with the original model in Chapter 3, using the new membrane properties in Table 4.3.

The model predicts a CO_2 outlet gas purity lower than 50 ppmv in cases of total membrane area above 80 m^2, with negligible wetting for all the cases due to horizontal operation. Notice also that the CO_2 absorption flux decreases with larger membrane area, given that the membrane area is already large enough for the CO_2 outlet purity to be at the ppm level.

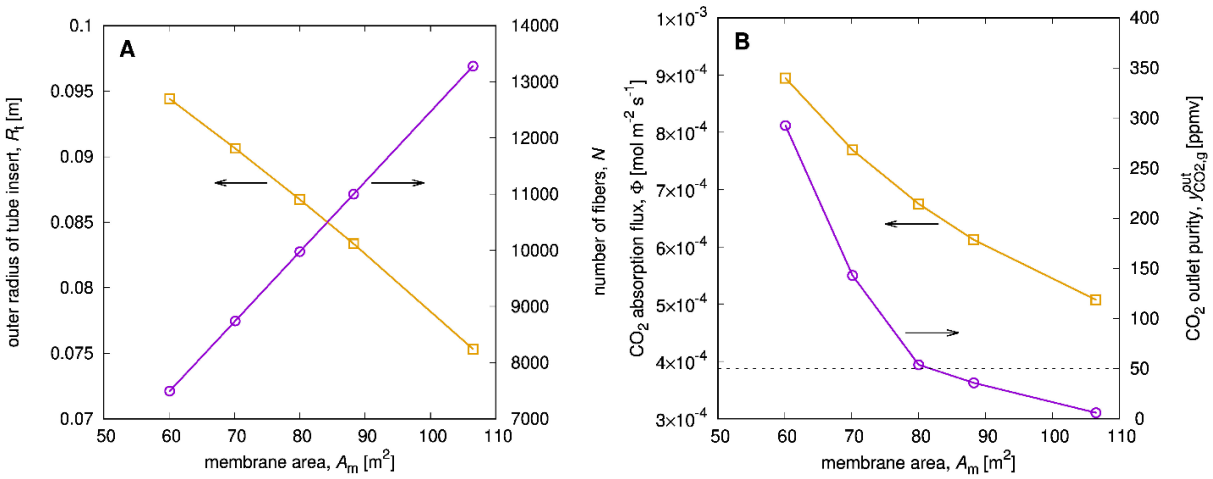

Figure 4.7: A: Predicted total number of fibers and outer radius of steel insert; **B:** Predicted CO_2 outlet gas purity and absorption flux at different membrane area, while maintaining the packing density of 0.55.

However, due to the rigid steel tube and braided structure of the HFM, only 8400 fibers could be successfully installed in practice with a tube insert of radius, $R_t = 0.08$ m compared to the required ca. 11,000 fibers. This configuration yields a packing density of only 0.38 and a reduced surface area of 68 m^2, as reported in Table 4.3. Nonetheless, it was decided to use this module configuration for all the pilot-scale tests (Sec. 4.4.2).

4.3.4 Thermo-Physical, Transport, and Reaction Kinetic Data

This subsection starts by discussing the prediction of Henry's constant for light hydrocarbon in amine solvent needed to estimate hydrocarbon losses (Sec. 4.3.4.1), and then the prediction of Henry's constant for CO_2 in semi- lean amine solvent (Sec. 4.3.4.2). Other temperature-dependent expressions for (i) the macroscopic reaction rates of CO_2 with MDEA and PZ, and (ii) the diffusivity coefficients of the various species in gas or liquid mixtures are reported in Appendix A (Table A.2) for completeness. The remaining thermo-physical and transport parameters are obtained by interfacing gPROMS with the property packages 'Advanced Peng Robinson', and 'UNIQUAC-RK' for the gas and liquid phases, respectively.

4.3.4.1 Prediction of Light Hydrocarbon Solubility in Amine Solvent

The solubility of methane, ethane and propane in water and in aqueous amine solutions of 50 wt% MDEA were gathered from the solubility charts by Carroll et al. (1998). These charts were derived from a combination of thermodynamic modeling (*i.e.* Peng-Robinson Equation of State and Henry's Law) and experimental data.

The following polynomial regression model for Henry's constant for light hydrocarbon in amine solvent, $H_{i,\mathrm{l}}$ $i \in \{\mathrm{CH_4}, \mathrm{C_2H_6}, \mathrm{C_3H_8}\}$ was fitted to this data set: for temperature range of 300-345 K and pressure in the range of 48-72 bar. The regression model is developed using Design-Expert version 11.

$$H_{i,\mathrm{l}} = \alpha_0 + \alpha_1 C + \alpha_2 T_\mathrm{l} + \alpha_3 P_\mathrm{l} + \alpha_4 C T_\mathrm{l} + \alpha_5 C P_\mathrm{l} + \alpha_6 T_\mathrm{l} P_\mathrm{l} \tag{4.9}$$

where T_l [K], P_l [Pa], and C [-] are the liquid temperature, liquid pressure and the mass fraction of MDEA in aqueous amine solvent, respectively. The coefficients α_1 to α_8 for each Henry's constants and absolute average deviations are given in Table 4.4. A comparison between the experimental and predicted Henry's constants is presented in Figure 4.8, showing excellent agreement in terms of deviation with most predictions being between ±5 %. The resulting Henry's constants surrogates Eq. (4.9) will be used to predict the hydrocarbon worst-case losses, as proposed in Sec. 4.2.2.

Table 4.4: Coefficients for $H_{i,\mathrm{l}}$, and absolute average deviations

$H_{i,\mathrm{l}}$	$H_{\mathrm{CH_4,l}}$ $\left[\mathrm{m^3\ Pa\ mol^{-1}}\right]$	$H_{\mathrm{C_2H_6,l}}$ $\left[\mathrm{m^3\ Pa\ mol^{-1}}\right]$	$H_{\mathrm{C_3H_{8,l}}}$ $\left[\mathrm{m^3\ Pa\ mol^{-1}}\right]$
α_0	-2.90×10^5	-5.97×10^5	-1.67×10^5
α_1	3.56×10^5	8.12×10^5	9.50×10^5
α_2	1.26×10^3	2.01×10^3	7.34×10^2
α_3	2.40×10^{-2}	5.63×10^{-2}	1.40×10^{-1}
α_4	-1.42×10^3	-2.72×10^3	-3.44×10^3
α_5	4.41×10^{-3}	-1.95×10^{-2}	-8.89×10^{-2}
α_6	-7.43×10^{-5}	-1.16×10^{-4}	-1.96×10^{-4}
AAD (%)	1.8	1.5	3.0

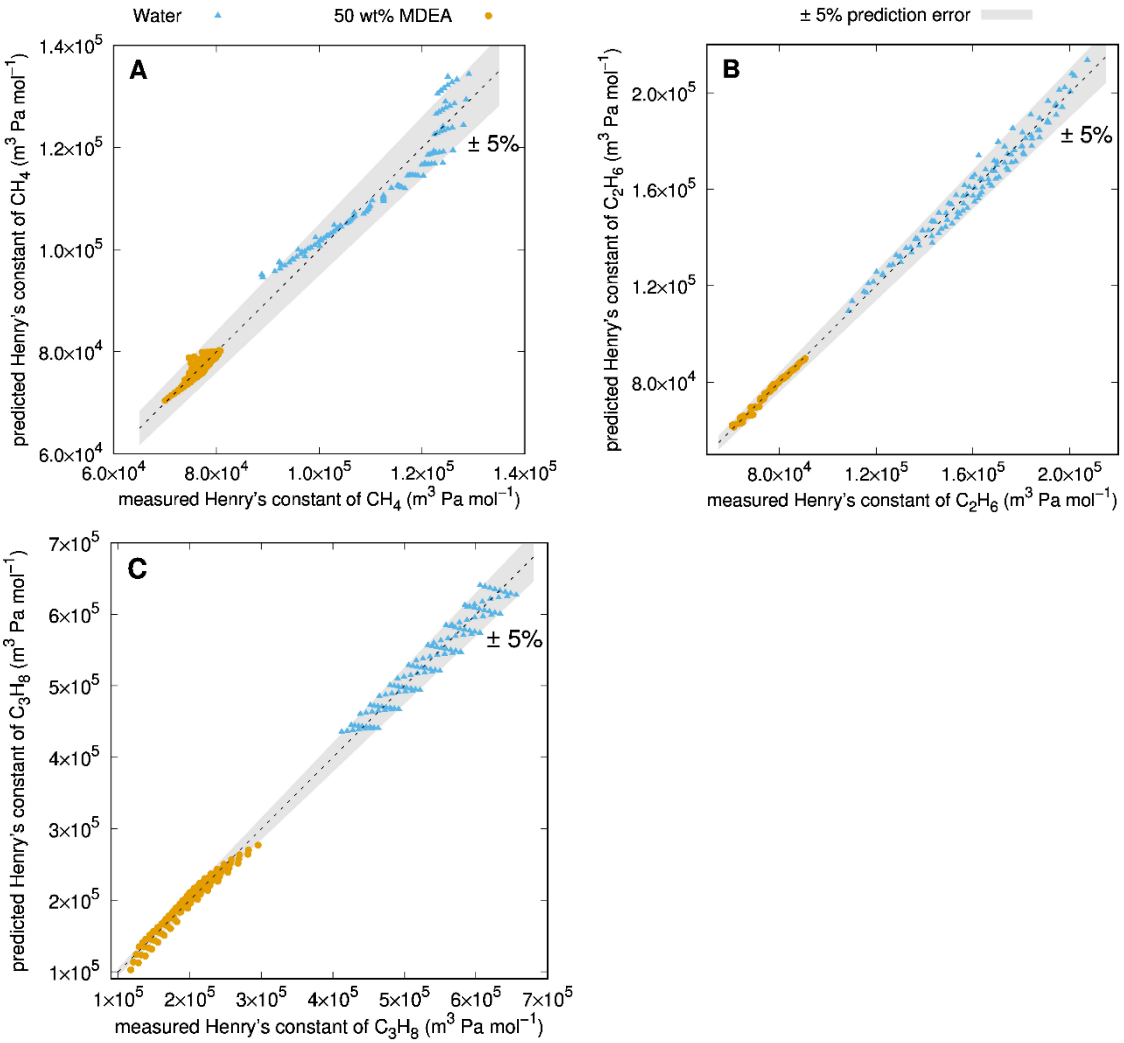

Figure 4.8: Predicted Henry's constant using Eq. (4.9) against the experimental data in water (blue points) and 50 wt% aqueous MDEA (orange points) from Carroll et al. (1998). **A:** $H_{\mathrm{CH_4,l}}$; **B:** $H_{\mathrm{C_2H_6,l}}$; **C:** $H_{\mathrm{C_3H_8,l}}$

4.3.4.2 Prediction of Henry's constant in semi-lean amine solvent

To account for the effect of CO_2 loading in amine solution, a regression model is developed based on empirical data of N_2O solubility in aqueous solution 50wt% of MDEA for CO_2 loading and temperature in the range of 0-0.5 mol mol^{-1} and 295-353 K, respectively (Park and Sandall, 2001). Here, the effect of pressure on Henry's constant is neglected, and assume that PZ behaves like MDEA.The regressed Henry's constant for N_2O is given by:

$$H_{N_2O,l} = -3.30 \times 10^4 - 3.79 \times 10^4 f^{in}_{CO_2,l} + 1.70 \times 10^2 T_l - 4.37 \times 10^3 (f^{in}_{CO_2,l})^2 - 1.34 \times 10^{-1} T_l^{\,2} + 1.45 \times 10^2 f^{in}_{CO_2,l} T_l \quad (4.10)$$

where $f^{in}_{CO_2,l}$ and T_l are inlet CO_2 loading in amine and liquid temperature, respectively.

The comparison in Figure 4.9A between the experimental and the predicted $H_{N_2O,l}$ based on the surrogate in Eq. (4.10) shows good agreement. It can be seen in Figure 4.9B that Eq. (3.37), developed for lean-amine solvent, predicts lower $H_{N_2O,l}$ compared to Eq. (4.10) for all CO_2 loadings. A higher value of $H_{N_2O,l}$ results in a higher $H_{CO_2,l}$ based on Eq. (3.34), and in turn a lower CO_2 solubility in the solvent. In addition, the gradient increase of $H_{N_2O,l}$ using Eq. (3.37) is higher compared to Eq. (4.10), which confirms the adverse effect of a higher CO_2 loading on the CO_2 absorption flux.

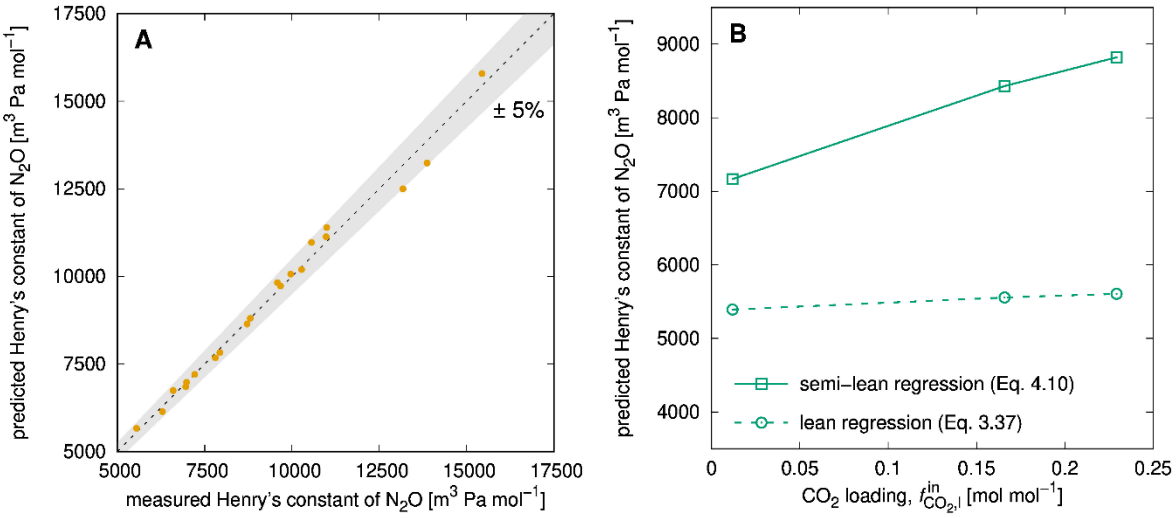

Figure 4.9: A: Comparison of the experimental data of $H_{N_2O,l}$ against the surrogate predictions by Eq. (4.10); **B :** Predicted $H_{N_2O,l}$ at various CO_2 loading using Eq. (3.37) for lean amine and Eq. (4.10) for semi-lean amine.

4.4 Experimental Model Verification and Analysis

4.4.1 Lab-Scale MBC Module

A comparison between measured and predicted CO_2 absorption fluxes, Φ [mol m^{-2} s^{-1}] is presented in Figure 4.10A-C using the Henry's constant in Eq. (4.10) that was regressed in both lean and semi-lean solvent. A comparison is also made with the predictions using Eq. (3.37). The experimental data are for different CO_2 loadings in solvent (0.01-0.24 mol mol^{-1}) and different gas and amine flow rates (see Table 4.2). It can be seen that model predictions using Eq. (4.10) are in close agreement with the experimental CO_2 fluxes. Predictions using Eq. (3.37) are found to be in relatively good agreement with the measurements still, albeit showing larger and more systematic errors of up to 10% overestimation, particularly at higher CO_2 loading experiments. This systematic offsets between predictions and measurements is due to Eq. (3.37) only accounting for lean amine, thereby overestimating the CO_2 solubility in the semi-lean solvent. Although Eq. (4.10) predicted higher value of $H_{N_2O,l}$ by approximately 25% for the lean amine (Figure 4.9B), the effect on the CO_2 absorption flux is not as significant compared to higher CO_2 loading cases as shown in Figure 4.10A. A possible explanation is that the diffusive mass transfer in the lean amine solution dominates over the CO_2 dissolution at the gas-liquid interface.

The MBC model correctly predicts that a larger CO_2 loading in the solvent feed decreases the CO_2 absorption flux (Figure 4.10A). An increase in liquid CO_2 loading essentially results in a decrease in free amine available to react with CO_2. And, from a thermodynamics viewpoint, the solubility of CO_2 in the liquid decreases with an increase in the liquid CO_2 loading due to higher value of $H_{N_2O,l}$, thus higher $H_{CO_{2,l}}$ based on Eq. (3.34) (see Figure 4.9B). The model predicts an average wetting in the range between 2 to 6% as the CO_2 loading varies. In particular, an increase in CO_2 loading increases membrane wetting due to the reduction in liquid surface tension, as per Young-Laplace equation (see Chapter 3, Sec 3.2.1), thereby causing a reduction of the CO_2 flux through the membrane.

The model also correctly predicts the increase in CO_2 absorption flux with a larger inlet gas flowrate (Figure 4.10B), driven by a larger amount of CO_2 in the gas feed. Note that, since the pressure drops in the tubes is negligible, increasing the inlet gas flowrate has minimal effect on the wetting ratio (a mere increase of 0.2% wetting here).

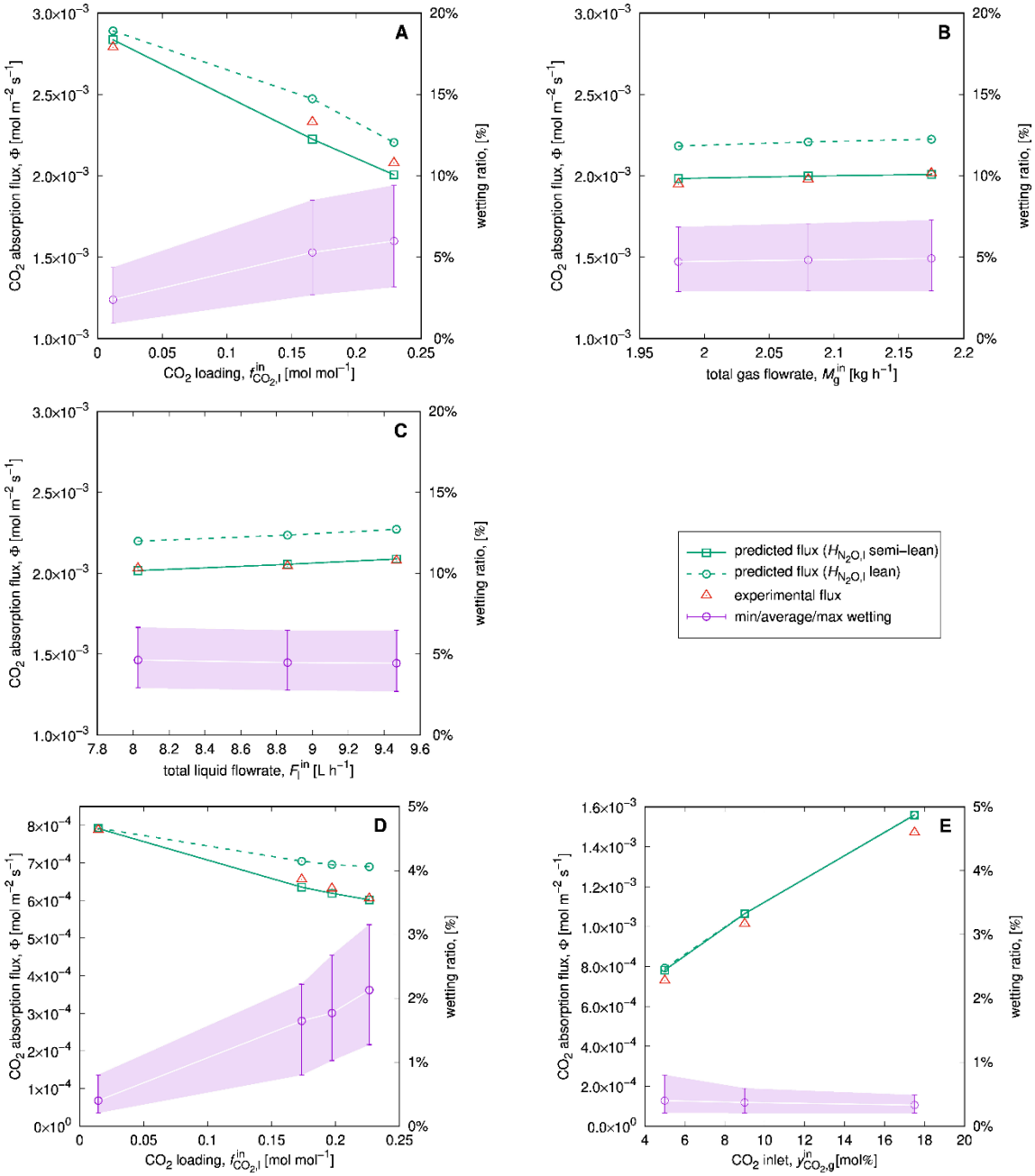

Figure 4.10: Predicted CO_2 absorption fluxes against experimental data in lab-scale **(A-C)** and pilot-scale **(D-E)** MBC, together with predicted membrane wetting. **A**: effect of $f^{in}_{CO_2,l}$ for fixed M^{in}_g = 3 kg h^{-1}, F^{in}_l =10 L h^{-1} and $y^{in}_{CO_2,g}$ = 20 mol% ; **B**: effect of M^{in}_g for a fixed F^{in}_l =10 L h^{-1} , $f^{in}_{CO_2,l}$ = 0.22 mol mol^{-1} and $y^{in}_{CO_2,g}$ = 24 mol%; **C**: effect of F^{in}_l for a fixed M^{in}_g = 2 kg h^{-1}, $f^{in}_{CO_2,l}$ = 0.2 mol mol^{-1} and $y^{in}_{CO_2,g}$ = 24 mol%; **D:** effect of $f^{in}_{CO_2,l}$ for fixed M^{in}_g = 75 kg h^{-1}, F^{in}_l= 275 L h^{-1} and $y^{in}_{CO_2,g}$ = 5 mol%; **E:** effect of $y^{in}_{CO_2,g}$ for a fixed $f^{in}_{CO_2,l}$ of 0.01 mol mol^{-1}, M^{in}_g = 50-75 kg h^{-1}, F^{in}_l= 180-275 L h^{-1}.

The model correctly captures the improvement in CO_2 absorption flux on increasing the solvent flowrate (Figure 4.10C), with a corresponding small decrease in the membrane wetting. An increase of liquid flowrate leads to a higher pressure drop, transmembrane pressure and membrane wetting, similar to the phenomena explained in Chapter 3 (Sec 3.4.2). But at higher liquid flowrate, the temperature increase in the solvent due to a higher CO_2 absorption is lower, which results in a relatively higher liquid surface tension, and therefore a lower membrane wetting. On balance, the model correctly predicts that the effect of a higher pressure drop on membrane wetting is small in comparison with the increase in liquid surface tension. The effect of a larger concentration gradient due to an increase in velocity also contributes to increasing the overall CO_2 absorption.

It can be seen from Figure 4.11 the predicted solvent temperature profile along the fiber length is in excellent agreement with the measured solvent temperature, which provides a first validation of the assumption made in the energy balance (Sec. 4.2.4). In this experiment, it appears that there is no significant temperature bulge in the MBC module. The model can be used to identify potential temperature bulge along the MBC length at different operating conditions. Notice also that the temperature rise (ca. 20 K) is significant compared to the lab-scale (ca. 3-4 K) in Sec. 3.4.3, where the L/G ratio (ca. 0.86 m^3 $kmol^{-1}$) was four-time lower in order to be comparable to values of 0.6 – 1.1 m^3 $kmol^{-1}$ typically encountered in conventional packed column (Park et al., 2004; Rezazadeh et al., 2016; Gaspar et al., 2017).

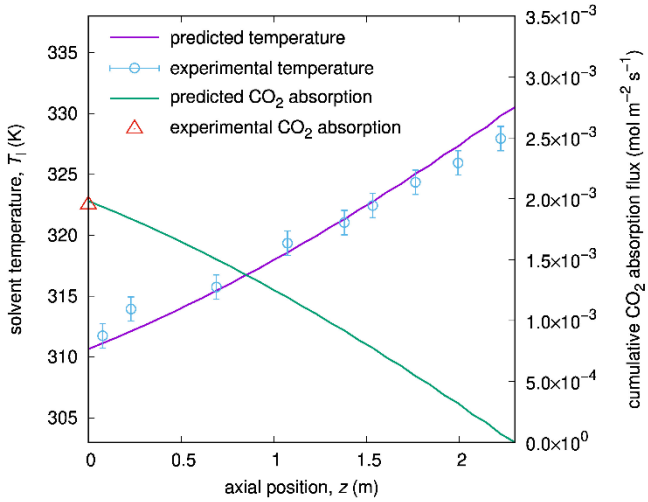

Figure 4.11: Relationship between the CO_2 removal rate and the temperature profile in solvent along the module length for gas and solvent flowrates and CO_2 loading of 2 kg h^{-1} , 10 L h^{-1} and 0.22 mol mol^{-1}, respectively.

The predicted cumulative CO_2 absorption flux in Figure 4.11 is 0 at the gas inlet (z=2.3 m) and increases along the fiber axis. The CO_2 absorption flux presents a slow decrease from the gas inlet to the gas outlet (concave shape), which is expected since the higher CO_2 concentration near the gas inlet enhances the mass transfer of CO_2 through the membrane. Likewise, the temperature rise is higher near the gas inlet (convex shape) due to more heat released being released from the CO_2 absorption in amine solvent.

4.4.2 Pilot-Scale MBC Module

4.4.2.1 Model verification of CO_2 absorption fluxes with experimental data

A similar comparison between measured and predicted CO_2 absorption fluxes in the pilot-scale MBC module is presented in Figure 4.10D-E. The experimental data are for different CO_2 loadings in solvent (0.01-0.23 mol mol^{-1}) and different gas and amine flow rates (see Table 4.2). The model predictions using Eq. (4.10) to predict CO_2 solubility are in close agreement with the CO_2 absorption fluxes in Figure 4.10D, while the predictions using Eq. (3.37) result in a similar 10% overestimation at higher CO_2 loading experiments, due to neglecting the effect of CO_2 loading in amine solvent as already discussed in Sec. 4.4.1.

Consistent with lab-scale results, the MBC model correctly predicts that a larger CO_2 liquid loading reduces the CO_2 absorption flux (Figure 4.10D) due to a decrease in free amine available to react with CO_2. And, an increase in the CO_2 liquid loading decreases the solubility of CO_2 in the liquid (Figure 4.9B) and the liquid surface tension, thereby causing extra wetting and therefore a reduction in the CO_2 flux through the membrane.

Experimental data corresponding to different CO_2 inlet concentration in NG mixture and a lean amine are considered in Figure 4.10E. The model correctly captures again the improvement in CO_2 absorption flux on the increasing CO_2 inlet concentration. This improvement is driven by the higher CO_2 concentration gradient which increases mass transfer in MBC. The model also predicts a negligible membrane wetting due to the horizontal orientation (see Sec 3.5.2) and operation with a lean amine. By comparing the first experiment point on Figure 4.10D to the third point in Figure 3.8A, which correspond to the same inlet CO_2 concentration, gas and liquid flowrates, it is seen that the CO_2 absorption flux has improved by nearly 80% and the membrane wetting has reduced to less than 1% by using the new HFM module in horizontal orientation compared to HFM vertical module of Chapter 3.

4.4.2.2 Estimation of hydrocarbon lost in high-pressure MBC for NG sweetening

A comparison between the predicted and measured molar flowrates of light hydrocarbons in the flashed gas is presented in Figure 4.12, at different solvent flowrates. It can be seen that the all of the predicted molar flows for methane and ethane are within 15% of the measurements. This validates the assumption that the solvent is about saturated with hydrocarbons at the MBC outlet (Sec. 4.2.2). On the other hand, the predicted molar flows of propane underestimate the measurements by a factor of 2 to 3, which could be due to these flowrates are relatively small, therefore are susceptible to experimental error.

On the other hand, the model correctly captures the increase in HC absorption on increasing the solvent flowrate against experimental data, as shown in Eq. (4.2). The increase in HC absorption is attributed to a higher concentration gradient in the solvent, which improves mass transfer. Model further predicted that the methane losses are an order of magnitude higher than ethane and higher hydrocarbon losses as shown in Figure 4.12. This was expected as the feed gas to the pilot plant contains 85 mol% of methane, and that methane has a higher solubility of in amine than ethane and higher hydrocarbons (Figure 4.8). Overall, the predictions provide the correct order of magnitude for the HC loss with small loss rates of ca. 1% for the experimented solvent flowrates. Therefore, similar modelling approach will be used in a techno-economic assessment (see Sec. 5.6 in Chapter 5).

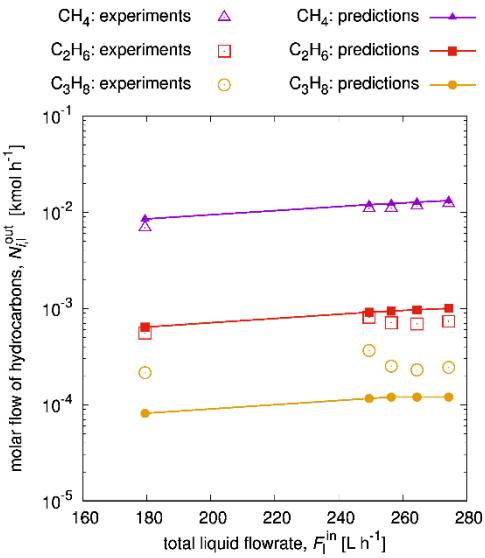

Figure 4.12: Predicted light hydrocarbon molar flowrates in flashed gas against experimental data from pilot plant for different solvent flowrates. The gas inlet flowrate, CO_2 inlet content and solvent inlet CO_2 loading were, respectively 75 kg h^{-1}, 5 mol% and 0.01 mol mol^{-1}.

4.4.2.3 Estimation of solvent evaporation rate in high-pressure MBC for NG sweetening.

The model predicts that water is predominantly evaporated while the evaporation rates of MDEA and PZ to the treated gas are negligible (left plot in Figure 4.13). This is attributed to the vapor pressures of MDEA and PZ being much lower compared to that of water in the temperature of 293-353 K (right plot in Figure 4.13) as well as their concentrations.

The low solvent evaporation rate is due to the fact that at higher operating pressure (54 bar), the molar fraction $y_{i,g}^{out}$ of solvent in the treated gas outlet, is 50 times smaller compared to atmospheric pressure (Eq. 4.3). For an MBC operating at atmospheric pressure, such as in post-combustion CO_2 capture, one can expect much higher solvent evaporation losses, hence the need to model solvent evaporation in a more detailed manner. For a high-pressure MBC used in NG sweetening, the assumptions of using Raoult's Law (Sec. 4.2.3) by means of overall mass balance (lumped) are justified since the evaporation rate is low.

2. Stream flowrates

Variable	Value at time 0.00000	Units
Mass flowrate	0.0181556	kg/s
Molar flowrate	3.65714	kmol/h
Volumetric flowrate	Data not available.	m^3/s
Component mass flowrate("H2O")	1.69693E-05	kg/s
Component mass flowrate("MDEA")	5.26213E-09	kg/s
Component mass flowrate("PZ")	2.30352E-07	kg/s
Component mass flowrate("CO2")	4.33188E-05	kg/s
Component mass flowrate("methane")	0.0146604	kg/s
Component mass flowrate("ethane")	0.00209891	kg/s
Component mass flowrate("propane")	0.00133579	kg/s
Component molar flowrate("H2O")	0.00339104	kmol/h
Component molar flowrate("MDEA")	1.58977E-07	kmol/h
Component molar flowrate("PZ")	9.62743E-06	kmol/h
Component molar flowrate("CO2")	0.00354346	kmol/h
Component molar flowrate("methane")	3.28985	kmol/h
Component molar flowrate("ethane")	0.251291	kmol/h
Component molar flowrate("propane")	0.109055	kmol/h

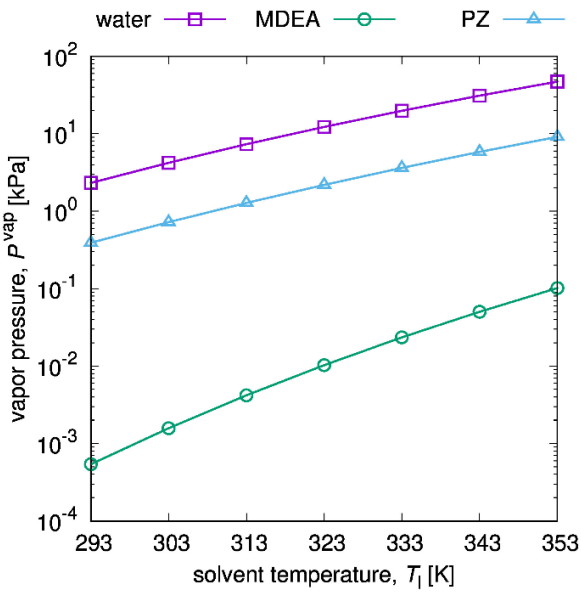

Figure 4.13 Left: Predicted component flowrates of the treated gas from MBC for a CO_2 loading, gas and solvent flowrates of 0.01 mol mol^{-1}, 75 kg h^{-1} and 275 L h^{-1}, respectively; **Right:** Vapour pressure of water, MDEA, and PZ between 293 - 353 K.

The model predicts that about 0.03 wt% of the solvent flowrate fed to the MBC is lost by evaporation in the pilot plant. The corresponding energy consumed by this solvent evaporation

in the MBC is less than 1 % of the heat generated by the CO_2 absorption. This confirms that solvent evaporation has a minimal impact on the solvent temperature at high pressure and validates the approximation of accounting for solvent evaporation at the liquid inlet in the MBC energy balance (see Sec. 4.2.4). Overall, the ability to predict the solvent evaporation rate and its composition will enable quantifying the amount of solvent make-up required and will feed into the process-wide assessment of MBC for NG sweetening in Chapter 5.

4.5 Conclusions

This chapter has refined the MBC model by including a description of solvent losses from evaporation and hydrocarbon absorption into the amine solvent, for lean and semi-lean operating conditions. An energy balance has also been added to the model, which enables predicting the temperature profile in the MBC by accounting for the CO_2 absorption heat of reaction and heat losses from solvent evaporation. An experimental verification of the model has been conducted using both lab-scale and pilot-scale MBC modules, using a new membrane fiber compared to Chapter 3 which significantly increases the specific membrane area. A close agreement of the model predictions with measured CO_2 absorption fluxes has been observed at various CO_2 loadings in solvent, various gas and liquid flowrates, and various CO_2 inlet concentration.

The predicted molar flowrates of light hydrocarbons against the measured flowrates in the flashed gas from the rich amine drum verified the assumption that the solvent is about saturated with hydrocarbons at the MBC outlet. Therefore, this prediction can help to determine the amount of HC that can be recovered in the downstream flash drum to minimize product loss in a process-wide plant. The model also predicts that water is predominantly evaporated, while the MDEA and PZ evaporation rates to the treated gas are negligible due to the vapor pressure of MDEA and PZ being much lower compared to water in the temperature range of interest. Only a small amount of solvent is evaporated compared to the total solvent flowrate in the pilot-scale MBC, and therefore solvent evaporation has a minimal impact on the solvent outlet temperature. This prediction was confirmed by the close agreement between predicted and measured temperature profile in the lab-scale MBC. Overall, the ability to predict the solvent evaporation rate and its composition will enable quantifying the amount of solvent make-up required in a full-scale MBC process.

Moving forward, the MBC model (*i.e,.* absorption section) can now be integrated with the solvent regeneration unit (*i.e.,* desorption section) for the development of a full-scale MBC based NG sweetening process model in Chapter 5. This integration will make it possible to analyze the effects of different conceptual designs, including various absorption/desorption design configurations and operational decisions for process scale-up and process-wide economic assessment.

Chapter 5 Process-wide modeling and assessment of natural gas sweetening using high-pressure membrane contactors

5.1 Introduction

Through Chapters 3 and 4, a mathematical model of high-pressure MBC has been formulated and verified experimentally, which is capable of quantitative predictions of both CO_2 and hydrocarbon absorptions in the amine solvent and solvent evaporation losses to the treated gas. The main objective of this chapter is an integration of this MBC model into a complete process model describing both CO_2 absorption and desorption operations, and then conducting a model-based assessment of a full-scale MBC process for NG sweetening.

Most modeling studies in the literature focus on the mathematical modelling of a standalone MBC for CO_2 capture operating at or near atmospheric pressure (Al-Marzouqi et al. 2008; Rezakazemi et al. 2011; Hoff and Svendsen 2014) or at high pressure (Faiz and Al-Marzouqi 2010; Quek et al. 2018). Even though the effectiveness of MBC for CO_2 removal has been widely studied over the past few decades, a detailed assessment of this technology in an industrially relevant context, and in particular for NG sweetening, is still lacking.

The absorption column in a conventional NG sweetening process can be readily replaced by an MBC unit, as depicted in Figure 5.1. This process comprises two operations — absorption and desorption (a.k.a solvent regeneration). In the absorption process, the (lean or semi-lean) chemical solvent, most commonly alkanolamines, flows counter-currently with the gas in the MBC, and selectively reacts with the acid gasses (CO_2 and H_2S) from the gas phase. For bulk CO_2 removal, the CO_2 purity target is typically sales gas specification with a CO_2 content lower than 2 mol% (TransCanada, 2016) or 6-8 mol% when the CO_2 content at the feed gas is higher than 20 mol%. For deep CO_2 removal applications in liquefied natural gas (LNG) plants and ammonia plants, the CO_2 specifications are <50 ppmv and < 100 ppmv, respectively, to avoid freezing in low-temperature chillers (liquefaction process) and catalyst poisoning (Boucif et al., 2012; Hoff, 2003).

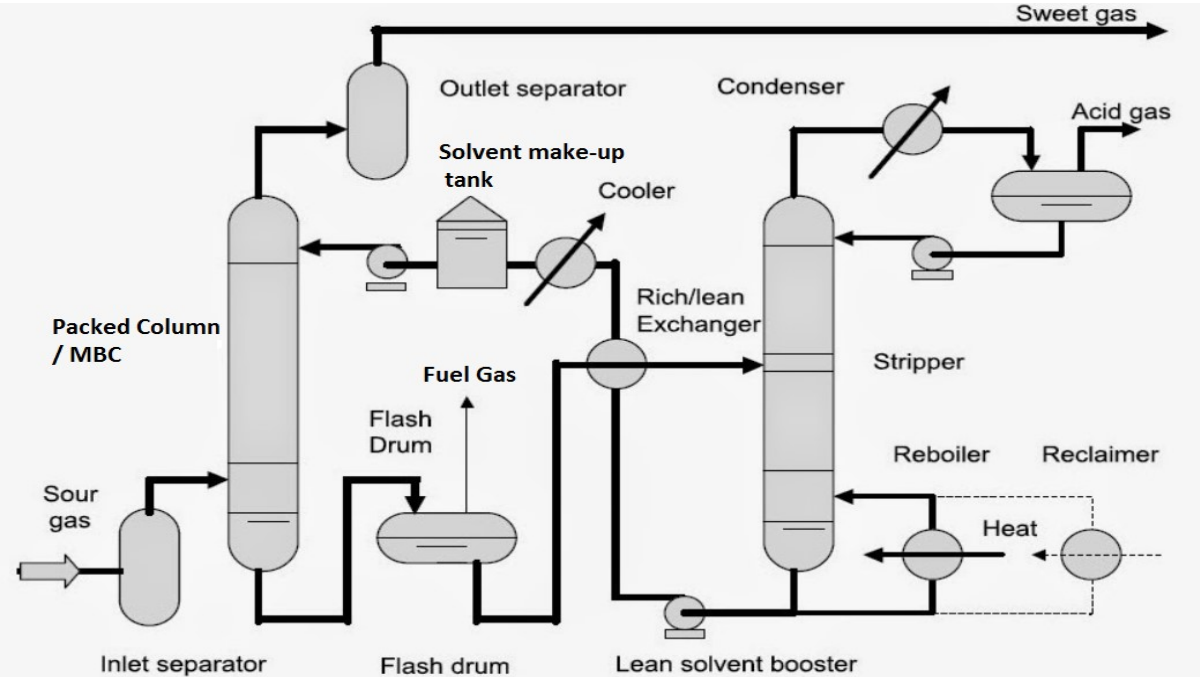

Figure 5.1: Simplified absorption/desorption cycle showing how MBC may replace the packed column. Adapted from: Gas Processors Suppliers Association (2004).

The terms lean and semi-lean refer to the fraction of acid gasses present in the amine solvent. In the context of CO_2 capture, "lean" solvent refers to an inlet solvent stream containing little or no CO_2 (*i.e.,* CO_2 loading ca. 0.01 mol mol^{-1}), while "semi-lean" indicates that the amine contains some CO_2 (*i.e.,* CO_2 loading ca. 0.2 mol mol^{-1}). The solvent stream coming out of the MBC is termed "rich", and it needs to undergo regeneration, which consists of a combination of flash stages and a gas-liquid contacting column.

In Figure 5.1, the rich amine solvent from the MBC outlet is first directed to a lower pressure flash drum to recover the flashed HC as fuel gas. The liquid outlet stream from the flash drum is then fed to the regeneration column, where it is heated by the reboiler to a suitable temperature to strip off CO_2 from the rich solvent before recycling the lean solvent to the MBC unit. On the other hand, the overhead condenser provides a reflux liquid stream to the column to ensure that the top-product stream (a.k.a acid gas stream) is as pure as possible. Finally, solvent make-up feeds into the amine tank to replenish the solvent evaporated in the MBC, flash drum, and regeneration column. The solvent regeneration process is operated at low pressure to recover the light HC and to lower the solvent boiling point in order to reduce energy consumption. A lower boiling point is also advantageous to keep the solvent below its

degradation temperature. Typically, the reboiler of the solvent regeneration process is the largest contributor to the operating cost (MacDowell et al., 2010; Cormos et al., 2015).

Some key performance indicators (KPIs) for the NG sweetening process are: (a) the CO_2 purity in the product gas; (b) the energy per ton CO_2 removed; (c) the amount of HC loss or recovered as fuel gas; and (d) the amount of solvent loss per treated gas and makeup required. Pakšiová et al. (2016) modeled a simple MBC operating at atmospheric pressure for both the absorption and desorption of CO_2, assuming non-wetted operation. Their model described the counter-current flow of CO_2/CH_4 gas mixture and MEA as absorbent and was used to simulate the effects of different liquid and gaseous flow rates on the process performance. To the best of knowledge, there is no published literature on MBC integrated within a NG sweetening process, that would consider the KPIs (a) – (d) all together.

A key contribution of this chapter is the development of an MBC-based NG sweetening process, which integrates the MBC model (absorption section) from Chapters 3 and 4 with the model of a conventional solvent regenerator (desorption section). The main objective is to use this integrated model to predict the CO_2 removal performance and the energy duty for each equipment under various scenarios, including lean and semi-lean process operation. The amount and the composition of light hydrocarbons (HC) recovered in the flash drum at various pressures can be quantified. In addition, the evaporative solvent losses in the MBC and solvent regeneration sections can be predicted, so that the solvent makeup required to maintain the solvent concentration in the process can be quantified and costed. Similar to previous chapters, the predictive capability of the integrated model in terms of CO_2 removal performance and energy consumptions will be tested against data from a pilot-scale MBC module operated at variable CO_2 loading in the amine solvent, at a NG processing plant in Malaysia. All of the experiments were conducted with aqueous mixtures of MDEA and piperazine (PZ) as the chemical solvent.

The rest of this chapter is organized as follows. The experimental set-ups of the pilot-scale MBC based NG sweetening process, and the corresponding model parameters are presented in Sec. 5.2, followed by a description of the development and implementation of the MBC process-wide model in Sec. 5.3. Results of the experimental verification of the process-wide model are presented and discussed in Sec. 5.4. Then, a model-based analysis is conducted in Sec. 5.5, to investigate the effect of (i) optimized lean and semi-lean MBC operations on energy

duty, (ii) different operating pressures on HC recovery in the rich solution flash drum, and (iii) different inlet solvent temperatures on the evaporative solvent losses. A model-based design and scale-up of a commercial-scale MBC is conducted in Sec. 5.6 for a semi-lean MBC process operating under industrially relevant conditions for NG sweetening and its intensification potential is assessed. Finally, Sec. 5.7 concludes the chapter.

5.2 Material and Methods

5.2.1 Pilot-Scale MBC Setup

Experiments were conducted in pilot-scale module operated under industrially relevant operating conditions at 54 bar in a NG processing plant in Malaysia. Aqueous mixtures of methyl diethanolamine (MDEA) and piperazine (PZ) were used as the chemical solvent. This experimental setup is identical to the pilot-scale description in Sec. 4.3.1 (see also Sec. 3.3.1), and is depicted in Figure 4.4. The corresponding operating conditions for the absorption and desorption system are summarized in Table 5.1. The flows and compositions of the gas at the MBC inlet and outlet, of the regenerated solvent, and of the flash gas were measured and averaged hourly for comparison with model predictions. The energy consumption of all the units which was powered by electricity was monitored. The piece of equipment considered for the total energy consumption or known as process duty, P_{T} [kW] are the (i) reboiler, (ii) overhead condenser, (iii) reflux pump, (iv) LP amine pump (v) lean solution cooler (vi) HP amine pump, and (vii) amine chiller.

5.2.2 Module Specification

The high-pressure MBC module was packed with hydrophobic, Polytetrafluoroethylene (PTFE) hollow fiber, which is identical to the module used in Chapter 4 (see Sec. 4.3.2, Table 4.3). The solvent regenerator was packed with Raschig Super-Ring #1 material. Table 5.2 summarizes the main characteristics and geometrical properties of both the MBC and solvent regeneration units.

Table 5.1: Operating conditions in the pilot plant.

Parameters	Natural Gas
MBC (Absorption)	
CO_2 inlet, $y^{in}_{CO_2,g}$ [mol%]	5
CH_4, C_2H_6, C_3H_8 inlet, [mol%]	85 / 7 / 3
MDEA/PZ inlet, [wt%]	39/5
Inlet gas pressure, P^{in}_{g} [kPa]	5400
Outlet liquid pressure, P^{out}_{l} [kPa]	5430
Gas mass flowrate, M^{in}_{g} $[\text{kg h}^{-1}]$	75
Liquid volumetric flowrate, F^{in}_{l} $[\text{L h}^{-1}]$	275
Gas temperature, T^{in}_{g} [K]	301-308
Liquid temperature, T^{in}_{l} [K]	308-313
CO_2 loading in solvent, $f^{in}_{CO_2,l}$ $[\text{mol mol}^{-1}]$	0.01-0.24
Solvent Regeneration (Desorption)	
Rich solution drum pressure, [kPa]	911
Solvent regenerator pressure, [kPa]	258
Reboiler temperature, [K]	403
Overhead condenser – Outlet [K]	333
Reflux pump pressure – Outlet [kPa]	258
Lean-rich exchanger	
Cold stream – Inlet / Outlet [K] / [kPa]	352 / 371 / 368
Hot stream – Inlet / Outlet [K] / [kPa]	382 / 364 / 233
LP amine pump pressure – Outlet [kPa]	711
Lean solution cooler – Outlet [K]	318
– Pressure drop [kPa]	35
Amine HP pump pressure – Outlet [kPa]	5460
Amine chiller – Outlet, [K]	308
– Pressure drop [kPa]	30

Table 5.2: Specifications of the MBC and solvent regeneration units.

Parameter	Value	Source
MBC (Absorption)		
Fiber length, L [m]	2.3	(PRSB, 2016)
Fiber inner radius, r_1 [μm]	225	(PRSB, 2016)
Fiber outer radius, r_2 [μm]	550	(PRSB, 2016)
Membrane porosity, ε [$-$]	0.41	(PRSB, 2016)
Membrane tortuosity, τ [$-$]	6.1	Sec. 4.3.2
Max. pore radius, δ_{max} [μm]	0.18	(PRSB, 2016)
Mean pore radius, $\bar{\delta}$ [μm]	0.06	Sec. 4.3.2
Pore standard deviation, σ [$-$]	0.24	Sec. 4.3.2
Contact angle , θ [°]	92.4	(PRSB, 2016)
Packing density, $\emptyset$ [$-$]	0.38	Sec. 4.3.3
Module inner radius, R_m [m]	0.115	(PRSB, 2016)
Membrane area, A_m [m^2]	68	Sec. 4.3.3
No of fibers, N [$-$]	8400	(PRSB, 2016)
Specific surface area [m^{-1}]	1600	(PRSB, 2016)
Outer radius of steel tube, R_t [m]	0.08	Sec. 4.3.3
Conventional Solvent Regenerator (Desorption)		
Packing size, [m]	0.025	(Honeywell UOP, 2014)
Packing height / diameter, [m]	6.1/0.3	(Honeywell UOP, 2014)
Surface area, [m^2/m^3]	150	(Honeywell UOP, 2014)
Void fraction, [$-$]	0.98	(Honeywell UOP, 2014)
Loading point constant, C_s [$-$]	3.491	(Billet and Schultes, 1999)
Flooding point constant, C_{FL} [$-$]	2.2	(Billet and Schultes, 1999)
Hydraulic constant, C_h [$-$]	0.75	(Billet and Schultes, 1999)
Total particles constant, C_{P0} [$-$]	0.5	(Billet and Schultes, 1999)
Liquid constant, C_L [$-$]	1.29	(Billet and Schultes, 1999)
Vapor constant, C_v [$-$]	0.44	(Billet and Schultes, 1999)

5.3 Modeling of MBC-based process for NG sweetening

This section describes the modeling of the regeneration unit operations in the MBC process, namely the flash drum, heat exchangers, pumps, and stripping column based on the MBC pilot-plant set up as described in Sec. 3.3.1. Their integration with the MBC unit model developed in Chapter 3 and 4 was conducted in the gPROMS ProcessBuilder environment. The MBC model was compiled into a gML-compliant model library, with the user interface shown in Figure 5.2. This library was then integrated to ProcessBuilder's standard unit operation library in order to build the MBC process flowsheet that is shown in Figure 5.3. The following subsections provide an overview of the specifications in the regeneration unit operations (see Table 5.1) as well as some numerical solution details.

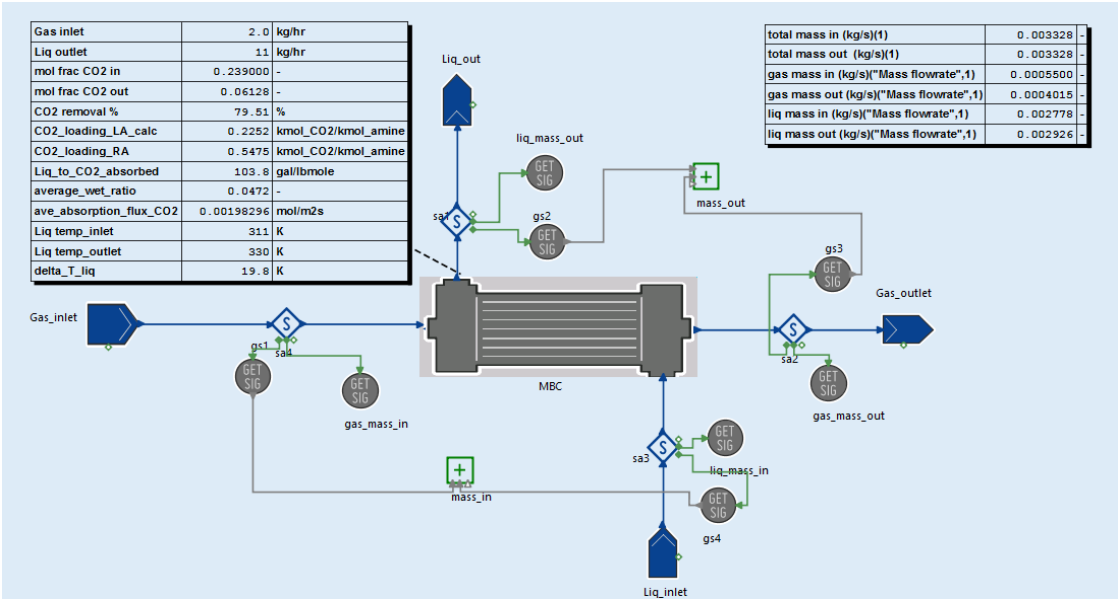

Figure 5.2: gML-compliant MBC unit operation model in gPROMS ProcessBuilder.

5.3.1 Modeling of rich solution flash drum

The rich amine from the MBC shell outlet passes through a pressure expander before entering the rich solution drum. The outlet pressure of the expander is set to the rich solution flash drum pressure of 911 kPa (Table 5.1). The rich solution drum itself is modelled as a two-phase (liquid-vapor) flash vessel, described by mass and energy balances, and thermodynamic equilibria (PSE, 2018), which predicts the flowrates, compositions, temperatures and pressures of the liquid and vapor outlet streams from the rich solution drum. And the presence of multiple liquid phase is accounted for in the model.

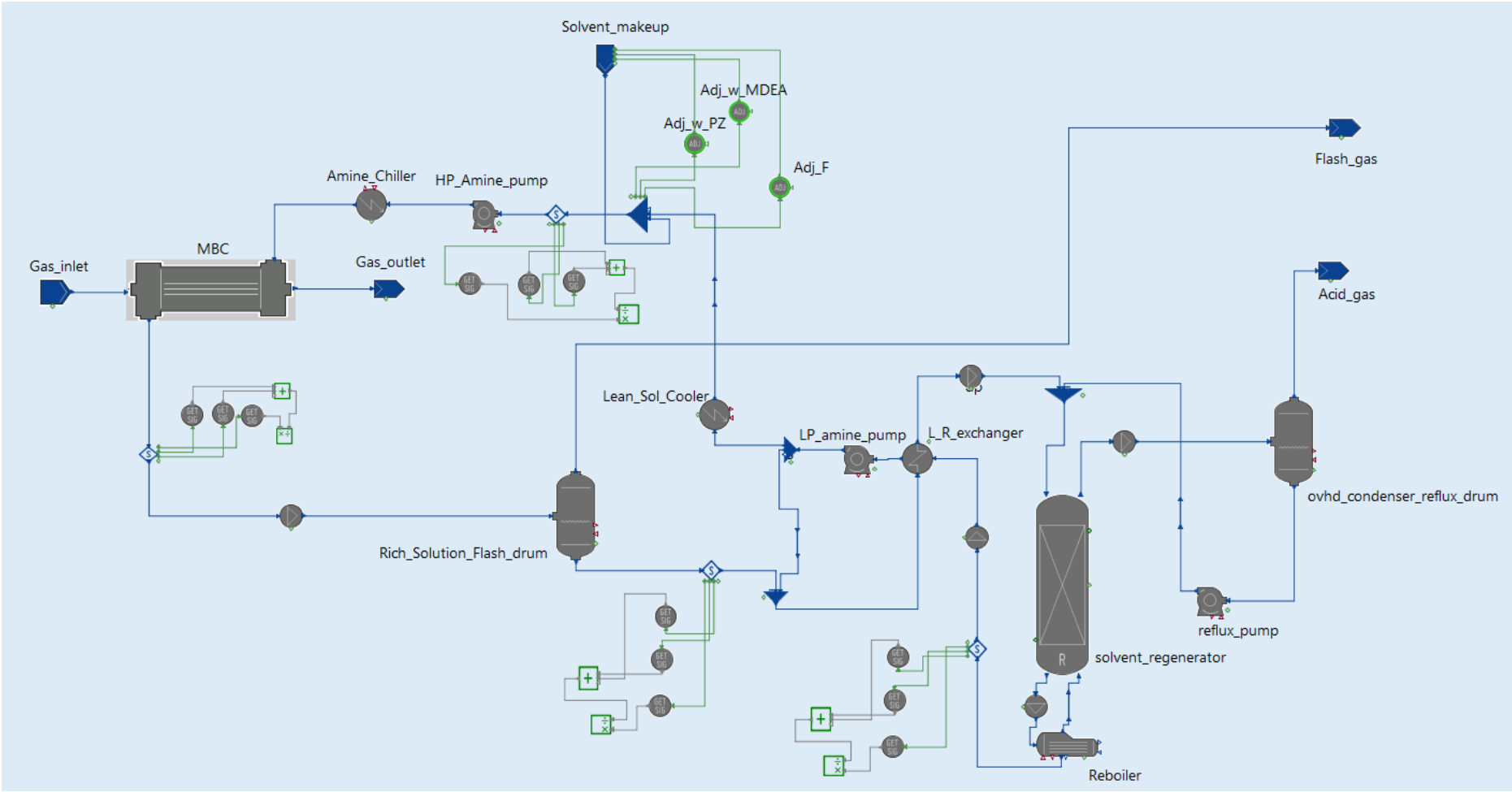

Figure 5.3: MBC based NG sweetening process flowsheet in gPROMS ProcessBuilder

5.3.2 Modeling of heat exchangers

Heat exchangers in the process model include a lean-rich heat exchanger, lean solution cooler, amine chiller, overhead condenser, and reboiler. The lean-rich heat exchanger, which transfers heat from the regenerated amine (hot stream) to the rich amine (cold stream), is modeled as a counter current flow heat exchanger. The cold stream outlet temperature and pressures of both outlet streams are specified in Table 5.1. The lean solution cooler and amine chiller, which reduce the amine temperature to 318 K and 303 K, respectively (Table 5.1) after its regeneration, are modelled with standard cooler The overhead condenser and reflux drum are modeled as a standard separator, with outlet temperature set to 333 K, in order for the fluid to separate into two phases. The reboiler is described by an evaporator kettle model, where the thermal specification is set at 403 K (Table 5.1). The heat exchanger models predict the process duty required to meet the thermal specifications.

5.3.3 Modeling of pumps

Pumps in the process model include the amine HP pump, amine LP pump, and the reflux pump. All of these pumps are assumed to have mechanical and isentropic efficiencies of 85%. The fluid outlet temperatures are furthermore calculated by defining the fluid compression relative to an ideal compression process, using an ideal efficiency (PSE, 2018). The outlet pressures for the pumps are specified as per Table 5.1. The pump models predict the required process duty required based on the outlet pressure specifications and efficiencies.

5.3.4 Modeling of the solvent regeneration column

For the solvent regenerator, the rate-based model from gPROMS's Advanced Model Library (PSE, 2018) for Gas-Liquid Contactor (AML: GLC) is used. The exchange of mass and heat between the bulk gas and liquid phases is described via gas and liquid films, separated by an infinitesimally thin interface where the phases are at equilibrium.

The Raschig Super Ring #1 packing characteristics (Table 5.2) are used by the model. The built-in correlations in AML: GLC are used to calculate the performance of packing. Specifically, the Onda correlations for mass transfer with random packing are used to predict the mass transfer coefficients and the interfacial area; and the Billet holdup correlation is used

to calculate the liquid holdup in the regenerator. It should be noted that the pressure drop in the column is neglected here.

The solvent regenerator model is coupled with the reboiler and condenser, which were described in Sec 5.3.2. The complete column model predicts the flow rate, composition temperature and pressure of the outlet gas and lean solvent streams.

5.3.5 Modeling of the solvent make-up

The solvent make-up stream maintains the desired solvent flowrate and concentration in the MBC system. In gPROMS ProcessBuilder, three "Adjust" elements are used to set the solvent flowrate to MBC, MDEA mass fraction and PZ mass fraction to 275 L h^{-1}, 39 wt% and 5 wt%, respectively (Table 5.1). These three elements feed into a mixer immediately before the MBC unit.

5.3.6 Thermo-Physical, Transport, and Reaction Kinetic Data

Temperature-dependent expressions for the macroscopic reaction rates of CO_2 with MDEA and PZ, and the diffusivity coefficients of the various species in the gas and liquid mixtures used in the MBC model are reported in Appendix A, while Henry's constants for CO_2 in the amine solution was taken as in Sect 4.3.4.2. In order to reduce the computational burden, simple polynomial surrogates are derived in the temperature range of 300-400 K for the diffusivity coefficient $D_{\mathrm{CO_2,l}}$, $D_{\mathrm{MDEA,l}}$ and $D_{\mathrm{PZ,l}}$ (Eqs. A.6 – A.11).

Other thermo-physical and transport parameters were obtained by interfacing gPROMS with the property packages Advanced Peng Robinson, UNIQUAC-RK and RSKA for the gas and liquid phases in the absorption and regeneration unit from Multiflash v6.1, respectively.

5.3.7 Numerical Simulation

As previously described in Chapters 3 and 4, a second-order centered finite difference scheme was used to discretize the partial differential equations of the MBC model, after a rescaling of the radial dimension for the membrane dry and wet spatial subdomains to be rectangular as outlined in Appendix B (Table B.1). A coarser uniform mesh grid consisting of 35 elements

was chosen to perform the simulations herein, which provides solutions within <1% of finer discretizations, while reducing the computational burden. For the solvent regenerator, a first-order finite difference method for the bulk liquid and vapor consisting of 20 elements was used. With these discretizations, a steady-state simulation takes about 10 minutes to converge on a desktop computer running Windows 7 with Intel® CoreTM i7-4790 CPU at 3.60GHz and 32GB of RAM in gPROMS ProcessBuilder v1.3.1.

5.4 Experimental Model Verification

A comparison of the predicted CO_2 removal performance of the MBC, CO_2 loadings in amine and total process duty against measurements from the pilot plant are presented in Figure 5.4. The experimental data are for different CO_2 loadings in the solvent, at constant gas and liquid flowrates of 75 kg h^{-1} and 275 L h^{-1}, respectively. Overall, the predictions are found to be in good agreement with the measurements, showing errors lower than 5% for the CO_2 absorption fluxes, CO_2 removal efficiencies, CO_2 loadings and total process duty. Notice that an error of ca. 15% can be seen in the second experiment point in Figure 5.4 (left axis) when compared against the predicted CO_2 outlet purity. The low level of CO_2 outlet purity (0.73 mol%) is susceptible to large error even there is a small variation in the predicted CO_2 outlet purity (0.85 mol%). Nevertheless, when compared in terms of CO_2 absorption flux and removal efficiency, the predictions and measurement is found to be within 5%.

The MBC model correctly predicts that a larger CO_2 liquid loading will reduce the CO_2 removal efficiencies, which in turn will decrease the CO_2 outlet purity (Figure 5.4A). As discussed in Chapter 4 previously, an increase in the liquid CO_2 loading leads to a decrease in the CO_2 solubility and absorption capacity of solvent due to a reduction in free amine. The process-wide model also correctly predicts the reduction in heating and cooling duties with a higher CO_2 loading in the solvent (Figure 5.4B). In particular, the reboiler of the regeneration column can be operated at a lower temperature under semi-lean operation (Figure 5.4D), which reduces the energy needed for the solvent regeneration. Alie (2004) and Xu et al. (2016) also found that the reboiler duty is significantly reduced by increasing the solvent CO_2 loading up to 0.23 and 0.27 mol mol^{-1}, respectively. Notice that the increase in regeneration temperature decreases the CO_2 inlet loading (Figure 5.4D) to the MBC, which in turn improves the CO_2 absorption flux (Figure 5.4C). Also, notice that the difference between the inlet and outlet CO_2 loading is larger

for lean amine condition ($f^{in}_{CO_2,l}$ = 0.01) compared to semi-lean operation ($f^{in}_{CO_2,l}$ = 0.23) as the CO_2 removal efficiency (ca. 99.9%) is higher compared to semi-lean operation (ca. 80%) as depicted in Figure 5.4D and 5.4A.

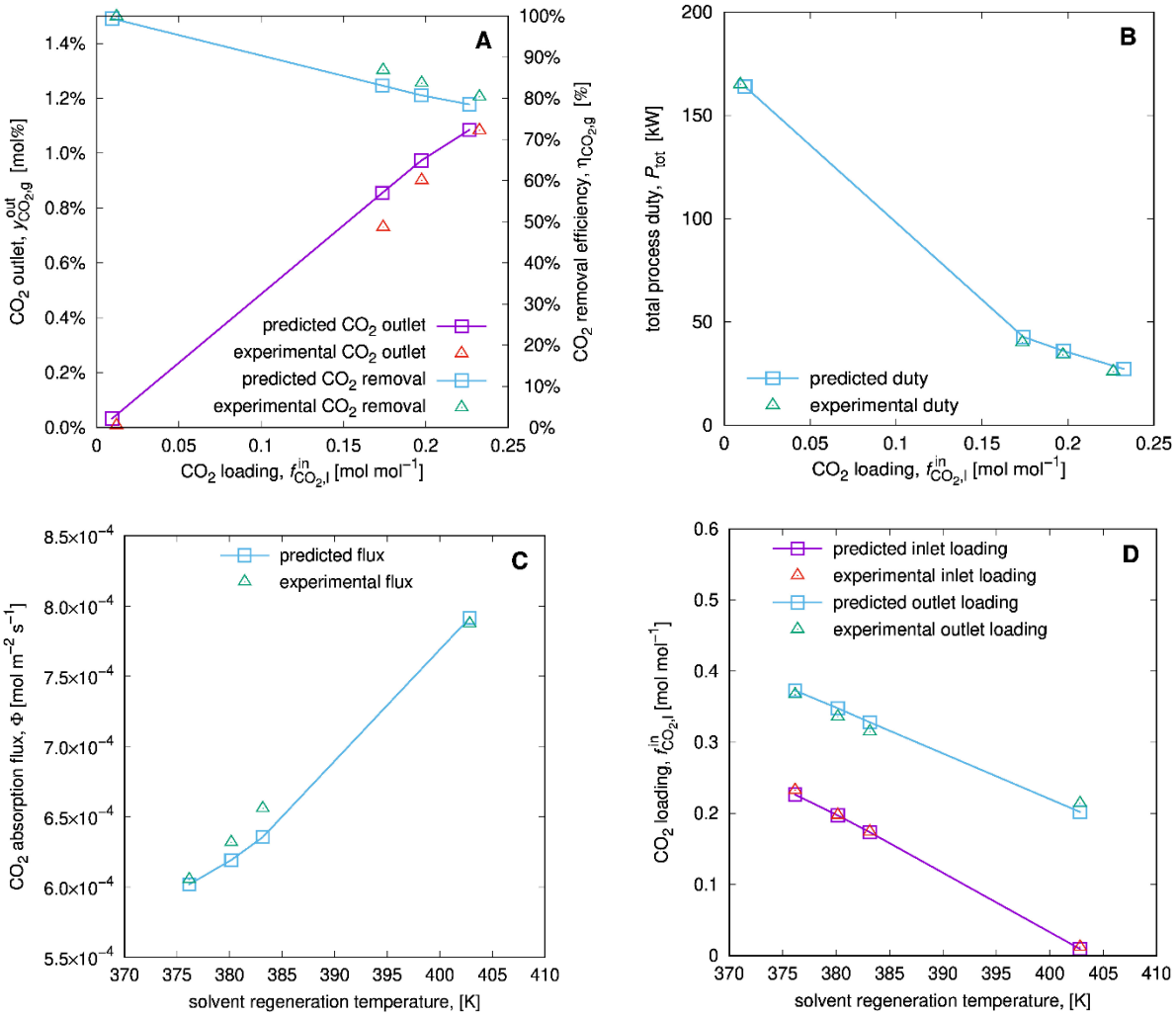

Figure 5.4: Predicted CO_2 removal performance of the MBC, CO_2 loadings in amine and total process duty against experimental measurements at constant gas and solvent flowrates of 75 kg h^{-1} and 275 L h^{-1}, respectively **A:** Predicted CO_2 purity at the MBC gas outlet and CO_2 removal efficiencies at various CO_2 loadings in the solvent; **B:** Predicted total process duty at various CO_2 loadings in the solvent; **C:** Predicted CO_2 absorption fluxes at various solvent regeneration temperatures; **D:** Predicted CO_2 loadings at various solvent regeneration temperatures.

In order to achieve deep CO_2 removal, for example to meet the LNG specification of < 50 ppmv of CO_2, the process model indicates that a lean solvent is necessary (CO_2 loading ≈ 0.01 mol mol^{-1}). On the other hand, a semi-lean solvent (CO_2 loading ca. 0.23 mol mol^{-1}) operation

appears to be sufficient to meet the typical sales gas specification of <1.5 mol% CO_2. In this particular experiment, the semi-lean operation consumes ca. 80% less energy compared to lean operation. Further model-based analysis and design of NG sweetening using an MBC process are conducted in the following sections.

5.5 Model-Based Analysis of pilot-scale MBC

In this section, the process-wide model was developed for the MBC pilot plant in order to analyse: (i) the process duty for an optimized MBC lean and semi-lean amine process; (ii) the optimum pressure at the rich solution flash drum for maximum fuel gas recovery; and (iii) the amount and concentration of solvent make-up.

5.5.1 Optimal solvent flowrate for lean and semi-lean operations

The experimental model verification in Sec. 5.4 has shown that both lean and semi-lean operations are capable of CO_2 purities down to the sales gas specification of <1.5 mol%, with the semi-lean operation consuming 80% less energy compared to lean operation. However, these experiments were all conducted with same flowrate of solvent to the MBC and may therefore correspond to a suboptimal operation. Herein, the minimum liquid flowrate required is determined to achieve a CO_2 purity of 1.5 mol% for processing 75 kg h^{-1} of sour natural gas. The lean amine operation is similar to the flowsheet in Figure 5.3, now without the excess amine recycle back to the solvent regenerator. Notice that the dimension of the solvent regenerator remains the same in the pilot plant in order to provide a conservative reboiler process duty when compared with the semi-lean process. For the semi-lean process, the reboiler and solvent regeneration column are replaced with a heater and a low pressure flash drum, as shown in Figure 5.5. All of the pressure and temperature specifications in both flowsheets remain the same as given in Sec. 5.2 and 5.3, except the reboiler/heater temperature, which is adjusted to obtain the desired CO_2 loading in the solvent. The results of this comparison are reported in Table 5.3.

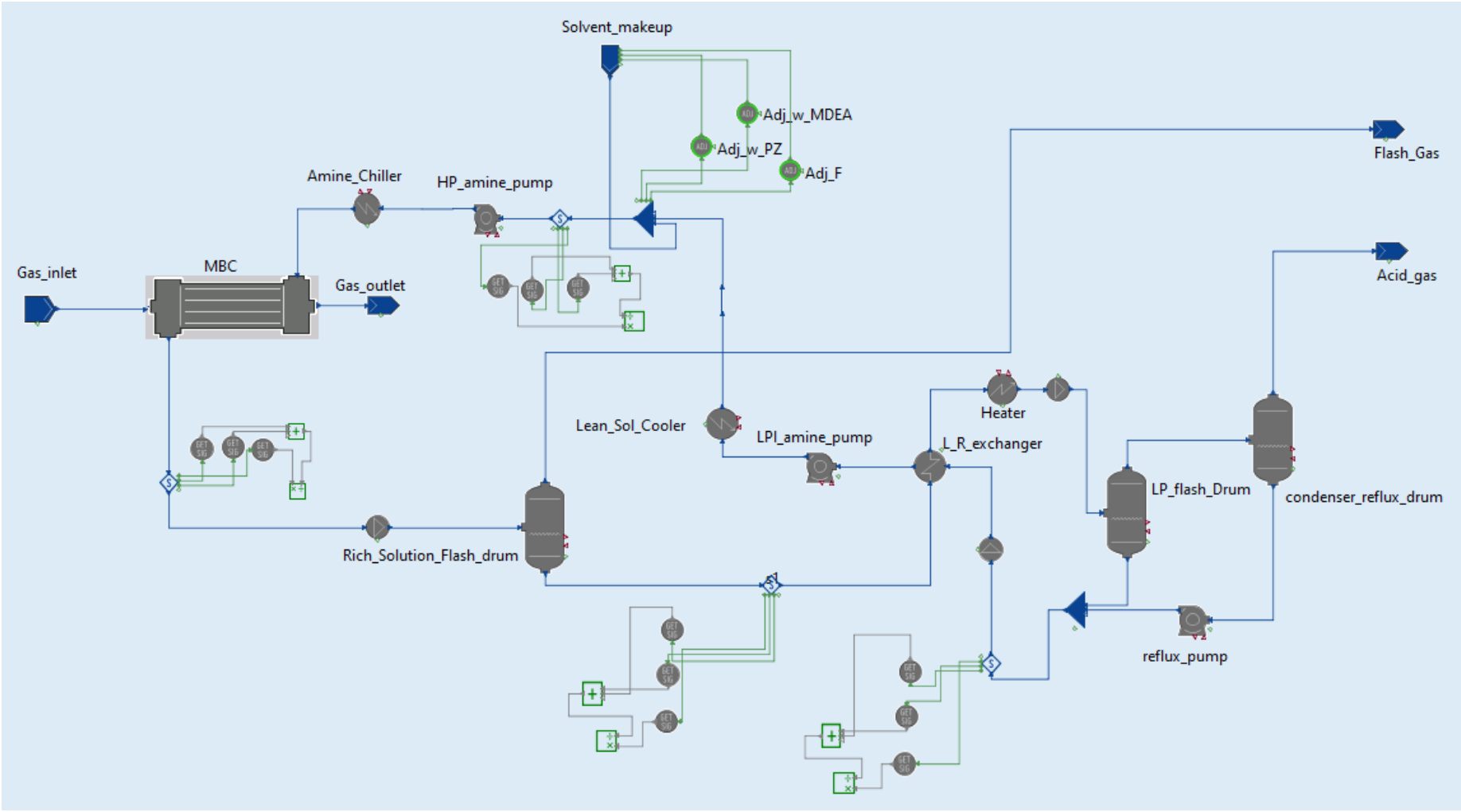

Figure 5.5: Model-based analysis - MBC pilot scale semi-lean operation in gPROMS ProcessBuilder.

The optimized lean operation requires a 34% lower solvent flowrate to the MBC compared to the optimized semi-lean operation to meet the required CO_2 purity. This is due to a higher CO_2 absorption capacity of the lean solvent, which enhances the CO_2 removal rate in the MBC. With a lower solvent flowrate, the model predicts a decrease in the process duties of all the pumps in comparison to the semi-lean operation. This corresponds to L/G ratio of ca. 0.75 m^3 $kmol^{-1}$, which is at the lower end values of 0.6 – 1.1 m^3 $kmol^{-1}$ typically encountered in conventional packed column (Park et al., 2004; Rezazadeh et al., 2016; Gaspar et al., 2017).

Table 5.3: Optimized operating conditions and process duty of the lean and semi-lean MBC

Parameters	Lean Operation	Semi Lean Operation
MBC (Absorption)		
CO_2 inlet, $y^{in}_{CO_2,g}$ [mol%]	5	5
MDEA/PZ inlet, [wt%]	39/5	39/5
Inlet gas pressure, P^{in}_{g} [kPa]	5400	5400
Outlet liquid pressure, P^{out}_{l} [kPa]	5430	5430
Gas mass flowrate, M^{in}_{g} $[kg\ h^{-1}]$	75	75
Liquid volumetric flowrate, F^{in}_{l} $[L\ h^{-1}]$	109	146
Gas temperature, T^{in}_{g} [K]	297	297
Liquid temperature, T^{in}_{l} [K]	303	303
CO_2 loading in the solvent, $f^{in}_{CO_2,l}$ $[mol\ mol^{-1}]$	0.01	0.24
Solvent Regeneration (Desorption)		
Reboiler/Heater temperature, [K]	403	376
Reboiler duty, [kW]	6.92	4.41
Overhead condenser duty, [kW]	0.51	1.41
Reflux Pump duty, [kW]	5.10E-5	1.45E-4
Lean solution pump duty, [kW]	0.0173	0.022
HP amine pump duty, [kW]	0.181	0.24
Lean solution cooler duty, [kW]	4.8	2.87
Amine chiller duty, [kW]	1.35	1.8
Total process duty, [kW]	13.7	10.7

However, the total process duty remains 28% higher under lean operation compared to semi-lean operation, due to the higher reboiler temperature that is required to regenerate the solvent under lean operation. And a higher temperature of the regenerated solvent also requires a higher cooling duty in the lean solution cooler too, before returning the solvent to the MBC, despite the heat integration between the inlet and outlet streams to the regenerator.

Figure 5.6 shows the breakdown of total process duty in terms of the different pieces of equipment under both lean and semi-lean operations. The reboiler duty is the largest energy consumer with approximately 40-50% of the overall process duty for both operations, which is consistent with the findings by MacDowell et al. (2010) and Cormos et al. (2015). The lean solution cooler and amine chiller come second and third, respectively, with 26-35% and 9-17% of the total process duty. Based on this analysis, one area of improvement could be to operate the liquid above 318 K at the MBC absorption section. This operation would eliminate the requirement of an amine chiller, therefore potentially reducing the footprint and process duty by a further 9-17% in both operations (see Sec. 5.6).

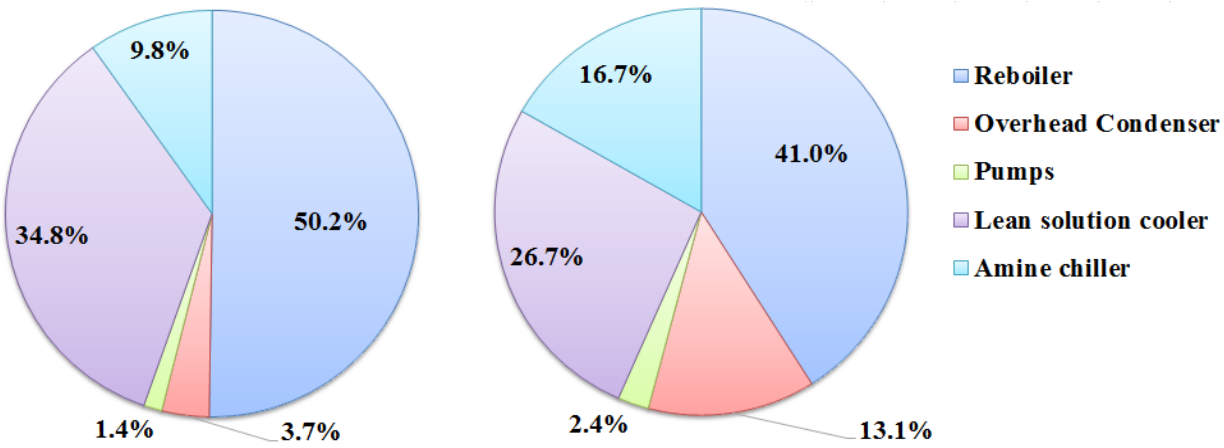

Figure 5.6: Breakdown (%) of the equipment process duty. Left: MBC lean amine operation. Right: MBC semi-lean amine operation.

Overall, the semi-lean operation presents a higher intensification potential with the reduction in energy consumption and footprint (i.e., flash tank and heater), and this should translate into a reduction in capital and operating expenditure compared to the lean operation.

5.5.2 Optimal flash pressure for fuel gas recovery

Any HC absorbed in the solvent and that is not recovered will end up in the acid gas stream. This could represent a large product loss and may cause problems elsewhere in the process (Carroll et al., 1998). This subsection investigates the optimum pressure at which to operate the rich solution flash drum for maximal flash gas recovery. A key constraint in practice is that the recovered flash gas should have a high enough lower heating value (LHV) in order to meet fuel gas specification, *i.e.,* 47.1 MJ kg^{-1} (ToolBox, 2003; Hydrogen Tools, 2019). From a thermodynamic standpoint, operating the rich solution flash drum at a lower pressure will increase the amount of flash gas, hence increasing fuel gas recovery. However, those species with a lower vapor pressure, such as CO_2, will also flash off, and thus reduce the fuel gas LHV. This, therefore, defines an optimal trade-off in terms of the flash drum pressure.

The total HC recovery from solvent at the rich solution flash drum, denoted by $f_{\mathrm{HC,g}}^{\mathrm{out}}$ [mol mol^{-1}], and the LHV of the recovered flash HC gas, $\mathrm{LHV_g}$ [MJ kg^{-1}] is computed as

$$f_{\mathrm{HC,g}}^{\mathrm{out}} = \frac{\sum N_{i,\mathrm{g}}^{\mathrm{fd}}}{\sum N_{i,\mathrm{l}}^{\mathrm{out}}} \quad , \tag{5.1}$$

$$\mathrm{LHV_g} = \sum \mathrm{y}_{i,\mathrm{g}}^{\mathrm{fd}} \mathrm{LHV}_i \quad , \tag{5.2}$$

where $N_{i,\mathrm{g}}^{\mathrm{fd}}$ [$\mathrm{kmol\,h^{-1}}$] and $\mathrm{y}_{i,\mathrm{g}}^{\mathrm{fd}}$ [$-$] are the molar flowrates and the mass fraction $i \in \{\mathrm{CH_4}, \mathrm{C_2H_6}, \mathrm{C_3H_8}\}$ in the flash gas from the rich solution drum; and the individual LHV values, LHV_i [MJ kg^{-1}] are based on ISO 6976 (ISO, 2016).

Figure 5.7 shows the effect of varying the pressure in the pilot-scale MBC rich solution flash drum on the predicted HC recovery and LHV under lean and semi-lean amine operations.

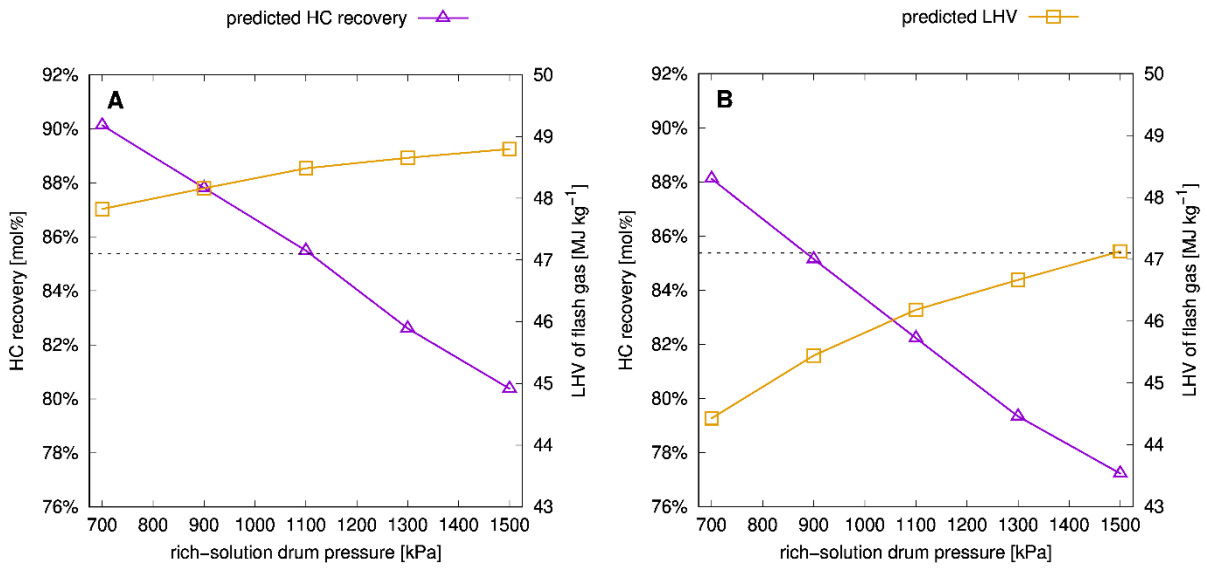

Figure 5.7: Effect of pressure in rich solution flash drum on HC recovery and LHV with NG gas and solvent flowrates of 75 kg h^{-1} and 275 L h^{-1}, under **A:** lean amine operation ($f^{in}_{CO_2,l}$ = 0.01); **B:** semi-lean amine operation ($f^{in}_{CO_2,l}$ = 0.23). **Dotted line:** fuel gas specification.

The MBC model predicts an improvement in HC recovery, from about 81% to 90% and 77% to 88%, by decreasing the rich solution flash drum pressure from 1500 kPa to 700 kPa for the lean and semi-lean operation, respectively. Notice that for the lean amine operation (Figure 5.7A), the flash gas meets the fuel gas LHV at all operating pressures and a maximum of 90% HC recovery can be obtained at 700 kPa. On the other hand, the predicted LHV_g for all the operating pressures of interest under semi-lean operation (Figure 5.7B), fail to meet the fuel gas specification except at 1500 kPa, with a lower HC recovery of 77%. The high CO_2 content in the flash gas is attributed to the higher CO_2 loading in the rich amine ($f^{out}_{CO_2,l} = 0.37$ mol mol^{-1}) from the MBC under the semi-lean operation as compared to the CO_2 loading of $f^{out}_{CO_2,l} = 0.20$ mol mol^{-1} in the lean amine operation (See Figure 5.4D). In order to recover more flash gas, further sweetening of the flash gas containing CO_2 would be required in order to use it as fuel gas (Gas Processors Suppliers Association, 2004); or else this flash gas could be compressed and returned to the MBC gas inlet or the treated gas, subject to meeting the required CO_2 purity.

5.5.3 MBC process-wide assessment of solvent losses

The amine solvent is not consumed during the acid gas removal process, but some amine loss is inevitable due to evaporation or entrainment. Unlike conventional packed columns, solvent entrainment is prevented in MBC by the microporous membrane which allows the liquid and gas phases to be in contact with each other, yet without the dispersion of one phase in the other. On the other hand, solvent evaporative losses in the form of either water, MDEA or PZ can occur with the treated gas, flash gas and acid gas streams. They are dependent on the type and concentration of amine, as well as on the temperature and pressure of the MBC, flash drum and solvent regenerator. The solvent makeup stream aims to compensate for these losses and to maintain the desired solvent concentration in the process.

Teletzke and Madhyani (2018) surveyed existing gas processing plants using monoethanolamine (MEA), diethanolamine (DEA), and MDEA, and reported an average amine loss rate of 2×10^{-4} kg Nm^{-3} of treated gas. They further noted the potential for reducing these losses to below 7×10^{-5} kg Nm^{-3} of treated gas in most gas processing systems.

Figure 5.8A shows the effect of solvent temperature at the MBC inlet on the total water, MDEA and PZ evaporative losses in the process. As the liquid temperature rises, the rates of water, MDEA and PZ evaporation also increase, due to the corresponding rise of their vapor pressures. This observation is consistent with the simulation results from Shariati and Khosravi Nikou (2015) in conventional NG sweetening process. Figure 5.8A also shows that the water evaporative loss rate is the highest followed by PZ and MDEA, which is consistent with the components respective vapor pressures (see right plot in Figure 4.13). In addition, the amine loss rate between 0.3-1.1× 10^{-4} kg Nm^{-3} is lower than, yet of same order, as the loss rates reported by Teletzke and Madhyani (2018). Overall, the amine loss is approximately 0.15% of the solvent's circulation rate (0.4 L h^{-1} of 275 L h^{-1}), and water makes over 99 wt% of these losses. This suggests that pure water make-up should be sufficient during normal operations to maintain the solvent concentration. When the amine concentration degrades or the solvent inventory in the process drops, a small portion of the amine solvent can be replaced by the fresh amine into the process.

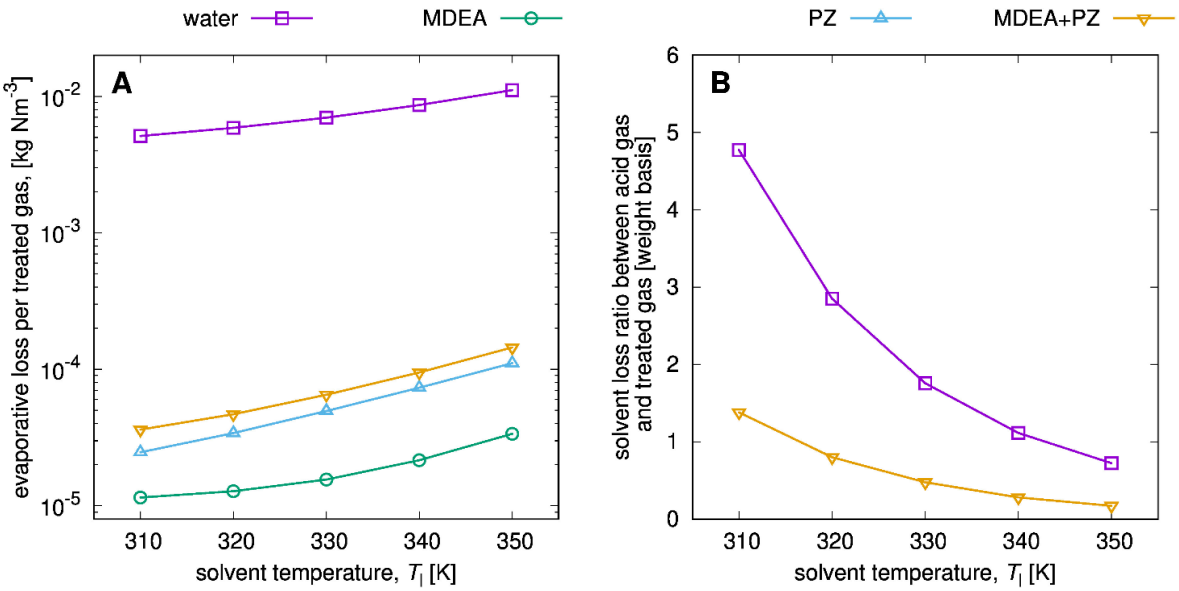

Figure 5.8: A: Effect of solvent temperature at the MBC inlet on the total water, MDEA, and PZ evaporative losses, under lean amine operation and NG gas and solvent flowrates of 75 kg h^{-1} and 275 L h^{-1}, respectively; **B:** Effect of solvent temperature at the MBC inlet on the ratio of evaporative loss in acid gas to loss in treated gas (mass basis) for water and MDEA+PZ.

Figure 5.8B presents the effect of solvent temperature into MBC on the ratio of evaporative loss in acid gas to loss in treated gas (mass basis) for water and MDEA+PZ. These results show that significant evaporative losses occur with the solvent regenerator overhead as well, which are of the same order of magnitude as the evaporative losses with the MBC treated gas. The scale-up study in the following section shows that, although small, the amine losses that occur within the MBC and regeneration section should not be neglected.

5.6 Model-based scale-up of a commercial MBC for natural gas sweetening

The objective of this section is to design a commercial MBC module (membrane area, solvent flowrate) for a semi-lean MBC operation in an industrially relevant NG sweetening application by using the knowledge acquired from the lab-scale and pilot scale studies. The inlet NG has a CO_2 content of 24 mol% to be reduced to < 6.5 mol% (Table 5.4) with flowrate of 240 MMSCFD. Notice that the amine chiller was removed as per the recommendation in Sec. 5.5.1, and the overhead condenser operates at 318 K in order to minimise amine loss to the acid gas. A model-based scale-up and analysis is conducted to assess this MBC in terms of (i) reboiler energy required per ton CO_2 removed; (ii) potential savings from the HC recovery in the rich

solution flash drum; and (iii) amount of MDEA and PZ make-up required to maintain solvent concentration.

Table 5.4: Operating conditions in an industrially relevant NG sweetening application

Parameters	Natural Gas
MBC (Absorption)	
CO_2 inlet / target outlet, $y^{in}_{CO_2,g}$ / $y^{out}_{CO_2,g}$ [mol%]	24 / < 6.5
CH_4, C_2H_6, C_3H_8 [mol%]	73 / 2 / 1
MDEA/PZ inlet [wt%]	39/5
Inlet gas pressure, P_g^{in} [kPa]	5400
Outlet liquid pressure, P_l^{out} [kPa]	5430
Gas flowrate, N_g^{in} / F_g^{in} [kmol h^{-1}] / [MMSCFD]	11,630 / 240
Liquid volumetric flowrate, F_l^{in} [m^3 h^{-1}]	1750
Gas temperature, T_g^{in} [K]	312
Liquid temperature, T_l^{in} [K]	318
CO_2 loading in solvent, $f^{in}_{CO_2,l}$ [mol mol^{-1}]	0.22
Solvent Regeneration (Desorption)	
Rich solution drum pressure [kPa]	911
Low pressure flash drum [kPa]	258
Heater temperature [K]	377
Overhead condenser – Outlet [K]	318
Reflux pump pressure – Outlet, [kPa]	258
Lean-rich exchanger	
Cold stream – Inlet / Outlet [K] / [kPa]	343 / 364 / 368
Hot stream – Inlet / Outlet [K] / [kPa]	374 / 344 / 233
LP amine pump pressure – Outlet [kPa]	711
Lean solution cooler – Outlet [K]	318
– Pressure drop [kPa]	35
Amine HP pump pressure – Outlet [kPa]	5460

The characteristics of the membrane are identical to the one used in Chapter 4 (Table 4.3), with the module cartridge inner radius, R_{m} following the pilot-scale module at 0.115 m. Table 5.5 reports the geometrical properties of the MBC used for the scale-up of an industrially relevant NG sweetening application.

Table 5.5: Specifications of the commercial-scale MBC

Parameters	**Commercial MBC module**	**Source**
Module cartridge inner radius, R_{m} [m]	0.115	(PRSB, 2017)
Number of fibers per module cartridge, N $[-]$	17,024	Eq. (3.1)
MBC module inner radius, R_{c} [m]	0.8	(PRSB, 2017)
Number of cartridges per MBC module, N_o $[-]$	31	(PRSB, 2017)
Membrane area, A_{m} [m^2]	288,687	Eq. (5.5)
Total number of module cartridges, N_{c} $[-]$	2115	Eq. (5.6)
Number of MBC modules, N_{MBC} $[-]$	69	Eq. (5.7)

Approximations of the solvent flowrate, $F_{\mathrm{l}}^{\mathrm{in}}$ and membrane area, A_{m} are first derived from the L/G ratio and CO_2 absorption flux obtained from the lab-scale experiment in Chapter 4 (Figure 4.11), which was operated under similar operating condition outlined in Table 5.5. The experimental L/G ratio, defined as the solvent flowrate per mol of CO_2 removed, and the CO_2 absorption flux were L/G = 0.86 $\mathrm{m^3\ kmol^{-1}}$ and $\Phi = 7.02 \times 10^{-3}$ $\mathrm{kmol\ m^{-2}\ hr^{-1}}$, respectively. Herein, the required solvent flowrate can thus be estimated as:

$$\eta_{\mathrm{CO_{2,g}}} = (y_{\mathrm{CO_2,g}}^{\mathrm{in}} - y_{\mathrm{CO_2,g}}^{\mathrm{out}}) N_{\mathrm{g}}^{\mathrm{in}}\,, \tag{5.3}$$

$$F_{\mathrm{l}}^{\mathrm{in}} = \eta_{\mathrm{CO_{2,g}}} \times \mathrm{L/G}\,, \tag{5.4}$$

The membrane area, A_{m} and number of module cartridges, N_{c} are determined as follows:

$$A_{\mathrm{m}} = \frac{\eta_{\mathrm{CO_{2,g}}}}{\Phi}\,, \tag{5.5}$$

$$N_{\mathrm{c}} = \frac{A_{\mathrm{m}}}{2\pi r_2 L N}\,, \tag{5.6}$$

where N_{c} is rounded to the next integer.

The total number of module cartridges, N_c is expected to be large and therefore a commercial scale module with a radius of 0.8 m, containing 31 MBC cartridges of radius 0.115 m each is considered (Figure 5.9). This design is preferred as it reduces the number of high-pressure vessels, therefore limiting reducing the physical footprint and weight of the module.

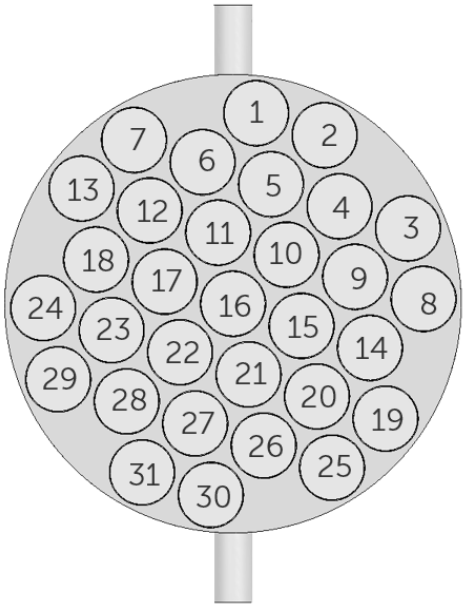

Figure 5.9: Cross-section of a commercial MBC module of 0.8 m radius- containing 31 smaller MBC cartridges of 0.115 m radius each.

Then, the number of MBC modules, N_{MBC} is determined as follow;.

$$N_{\mathrm{MBC}} = \frac{N_c}{N_o} \tag{5.7}$$

Where , N_o is the number of catridges per MBC module; and N_{MBC} is rounded to the next integer.

A model-based scale-up of the MBC plant is then conducted based on the operating conditions and MBC characteristics in Tables 5.4 and 5.5. Predicted values of the process KPIs are tabulated in Table 5.6.

Table 5.6: Model predictions of the process KPIs.

Parameters	Predicted values
CO_2 purity of treated gas, $y_{CO_2,g}^{out}$ [mol %]	6.1
CO_2 absorption flux, Φ [kmol m^{-2} hr^{-1}]	7.71×10^{-3}
L/G ratio [m^3 $kmol^{-1}$]	0.78
Reboiler energy per ton of CO_2 removed [GJ ton^{-1}]	2.2
Amount of flash gas recovered, M_g^{fd} [kg h^{-1}]	$1692 - 1908$
HC recovery in the flash gas, $f_{HC,g}^{out}$ [%]	82
Annual savings from HC recovery [US$ million yr^{-1}]	$0.96 - 1.10$
Predicted flash gas lower heating value, LHV_g [MJ kg^{-1}]	30.2
Amine loss rate per treated gas [kg Nm^{-3}]	1.24×10^{-4}
Amine loss rate per ton of CO_2 removed [kg ton^{-1}]	0.28
MDEA make-up required [ton yr^{-1}]	73
PZ make-up required, F_l^{in} [ton yr^{-1}]	144

The process-wide model predicted that the CO_2 purity at the treated gas meets the targeted specification of < 6.5 mol % with approximately 10% improvement in the CO_2 absorption flux and L/G ratio compared to the lab-scale experiment in Figure 4.11. This is attributed to operating the solvent inlet temperature at a higher temperature of 318 K, in order to eliminate the requirement of amine chiller before the MBC as per the recommendation in Sec. 5.5.1. It is also found that an increase in solvent temperature improves the CO_2 absorption flux, despite the slight increase in the average membrane wetting; whereby the increase in mass transfer due to higher reaction rates and diffusivities of CO_2 and amines, dominates over the decreased in CO_2 solubility in the amine solvent.

The predicted reboiler energy per ton of CO_2 removed is 2.2 GJ ton^{-1}, which is lower compared to the range of 2.4 – 4.2 GJ ton^{-1}, typically reported for amine-based absorption process (Dave et al., 2009; Liebenthal et al., 2013; Narku-Tetteh et al., 2018). This can be attributed to the semi-lean operation of the MBC system, which was shown to reduce the energy consumption in Sec. 5.5.1. In addition, model predicted the amine loss rate per treated gas is 1.35×10^{-4} kg Nm^{-3}, which is below the average amine loss rates of 2×10^{-4} kg Nm^{-3} in the survey by the Teletzke and Madhyani (2018). Similarly, the predicted amine loss per ton

of CO_2 removed of 0.28 kg ton^{-1}, is at the lower end of the range 0.35 – 2.0 kg ton^{-1} that is typically reported for amine-based processes (Bailey and Feron, 2005). The resulting solvent make-up, are 73 and 144 ton yr^{-1} for MDEA and PZ, respectively.

Finally, a sensitivity analysis of ±5% on the Henry's constants of light HC in the solvent was simulated to determine how uncertainty in the Henry's constant propagates into the estimation of the amount of flash gas recovered at the rich solution flash drum and its heating value, which are used to quantify the annual savings from HC recovery. The predicted amount of flash gas recovered is $1692 - 1908$ kg hr^{-1}, corresponding to +5% and -5% of the Henry's constant of light HC in the solvent, respectively. On the other hand, the predicted heating value of the flash gas LHV_g and HC recovery is 30 MJ kg^{-1} and 82%, respectively. Similar to the findings in Sec. 5.5.2 for semi-lean operation, the predicted LHV_g is lower than the fuel gas specification of 47.1 MJ kg^{-1}, which is due to the high CO_2 content of the flash gas. A sensitivity analysis of the operating pressure of the flash drum up to 1500 kPa only shows improvement of the LHV_g to 37 MJ kg^{-1}, yet with a lower HC recovery of 68%. The high CO_2 content in the flash gas is attributed to the higher CO_2 loading in the rich amine ($f^{\text{out}}_{\text{CO}_2,\text{l}} = 0.56$ mol mol^{-1}) from the MBC compared to the CO_2 loading of $f^{\text{out}}_{\text{CO}_2,\text{l}} = 0.38$ mol mol^{-1} in the pilot-scale experiment in Sec. 5.4. Therefore, the flash gas containing CO_2 will require sweetening at the top section of the flash drum in order to be used as fuel gas (Gas Processors Suppliers Association, 2004); or else this flash gas could be compressed and returned to the MBC gas inlet. The annual cost savings from flash gas recovery is high, estimated to be

$$\sum M^{\text{fd}}_{i,\text{g}} \, \text{LHV}_\text{g} \, t_{\text{op}} E_\text{c} = \text{ US\$ } 0.96 - 1.1 \text{ million yr}^{-1} \tag{5.8}$$

where $M^{\text{fd}}_{i,\text{g}}$ [kg hr^{-1}] and LHV_g [MJ kg^{-1}] denote the mass flowrate of species $i \in \{\text{CH}_4, \text{C}_2\text{H}_6, \text{C}_3\text{H}_8\}$ in the flash gas and the flash gas lower heating value; the number of operating hours per year, $t_{\text{op}} = 8000$ hr yr^{-1}, and the energy cost is $E_\text{c} = 2.4 \times 10^{-3}$ USD MJ^{-1} (U.S. Energy Information Administration, 2019), which corresponds to +5% and -5% of the Henry's constant of light HC in the solvent, respectively. Based on the predictions of the annual cost savings, an economic assessment could be conducted to determine whether to invest capital cost to sweeten the flash gas, or to recompress and recyle the flash gas to the MBC gas inlet, or to send the flash gas to the flare header.

Overall, the intensification potential of the scaled-up MBC commercial module showed promising prospects, whereby (i) the predicted reboiler energy per ton of CO_2 removed is lower than the conventional amine absorption column by 12 - 50%; (ii) the predicted amine loss rate per treated gas and per ton of CO_2 removed are lower compared to the typical loss rates reported in a conventional amine-based processes; and (iii) a potential savings of US$ $0.96 - 1.1$ million yr^{-1} from the HC recovery can be realized, subject to further sweetening of the flash gas. Nevertheless, the total number of MBC modules (69) will require footprint area of ca. 250 m^2, implying that MBC may require larger footprint than conventional absorption column. Further improvement on the membrane characteristics such as the specific surface area and the hydrophobicity are required to enable commercial MBC modules to be stacked, thereby improving the intensification potential in terms of footprint.

5.7 Conclusions

This chapter has integrated the MBC unit (*i.e.,* absorption section) with the solvent regeneration unit (*i.e.,* desorption section) in a full-scale MBC process for NG sweetening. In addition to predicting the CO_2 removal performance, light HC absorptions into solvent and solvent loss due to evaporation, the process-wide model can predict the process energy duty of all the equipment, the HC recovery rate and the solvent make-up under different operating conditions. Verification of the model has been conducted using data from the pilot plant, showing a close agreement of the predictions with measured energy consumption and CO_2 removal performance at various CO_2 loadings in the solvent.

The experimental data and model analysis has confirmed the advantages of semi-lean operation in terms of energy reduction and physical footprint. The results suggest that semi-lean operation is sufficient for bulk CO_2 removal to meet sales gas specification, while lean amine operation is required for deep CO_2 removal in order to meet LNG specification. The optimum operating pressure for the rich solution flash drum could also be determined, in order to maximise HC recovery from the solvent, while meeting the fuel gas LHV specification. In addition, the evaporation rate of the solvent has been predicted to be predominantly water, and therefore, pure water make-up should be sufficient to maintain the amine concentration in the

solvent during normal operation. In addition, the predicted amine loss rate has been found to be within the typically reported loss rates for conventional CO_2 absorption process.

Finally, the scale-up of a commercial MBC has been conducted for a semi-lean MBC operating in an industrially relevant NG sweetening application in order to meet a CO_2 purity of < 6.5 mol%. The method to predict the required solvent flowrate and membrane area for the commercial-scale MBC has used knowledge of the experimental L/G ratio and CO_2 absorption flux from existing lab-scale experiments as a first approximation. The predicted reboiler energy per ton of CO_2 removed is lower than the range typically reported for amine-based processes, mainly due to the semi-lean operation. However, the flash gas from the flash drum may need to undergo further sweetening in order to be used as fuel gas due to high CO_2 loading in rich amine. Lastly, the predicted amine loss rate per treated gas and per ton of CO_2 removed is below the typical loss rates reported in conventional amine-based processes. These full-scale MBC results could provide the base case in a systematic model-based optimisation to improve the design and operation of commercial MBC modules as part of future work.

Chapter 6 Conclusion and Future Work

Over the past decade, MBC for CO_2 absorption has been widely recognised for its large intensification potential compared to conventional absorption towers. However, no literature to date has conducted a comprehensive process wide assessment of using MBC for NG sweetening. The main objective of this work is to develop a process-wide modelling of NG sweetening using MBC to enable MBC process design and performance assessment. To achieve the objective, mathematical modeling with experimental verifications were conducted. For the experiments, literature reviews were conducted to identify and select the suitable type of MBC, membrane-solvent combination and fluid flow configuration to be used in the MBC lab and pilot-scale test rigs. For the MBC modeling, a predictive mathematical model is developed to investigate the acid gas absorption mechanism in MBC and the impact of various parameters such as membrane characteristics, operating parameters, and flow configurations in NG sweetening applications. Then, an integrated MBC process model was developed whereby the effects of various design configuration, operating conditions and scale-up of a commercial MBC for NG sweetening were conducted. The following subsections summarize the key contributions and the recommendations for future works.

6.1 Summary of key contributions

In Chapter 2, literature reviews found that counter-current longitudinal MBC modules are widely used in lab scale studies due to the simplicity in manufacturing, well-known fluid dynamics in shell and tube side and relative easiness of mass transfer estimation. Several studies have reported that PTFE hollow fiber with alkanolamines exhibit high hydrophobicity, chemical, and thermal stability and high CO_2 removal performance after a prolonged period of operation in MBC.

Numerous publications on modelling of MBC for CO_2 capture have reported a good agreement of model results with experimental data, eventhough different modelling strategies were adopted, ranging from a simple constant overall mass transfer coefficient K_L, to sophisticated 2D modelling consisting of convection, diffusion and reaction phenomena.

Moreover, most studies conducted experiments using binary mixtures such as CO_2/N_2 or CO_2/CH_4 at atmospheric pressure in the laboratory; while experiments on multi-component gas mixtures (i.e., natural gas) have not been performed to verify the CO_2 absorption performance.

Therefore, longitudinal MBC modules with PTFE hollow fiber-alkanolamines solvent operating in the counter-current fluid flow configuration are selected to be used in high-pressure MBC in the lab-scale and pilot-scale test rigs with CO_2 rich natural gas throughout this thesis.

In Chapter 3, a predictive mathematical model of high-pressure MBC for NG sweetening applications with aqueous alkanolamine mixtures of MDEA and PZ as the chemical solvent was developed. The model explicitly accounts for the rates of mass transfer through the membrane, diffusion and chemical reaction in the liquid phase. A combination of 1-d and 2-d mass-balance equations to predict the CO_2 absorption flux was considered, whereby the degree of membrane wetting itself is calculated using the Laplace-Young equation based upon knowledge of the membrane pore-size distribution, fluid flow configuration, and operating conditions. Also, real gas behavior is accounted for due to high-pressure operation, and Henry's law is applicable at the gas-liquid interface.

The predictive capability of the model is tested against data from two experimental settings operating in a vertical orientation: a lab-scale MBC module, where the purification is conducted using binary gas mixtures of CH_4/CO_2 and N_2/CO_2 at 11 bar; and a pilot-scale MBC module operated under industrially relevant conditions at a natural gas processing plant in Malaysia. All model predictions showed a close agreement with measured CO_2 absorption flux, *i.e.,* within ±5% at various gas and liquid flowrate, subject to a temperature correction to account for the heat of reaction in the liquid phase for the pilot-scale MBC modules due to operating at a lower L/G ratio.

The model's ability to predict the variation in membrane wetting along the fiber length makes it possible to analyze the effects of vertical and horizontal modes of operation, whereby horizontal mode of operation is not subject to liquid static head, thereby decreasing the membrane wetting and increasing the CO_2 removal efficiency, respectively. Consequently, horizontal operation is experimented in the lab and pilot-scales in Chapter 4.

In Chapter 4, the MBC model was further refined to predict CO_2 absorption under lean and semi-lean operating conditions, that includes the modeling solvent losses from evaporation and light hydrocarbon absorption into the amine solvent. An energy balance has also been added to the model, which enables predicting the temperature profile in the MBC by accounting for the CO_2 absorption heat of reaction and heat losses from solvent evaporation.

An experimental verification of the model has been conducted using both lab-scale and pilot-scale MBC modules, now in a horizontal orientation, using an improved membrane fiber compared to Chapter 3. The experimental result showed that the CO_2 absorption flux has improved by nearly 80% and the membrane wetting has reduced to less than 1% for the pilot-scale MBC. A close agreement of all the model predictions with measured CO_2 absorption fluxes has been observed at various CO_2 loading in solvent, gas and liquid flowrates, and CO_2 inlet concentrations.

The predicted molar flowrates of light hydrocarbons against the measured flowrates in the flashed gas from the rich amine flash drum verified the assumption that the solvent is about saturated with hydrocarbons at the MBC outlet. Therefore, this prediction can help to determine the amount of HC that can be recovered in the downstream flash drum to minimize product loss. The model also predicts that water is predominantly evaporated to the treated gas compared to MDEA and PZ due to their vapor pressures being much lower compared to water in the temperature range of interest. In addition, only a small amount of solvent is evaporated compared to the total solvent flowrate in the high-pressure pilot-scale MBC operation, and therefore solvent evaporation has a minimal impact on the solvent outlet temperature. This prediction was confirmed by the close agreement between predicted and measured temperature profile in the lab-scale MBC. The ability to predict the solvent evaporation rate and its composition will enable quantifying the amount of solvent make-up required in a full-scale MBC process.

In Chapter 5, the MBC model developed in Chapter 4 is integrated with the conventional solvent regeneration model in a full-scale MBC process for NG sweetening in the gPROMS ProcessBuilder environment, which can now predict the key performance indicators (KPIs) such as: (a) the CO_2 purity in the product gas; (b) the process duty and the energy per ton CO_2 removed; (c) the amount of HC loss or recovered as fuel gas; and (d) the amount of solvent

loss per treated gas and makeup required for various conceptual designs and operating conditions. Verification of the model has been conducted using data from the pilot plant, showing a close agreement of the predictions with the measured energy consumption and CO_2 removal efficiencies at various CO_2 loadings in the solvent.

From the experimental data and model analysis, semi-lean operation is advantageous in terms of energy reduction and physical footprint for bulk CO_2 removal to meet sales gas specification, while lean amine operation is required for deep CO_2 removal in order to meet LNG specification. Optimum operating pressure for the rich solution flash drum could also be determined in order to maximise HC recovery from the solvent, while meeting the fuel gas LHV specification. Likewise in Chapter 4, the evaporation rate of the solvent in the process-wide has been predicted to be predominantly water, and therefore, pure water make-up should be sufficient to maintain the amine concentration in the solvent during normal operation. In addition, the predicted amine loss rate has been found to be within the typically reported loss rates for conventional CO_2 absorption process.

Finally, the model-based scale-up of a commercial MBC was conducted for a semi-lean MBC operating in an industrially relevant NG sweetening application in order to assess its intensification potential, which showed promising prospects in all the key performance indicators. Nevertheless, the required MBC footprint area is ca. 250 m^2, implying a larger footprint compared to the conventional absorption column. Overall, the resulting full-scale MBC could provide the base case in a systematic model-based optimisation to improve the design and operation of commercial MBC modules.

6.2 Recommendations for future work

The MBC model developed in this work can be continuously improved as a result of increased in knowledge, computational power and access to new data information. The critical points of improvement, both in terms of a more in-depth understanding of acid gas absorption in MBC and modeling are summarized below:

- MBC model can be used for the development of improved membrane. Global sensitivity analysis (GSA) can be conducted to rank the membrane characteristics and operating conditions that have the most significant impact on CO_2 removal performance and costs. It provides insight on which membrane characteristics to focus on and to be improved further by the membrane manufacturer. In addition, it helps to identify the key decision variables to be used for a model-based optimization problem (e.g., minimizing the annualized cost).

- Sensitivity analysis of the optimized MBC module concerning the MBC material cost, lifespan and energy unit cost be conducted for the NG sweetening application. Then, a detailed techno-economic assessment framework comprising various criteria such as technical, economic, operational, maintenance and technology risks can be developed with appropriate weightages and scores to benchmark against the conventional packed column. The development of the framework can then be used to systematically identify the gaps and improvements for MBC technology.

- Modeling and experiments should be conducted for different MDEA and PZ concentrations or other commonly used chemical solvents such as MEA to identify optimal solvents for MBC in terms of CO_2 removal absorption performance and solvent regeneration costs.

- To utilize other thermodynamic property package such as SAFT Equation of State to obtain the thermo-physical parameters and to evaluate the MBC based NG sweetening process in terms of CO_2 removal, HC absorption and energy consumption.

- Computational fluid dynamic (CFD) modeling to investigate the flow distribution of the gas and liquid into the hollow fiber tube and shell of MBC modules to help ensure

even fluid flow distribution and to select the optimal arrangement of MBC multi-stage cascade modules.

- The model should be checked against experiments with various MBC flow configurations such as co-current, gas in shell and liquid in hollow fiber tubes, respectively and for a better understanding of CO_2 absorption in MBC.

- The model and experiments should be extended to include simultaneous acid gas absorption (i.e., CO_2 and H_2S) for a comprehensive assessment of NG sweetening using MBC.

- The effects of gas temperature changes on MBC performance is not considered as the gas mass transfer resistance are negligible, and the gas diffusivities are four (4) orders of magnitude greater than liquid diffusivities. However, depending on the feed gas temperature to MBC, the colder gas absorbs heat from the hot liquid causing the gas temperature to increase and liquid temperature to decrease which may result in a temperature bulge at the end of the MBC length. The potential effect of such a phenomenon on MBC performance is presently unknown. Also, the temperature increase in treated gas may have an impact on the downstream equipment, and therefore should be considered. The physical and thermodynamic properties related to temperature changes along MBC and its effect on membrane wetting and CO_2 absorption can also be considered.

- Using the same principle, MBC for solvent regeneration (CO_2 desorption) can be considered as an alternative potential to a conventional desorption column (Koonaphapdeelert et al., 2009; Wang et al., 2013). Modeling of integrated MBC process for CO_2 absorption-desorption can be conducted to assess its potential in NG Sweetening.

Bibliography

Addington, L. and Ness, C. (2010) 'An evaluation of general "rules of thumb" in amine sweetening unit design and operation', *GPA Annual Convention Proceedings*, 1, pp. 119–135.

Al-Baghli, N. A., Pruess, S. A., Yesavage, V. F. and Selim, M. S. (2001) 'A rate-based model for the design of gas absorbers for the removal of CO_2 and H_2S using aqueous solutions of MEA and DEA', *Fluid Phase Equilibria*, 185(1–2), pp. 31–43. doi: 10.1016/S0378-3812(01)00454-X.

Al-Marzouqi, M., El-Naas, M., Marzouk, S. and Abdullatif, N. (2008) 'Modeling of chemical absorption of CO_2 in membrane contactors', *Separation and Purification Technology*, 62(3), pp. 499–506. doi: 10.1016/j.seppur.2008.02.009.

Al-Marzouqi, M. H., El-Naas, M. H., Marzouk, S. A. M., Al-Zarooni, M. A., Abdullatif, N. and Faiz, R. (2008) 'Modeling of CO_2 absorption in membrane contactors', *Separation and Purification Technology*, 59(3), pp. 286–293. doi: 10.1016/j.seppur.2007.06.020.

Al-Marzouqi, M. H., Marzouk, S. a M., El-naas, M. H. and Abdullatif, N. (2009) 'CO_2 Removal from CO_2 - CH_4 Gas Mixture Using Different Solvents and Hollow Fiber Membranes', pp. 3600–3605. doi: 10.1021/ie800977z.

Alie, C. F. (2004) 'CO_2 Capture With MEA: Integrating the Absorption Process and Steam Cycle of an Existing Coal-Fired Power Plant', *Master Thesis, University of Waterloo*.

Bailey, D. W. and Feron, P. H. M. (2005) 'Post-combustion decarbonisation processes', *Oil and Gas Science and Technology*, 60(3), pp. 461–474. doi: 10.2516/ogst:2005028.

Bensetiti, Z., Iliuta, I., Larachi, F. and Grandjean, B. P. . (1999) 'Solubility of Nitrous Oxide in Amine Aqueous Solutions', *Ind. Eng.Chem.Res*, pp. 328–332. doi: 10.1021/je990253b.

Billet, R. and Schultes, M. (1999) 'Prediction of mass transfer columns with dumped and arranged packings', *Trans IChemE*, 77. pp. 501. doi: 10.1205/026387699526520.

Bird, R. B., Lightfoot, E. N. and Stewart, W. E. (1960) *Transport Phenomena*. John Wiley & Sons.

Boributh, S., Assabumrungrat, S., Laosiripojana, N. and Jiraratananon, R. (2011) 'A modeling study on the effects of membrane characteristics and operating parameters on physical absorption of CO_2 by hollow fiber membrane contactor', *Journal of Membrane Science*. Elsevier B.V., 380(1–2), pp. 21–33. doi: 10.1016/j.memsci.2011.06.029.

Boributh, S., Rongwong, W., Assabumrungrat, S., Laosiripojana, N. and Jiraratananon, R. (2012) 'Mathematical modeling and cascade design of hollow fiber membrane contactor for CO_2 absorption by monoethanolamine', *Journal of Membrane Science*. Elsevier B.V., 401–402, pp. 175–189. doi: 10.1016/j.memsci.2012.01.048.

Boucif, N., Corriou, J. P., Roizard, D. and Favre, E. (2012) 'Carbon Dioxide Absorption by Monoethanolamine in Hollow Fiber Membrane Contactors: A Parametric Investigation', *AIChE Journal*, Vol 58(9), pp. 2843–2855. doi: 10.1002/aic.12791.

Boucif, N., Roizard, D., Corriou, J.-P. and Favre, E. (2015) 'To What Extent Does Temperature Affect Absorption in Gas-Liquid Hollow Fiber Membrane Contactors?', *Separation Science and Technology*, 50(9), pp. 1331–1343. doi: 10.1080/01496395.2014.969807.

Carroll, J. J., Maddocks, J. and Mather, A. E. (1998) 'The solubility of hydrocarbons in amine solutions', *Laurance Reid Gas Conditioning Conference*, (March), pp. 44–64.

Chabanon, E., Roizard, D. and Favre, E. (2013) 'Modeling strategies of membrane contactors for post-combustion carbon capture: A critical comparative study', *Chemical Engineering Science*. Elsevier, 87, pp. 393–407. doi: 10.1016/j.ces.2012.09.011.

Chan, Z. P., Saleh, S. M., Yusop, N. M. and Abai, M. (2013) 'Removal of CO_2 using membrane contactor and ionic liquid project'. Final Report, PETRONAS Research Sdn Bhd.

Chemeo (2017) *Chemical Properties of Methyldiethanolamine (CAS 105-59-9) and Piperazine (CAS 110-85-0)*. Available at: https://www.chemeo.com/cid/60-936-6/Methyldiethanolamine/ (Accessed: 2 January 2017).

Constantinou, A. (2011) *CO_2 Absorption in Microstructured Membrane Reactors*. PhD Thesis, University College London.

Cormos, A. M. and Daraban, I. M. (2015) 'Dynamic modeling and validation of amine-based CO_2 capture plant', *Applied Thermal Engineering*. Elsevier Ltd, 74, pp. 202–209. doi: 10.1016/j.applthermaleng.2013.12.045.

Cui, L., Ding, Z., Liu, L. and Li, Y. (2015) 'Modelling and Experimental Study of Membrane Wetting in Microporous Hollow Fiber Membrane Contactors', *The Canadian Journal of Chemical Engineering*, 93(7), pp. 1254–1265. doi: 10.1002/cjce.22210.

Cussler, E. L. (2009) *Diffusion: Mass Transfer in Fluid Systems*. Third. Cambridge University Press, New York.

Dahlquist, E., Lv, Y., Yu, X., Tu, S. and Yan, J. (2010) 'Wetting of polypropylene hollow fiber membrane contactors', *Journal of Membrane Science*. Elsevier B.V., 362(1–2), pp. 444–452. doi: 10.1016/j.memsci.2010.06.067.

Dave, N., Do, T., Puxty, G., Rowland, R., Feron, P. H. M. and Attalla, M. I. (2009) 'CO_2 capture by aqueous amines and aqueous ammonia-A Comparison', *Energy Procedia*. Elsevier, 1(1), pp. 949–954. doi: 10.1016/j.egypro.2009.01.126.

deMontigny, D., Tontiwachwuthikul, P. and Chakma, A. (2006) 'Using polypropylene and polytetrafluoroethylene membranes in a membrane contactor for CO_2 absorption', *Journal of Membrane Science*, 277, pp. 99–107. doi: 10.1016/j.memsci.2005.10.024.

Deshmukh, S. P. and Li, K. (1998) 'Effect of ethanol composition in water coagulation bath on morphology of PVDF hollow fibre membranes', *Journal of Membrane Science*, 150(1), pp. 75–85. doi: 10.1016/S0376-7388(98)00196-3.

Dindore, V. Y. (2003) *Gas Purification using Membrane Gas Absorption Processes*. PhD Thesis, University of Twente, the Netherlands.

Dindore, V. Y. and Versteeg, G. F. (2005) 'Gas–liquid mass transfer in a cross-flow hollow fiber module: Analytical model and experimental validation', *International Journal of Heat and Mass Transfer*, 48(16), pp. 3352–3362. doi: 10.1016/j.ijheatmasstransfer.2005.03.002.

Drioli, E., Criscuoli, A. and Curcio, E. (2005) 'Membrane Contactors: Fundamentals, Applications and Potentialities ; Chapter 2 . Membrane materials', *Elsevier Science*, pp. 40–104.

EIA (2016) '*International Energy Outlook 2016*'. Available at: doi:www.eia.gov/forecasts/ieo/pdf/0484(2016).pdf (Accessed: 2 January 2019).

Engineering ToolBox (2003) *Fuels - Higher and Lower Calorific Values*. Available at: https://www.engineeringtoolbox.com/fuels-higher-calorific-values-d_169.html (Accessed: 2 January 2019).

Engineering ToolBox (2010) *Water - Heat of Vaporization*. Available at: https://www.engineeringtoolbox.com/water-properties-d_1573.html (Accessed: 2 January 2017).

Eslami, S., Mousavi, S. M., Danesh, S. and Banazadeh, H. (2011) 'Modeling and simulation of CO_2 removal from power plant flue gas by PG solution in a hollow fiber membrane contactor', *Advances in Engineering Software*. Elsevier Ltd, 42(8), pp. 612–620. doi: 10.1016/j.advengsoft.2011.05.002.

Faiz, R. and Al-Marzouqi, M. (2010) 'CO_2 removal from natural gas at high pressure using membrane contactors: Model validation and membrane parametric studies', *Journal of Membrane Science*. Elsevier B.V., 365(1–2), pp. 232–241. doi: 10.1016/j.memsci.2010.09.004.

Faiz, R., El-Naas, M. H. and Al-Marzouqi, M. (2011) 'Significance of gas velocity change during the transport of CO_2 through hollow fiber membrane contactors', *Chemical Engineering Journal*. Elsevier B.V., 168(2), pp. 593–603. doi: 10.1016/j.cej.2011.01.029.

Falk-Pedersen, O. and Dannström, H. (1997) 'Separation of carbon dioxide from offshore gas turbine exhaust', *Energy Conversion and Management*, 38, pp. S81–S86. doi: 10.1016/S0196-8904(96)00250-6.

Favre, E. (2011) 'Membrane processes and postcombustion carbon dioxide capture: Challenges and prospects', *Chemical Engineering Journal*. Elsevier B.V., 171(3), pp. 782–793. doi: 10.1016/j.cej.2011.01.010.

Gaspar, J., Gladis, A., Woodley, J. M., Thomsen, K., Von Solms, N. and Fosbøl, P. L. (2017) 'Rate-based Modelling and Validation of a Pilot Absorber Using MDEA Enhanced with Carbonic Anhydrase (CA)', Energy Procedia. The Author(s), 114(November 2016), pp. 707–718. doi: 10.1016/j.egypro.2017.03.1213.

Gas Processors Suppliers Association (2004) *GPSA Engineering Data Book , Section 21 : Hydrocarbon Treating*.

Ghasem, N., Al-Marzouqi, M. and Abdul Rahim, N. (2013) 'Modeling of CO_2 absorption in a membrane contactor considering solvent evaporation', *Separation and Purification Technology*. Elsevier B.V., 110, pp. 1–10. doi: 10.1016/j.seppur.2013.03.008.

Goyal, N., Suman, S. and Gupta, S. K. (2015) 'Mathematical modeling of CO_2 separation from gaseous-mixture using a Hollow-Fiber Membrane Module: Physical mechanism and influence of partial-wetting', *Journal of Membrane Science*. Elsevier, 474, pp. 64–82. doi: 10.1016/j.memsci.2014.09.036.

Hatcher, N., Jones, C. and Weiland, R. (2013) 'Solubility of hydrocarbons and light ends in amines'. Optimized Gas Treating, Inc. Available at: https://www.protreat.com/files/publications/80/ogrt-0.pdf (Accessed: 3 January 2018).

He, X. and Hägg, M. B. (2012) 'Membranes for environmentally friendly energy processes', *Membranes*, 2(4), pp. 706–726. doi: 10.3390/membranes2040706.

Hoff, K. A., Juliussen, O., Falk-Pedersen, O. and Svendsen, H. F. (2004) 'Modeling and Experimental Study of Carbon Dioxide Absorption in Aqueous Alkanolamine Solutions using a Membrane Contactor', *Industrial & Engineering Chemistry Research*, pp. 4908–4921.

Hoff, K. A. (2003) *Modeling and Experimental Study of Carbon Dioxide Absorption in a Membrane Contactor*, *Science And Technology*. PhD Thesis, Norwegian University of Science and Technology.

Hoff, K. A. and Svendsen, H. F. (2013) 'CO_2 absorption with membrane contactors vs. packed absorbers- Challenges and opportunities in post combustion capture and natural gas sweetening', *Energy Procedia*. Elsevier B.V., 37(1876), pp. 952–960. doi: 10.1016/j.egypro.2013.05.190.

Hoff, K. A. and Svendsen, H. F. (2014) 'Membrane contactors for CO_2 absorption - Application, modeling and mass transfer effects', *Chemical Engineering Science*. Elsevier, 116, pp. 331–341. doi: 10.1016/j.ces.2014.05.001.

Honeywell UOP (2014) 'Regeneration Section for PETRONAS CO2 Pilot Plant'.

Hydrogen Tools (2019) *Lower and Higher Heating Values of Hydrogen and Other Fuels*. Available at: https://h2tools.org/hyarc/hydrogen-data/lower-and-higher-heating-values-hydrogen-and-other-fuels (Accessed: 2 January 2019).

IEA (2004) 'Energy Technology Analysis: Prospects for CO_2 Capture and Storage', pp. 1–249. doi: 10.1016/B978-1-85617-710-8.00010-8.

ISO (2016) *Natural gas - Calculation of calorific values, density, relative density and Wobbe index from composition*.

Iversen, S. B., Bhatia, V. K., Dam-Johansen, K. and Jonsson, G. (1997) 'Characterization of microporous membranes for use in membrane contactors', *Elsevier, Membrane Science*, 130, pp. 205–217. doi: 10.1016/S0376-7388(97)00026-4.

Kabadi, V. N. (2007) 'Heat of Dissolution Measurements for CO_2 in Mixed Alkanolamine Solvents', *Final Report DE-FG26-03NT41912. North Carolina A&T State University, Greensbor*.

Kamo, J., Hirai, T. and Kamada, K. (1992) 'Solvent-induced morphological change of microporous hollow fiber membranes', *Journal of Membrane Science*, 70(2–3), pp. 217–224. doi: 10.1016/0376-7388(92)80107-U.

Kang, G., Chan, Z. P., Saleh, S. B. M. and Cao, Y. (2017) 'Removal of high concentration CO_2 from natural gas using high pressure membrane contactors', *International Journal of Greenhouse Gas Control*. Elsevier Ltd, 60, pp. 1–9. doi: 10.1016/j.ijggc.2017.03.003.

Keshavarz, P., Fathikalajahi, J. and Ayatollahi, S. (2008) 'Analysis of CO_2 separation and simulation of a partially wetted hollow fiber membrane contactor', *Journal of Hazardous Materials*, 152(3), pp. 1237–1247. doi: 10.1016/j.jhazmat.2007.07.115.

Khaisri, S., deMontigny, D., Tontiwachwuthikul, P. and Jiraratananon, R. (2009a) 'Comparing membrane resistance and absorption performance of three different membranes in a gas absorption membrane contactor', *Separation and Purification Technology*, 65, pp. 290–297. doi: 10.1016/j.seppur.2008.10.035.

Khaisri, S., deMontigny, D., Tontiwachwuthikul, P. and Jiraratananon, R. (2009b) 'Comparing membrane resistance and absorption performance of three different membranes in a gas absorption membrane contactor', *Separation and Purification Technology*, 65(3), pp. 290–297. doi: 10.1016/j.seppur.2008.10.035.

Khaisri, S., deMontigny, D., Tontiwachwuthikul, P. and Jiraratananon, R. (2010) 'A mathematical model for gas absorption membrane contactors that studies the effect of partially wetted membranes', *Journal of Membrane Science*, 347(1–2), pp. 228–239. doi: 10.1016/j.memsci.2009.10.028.

Kidnay, A. J. and Parrish, W. R. (2006) *Fundamentals of Natural Gas Processing*, *Fundamentals of Natural Gas Processing*. CRC Press. doi: 10.1201/b14397.

Ko, J. and Li, M. (2000) 'Kinetics of absorption of carbon dioxide into solutions of N - methyldiethanolamine # water', *Chemical Engineering Science*, 55, pp. 4139–4147. doi: 10.1016/S0009-2509(00)00079-8.

Koonaphapdeelert, S., Wu, Z. and Li, K. (2009) 'Carbon dioxide stripping in ceramic hollow fibre membrane contactors', *Chemical Engineering Science*, 64, pp. 1–8. doi: 10.1016/j.ces.2008.09.010.

Kreulen, H., Smolders, C. a., Versteeg, G. F. and Van Swaaij, W. P. M. (1993) 'Microporous hollow fibre membrane modules as gas-liquid contractors. Part 2. Mass transfer with chemical reaction', *Journal of Membrane Science*, 78(3), pp. 217–238. doi: 10.1016/0376-7388(93)80002-F.

Krishna, R. and Wesselingh, J. A. (1997) 'The Maxwell-Stefan approach to mass transfer', *Science*, 52(6), pp. 861–911.

Kvamsdal, H. M. and Rochelle, G. T. (2008) 'Effects of the temperature bulge in CO_2 absorption from flue gas by aqueous monoethanolamine', *Industrial and Engineering Chemistry Research*, 47(3), pp. 867–875. doi: 10.1021/ie061651s.

Li, J. L. and Chen, B. H. (2005) 'Review of CO_2 absorption using chemical solvents in hollow fiber membrane contactors', *Separation and Purification Technology*, 41(2), pp. 109–122. doi: 10.1016/j.seppur.2004.09.008.

Li, K. (2015) *Membrane Science and Membrane Separation Processes*. ChE 413 Lecture notes. Department of Chemical Engineering & Chemical Technology, Imperial College London.

Li, S., Pyrzynski, T. J., Klingho, N. B., Tamale, T., Zhong, Y., Aderhold, J. L., Zhou, S. J., Meyer, H. S., Ding, Y., *et al.* (2017) 'Scale-up of PEEK hollow fiber membrane contactor for post-combustion CO_2 capture', *Journal of Membrane Science,* 527(January), pp. 92–101. doi: 10.1016/j.memsci.2017.01.014.

Liebenthal, U., Di D. Pinto, D., Monteiro, J. G. M. S., Svendsen, H. F. and Kather, A. (2013) 'Overall process analysis and optimisation for CO2 Capture from coal fired power plants based

on phase change solvents forming two liquid phases', *Energy Procedia*. Elsevier B.V., 37, pp. 1844–1854. doi: 10.1016/j.egypro.2013.06.064.

Liu, L., Li, L., Ding, Z., Ma, R. and Yang, Z. (2005) 'Mass transfer enhancement in coiled hollow fiber membrane modules', *Journal of Membrane Science*, 264(1–2), pp. 113–121. doi: 10.1016/j.memsci.2005.04.035.

Lu, J. G., Zheng, Y. F. and Cheng, M. D. (2008) 'Wetting mechanism in mass transfer process of hydrophobic membrane gas absorption', *Journal of Membrane Science*, 308(1–2), pp. 180–190. doi: 10.1016/j.memsci.2007.09.051.

Lu, J., Wang, L., Sun, X., Li, J. and Liu, X. (2005a) 'Absorption of CO_2 into aqueous solutions of methyldiethanolamine and activated methyldiethanolamine from a gas mixture in a hollow fiber contactor', *Industrial and Engineering Chemistry Research*, 44, pp. 9230–9238. doi: 10.1021/ie058023f.

Lu, J., Wang, L., Sun, X., Li, J. and Liu, X. (2005b) 'Absorption of CO_2 into aqueous solutions of methyldiethanolamine and activated methyldiethanolamine from a gas mixture in a hollow fiber contactor', *Industrial and Engineering Chemistry Research*, 44(24), pp. 9230–9238. doi: 10.1021/ie058023f.

Mac Dowell, N., Florin, N., Buchard, A., Hallett, J., Galindo, A., Jackson, G., Adjiman, C. S., Williams, C. K., Shah, N., *et al.* (2010) 'An overview of CO_2 capture technologies', *Energy & Environmental Science*, 3(11), p. 1645. doi: 10.1039/c004106h.

Malek, A., Li, K. and Teo, W. K. (1997) 'Modeling of Microporous Hollow Fiber Membrane Modules operated under Partially Wetted Conditions', *Industrial & Engineering Chemistry Research*, pp. 784–793.

Mandal, B. P., Kundu, M. and Bandyopadhyay, S. S. (2003) 'Density and viscosity of aqueous solutions of (N-methyldiethanolamine + monoethanolamine), (N-methyldiethanolamine + diethanolamine), (2-amino-2-methyl-1-propanol + monoethanolamine), and (2-amino-2-methyl-1-propanol + diethanolamine)', *Journal of Chemical and Engineering Data*, 48(3), pp. 703–707. doi: 10.1021/je020206a.

Mansourizadeh, A. and Ismail, A. F. (2009) 'Hollow fiber gas-liquid membrane contactors for acid gas capture: A review', *Journal of Hazardous Materials*, 171, pp. 38–53. doi: 10.1016/j.jhazmat.2009.06.026.

Mavroudi, M., Kaldis, S. P. and Sakellaropoulos, G. P. (2006) 'A study of mass transfer resistance in membrane gas-liquid contacting processes', *Journal of Membrane Science*, 272(1–2), pp. 103–115. doi: 10.1016/j.memsci.2005.07.025.

Moulin, P., Rouch, J. C., Serra, C., Clifton, M. J. and Aptel, P. (1996) 'Mass transfer improvement by secondary flows: Dean vortices in coiled tubular membranes', *Journal of Membrane Science*, 114(2), pp. 235–244. doi: 10.1016/0376-7388(95)00323-1.

Mulder, M. (1996) *Basic Principles of Membrane Technology*. 2nd Edition. Kluwer Academic. Springer Netherlands, second edition.

Nishikawa, N., Ishibashi, M., Ohta, H., Akutsu, N., Kamata, T., Kitamura, H. (1995) 'CO_2 Removal By Hollow Fiber Gas Liquid Contactor', *Energy Conversion and Management,* 36(6), pp. 415–418. doi: 10.1016/0196-8904(95)00033-A.

Narku-Tetteh, J., Afari, D. B., Coker, J. and Idem, R. (2018) 'Evaluation of the Roles of Absorber and Desorber Catalysts in the Heat Duty and Heat of CO_2 Desorption from Butylethanolamine-2-Amino-2-methyl-1-propanol and Monoethanolamine-Methyldiethanolamine Solvent Blends in a Bench-Scale CO_2 Capture Pilot Plant', *Energy and Fuels*. American Chemical Society, 32(9), pp. 9711–9726. doi: 10.1021/acs.energyfuels.8b02205.

Pakšiová, D., Fikar, M. and Skogestad, S. (2016) 'Modeling of carbon dioxide removal using membrane contactors', *2016 Cybernetics & Informatics (K&I)*, pp. 1–6. doi: 10.1109/CYBERI.2016.7438596.

Park, M. K. and Sandall, O. C. (2001) 'Solubility of carbon dioxide and nitrous oxide in 50 mass % methyldiethanolamine', *Journal of Chemical and Engineering Data*, 46(1), pp. 166–168. doi: 10.1021/je000190t.

Park, S. Y., Min, B. M., Lee, J. S., Nam, S. C., Han, K. H. and Hyun, J. S. (2004) 'Absorption characteristic of continuous CO_2 absorption process', ACS Division of Fuel Chemistry, Preprints, 49(1), pp. 249–250.

Paul, S., Ghoshal, A. K. and Mandal, B. (2007) 'Removal of CO_2 by Single and Blended Aqueous Alkanolamine Solvents in Hollow-Fiber Membrane Contactor: Modeling and Simulation', *Industrial and Engineering Chemistry Research*, (46), pp. 2576–2588. doi: 10.1021/ie061476f.

PRSB (2014) 'Module C - Hollow Fiber Membrane (HFM) Quality Check and Characterization', PETRONAS Research Sdn Bhd.

PRSB (2016) 'Module D - Hollow Fiber Membrane (HFM) Quality Check and Characterization', PETRONAS Research Sdn Bhd.

PRSB (2017) 'Conceptual Design of Commercial MBC Module', PETRONAS Research Sdn Bhd.

PSE (2018) *gPROMS ProcessBuilder Documentation 1.3.1*. Process Systems Enterprise Limited. United Kingdom.

Qi, Z. and Cussler, E. L. (1985a) 'Microporous hollow fibers for gas absorption. II. Mass transfer across the membrane', *Journal of Membrane Science*, 23(3), pp. 333–345. doi: 10.1016/S0376-7388(00)83150-6.

Qi, Z. and Cussler, E. L. (1985b) 'Microporous hollow fibers for gas absorption', *Journal of Membrane Science*, 23(3), pp. 333–345. doi: 10.1016/S0376-7388(00)83150-6.

Quek, V. C., Azmil, A. A., Chan, Z. P., Cao, Y., Kang, G., Li, M. and Jia, J. (2015) 'Process and System for Treating Natural Gas Feedstock', Patent, International Publication Number-WO2015003286A1'.

Quek, V. C., Shah, N. and Chachuat, B. (2018) 'Modeling for design and operation of high-pressure membrane contactors in natural gas sweetening', *Chemical Engineering Research and Design*. Institution of Chemical Engineers, 132, pp. 1005–1019. doi: 10.1016/j.cherd.2018.01.033.

Rezakazemi, M., Niazi, Z., Mirfendereski, M., Shirazian, S., Mohammadi, T. and Pak, A. (2011) 'CFD simulation of natural gas sweetening in a gas-liquid hollow-fiber membrane contactor', *Chemical Engineering Journal*. Elsevier B.V., 168(3), pp. 1217–1226. doi: 10.1016/j.cej.2011.02.019.

Rezazadeh, F., Gale, W. F., Akram, M., Hughes, K. J. and Pourkashanian, M. (2016) 'Performance evaluation and optimisation of post combustion CO_2 capture processes for natural gas applications at pilot scale via a verified rate-based model', International Journal of Greenhouse Gas Control. Elsevier Ltd, 53, pp. 243–253. doi: 10.1016/j.ijggc.2016.08.003.

Rongwong, W., Jiraratananon, R. and Assabumrungratt, S. (2012) 'Rate based modeling for CO_2 absorption using Monoethanolamine solution in a hollow fiber membrane contactor', *Journal of Membrane Science,* 429, pp.396-408. Elsevier Inc. doi: 10.1016/j.memsci.2012.11.050.

Sánchez, F. A., Pereda, S., Mohammadi, A. H., Richon, D., Brignole, E. A., Nacional, U., La, C., Km, C. and Blanca, B. (2009) 'Solubility of hydrocarbon in alkanolamine aqueous solution', *EQUIFASE Conference*, (January).

Shariati, A. and Khosravi Nikou, M. R. (2015) 'Sensitivity analysis for selection of an optimum amine gas sweetening process with minimum cost requirement', *Asia-Pacific Journal of Chemical Engineering*, 10(5), pp. 709–715. doi: 10.1002/apj.1907.

Shaw, T. P. and Hughes, P. . (2001) 'Optimize CO_2 removal', *Hydrocarbon Processing*, May, pp. 53–58.

Sohrabi, M. R., Marjani, A., Moradi, S., Davallo, M. and Shirazian, S. (2011) 'Mathematical modeling and numerical simulation of CO_2 transport through hollow-fiber membranes', *Applied Mathematical Modelling*. Elsevier Inc., 35(1), pp. 174–188. doi: 10.1016/j.apm.2010.05.016.

Souza, L. (2018) 'Modelling ethane absorption in MEA solution', *Petroleum Technology*.
Subhasish, M. (2017) 'A technical report on gas sweetening by amines. Petrofac Engineering India Ltd, Mumbai', (I).

Teletzke, E. and Madhyani, B. (2018) *Minimise amine losses in gas and liquid treating*. Available at: https://www.digitalrefining.com/article/1001504,Minimise_amine_losses_in_gas_and____liquid_treating.html#.XKMHpJgzZPY (Accessed: 3 January 2019).

TransCanada (2016) *Gas Quality Specifications-TransCanada and other pipelines*. Available at: http://www.tccustomerexpress.com/docs/Gas_Quality_Specifications_Fact_Sheet.pdf (Accessed: 1 January 2016).

U.S. Energy Information Administration (2019) *Henry Hub Natural Gas Spot Price*. Available at: https://www.eia.gov/dnav/ng/hist/rngwhhdD.htm (Accessed: 2 January 2019).

van Swaaij, W. P. M. and Versteeg, G. F. (1992) 'Mass transfer accompanied with complex reversible chemical reactions in gas—liquid systems: an overview', *Chemical Engineering Science*, 47(13–14), pp. 3181–3195. doi: 10.1016/0009-2509(92)85028-A.

Versteeg, G. F. and van Swaaij, W. P. M. (1988) 'Solubility and diffusivity of acid gases (CO_2 and N_2O) in aqueous alkanilamine solutions', *J. Chem. Eng. Data*, 32, p. 29.
Wang, D., Li, K. and Teo, W. K. (2000) 'Porous PVDF asymmetric hollow fiber membranes prepared with the use of small molecular additives', *Journal of Membrane Science*, 178(1–2), pp. 13–23. doi: 10.1016/S0376-7388(00)00460-9.

Wang, K. L. and Cussler, E. L. (1993) 'Baffled membrane modules made with hollow fiber fabric', *Journal of Membrane Science*, 85(3), pp. 265–278. doi: 10.1016/0376-7388(93)85280-A.

Wang, M., Lawal, A., Stephenson, P., Sidders, J. and Ramshaw, C. (2011) 'Post-combustion CO_2 capture with chemical absorption: A state-of-the-art review', *Chemical Engineering Research and Design*. Institution of Chemical Engineers, 89(9), pp. 1609–1624. doi: 10.1016/j.cherd.2010.11.005.

Wang, R., Li, D. F., Zhou, C., Liu, M. and Liang, D. T. (2004) 'Impact of DEA solutions with and without CO_2 loading on porous polypropylene membranes intended for use as contactors', *Journal of Membrane Science*, 229(1–2), pp. 147–157. doi: 10.1016/j.memsci.2003.10.022.

Wang, R., Zhang, H. Y., Feron, P. H. M. and Liang, D. T. (2005) 'Influence of membrane wetting on CO_2 capture in microporous hollow fiber membrane contactors', *Separation and Purification Technology*, 46(1–2), pp. 33–40. doi: 10.1016/j.seppur.2005.04.007.

Wang, Y. W., Xu, S., Otto, F. D. and Mather, A. E. (1992) 'Solubility of N_2O in Aqueous Solution of Diethylenetriamine', *J. Chem. Eng. Data*, 48, pp. 31–40. doi: 10.1021/je800409d.

Wang, Z., Fang, M., Yan, S., Yu, H., Wei, C. C. and Luo, Z. (2013) 'Optimization of blended amines for CO_2 absorption in a hollow-fiber membrane contactor', *Industrial and Engineering Chemistry Research*, 52(34), pp. 12170–12182. doi: 10.1021/ie401676t.

Wang, Z., Fang, M., Yu, H., Wei, C.-C. and Luo, Z. (2013) 'Experimental and Modeling Study of Trace CO2 Removal in a Hollow-Fiber Membrane Contactor, Using CO_2 -Loaded Monoethanolamine', *Industrial & Engineering Chemistry Research*, 52, pp. 18059–18070. doi: 10.1021/ie402264k.

Weiland, R. H., Dingman, J. C., Cronin, D. B., Treating, O. G. and Lane, W. (1997) 'Heat Capacity of Aqueous Monoethanolamine , Diethanolamine , N -Methyldiethanolamine , and N -Methyldiethanolamine-Based Blends with Carbon Dioxide', *Journal of Chemical & Engineering Data*, 42(5), pp. 1004–1006. doi: 10.1021/je960314v.

Wickramasinghe, S. R., Semmens, M. J. and Cussler, E. L. (1992) 'Mass transfer in various hollow fiber geometries', *Journal of Membrane Science*, 69(3), pp. 235–250. doi: 10.1016/0376-7388(92)80042-I.

Xu, B., Gao, H., Chen, M., Liang, Z. and Idem, R. (2016) 'Experimental Study of Regeneration Performance of Aqueous N,N-Diethylethanolamine Solution in a Column Packed with Dixon Ring Random Packing', *Industrial and Engineering Chemistry Research*, 55(31), pp. 8519–8526. doi: 10.1021/acs.iecr.6b00936.

Yeow, M. L., Liu, Y. T. and Li, K. (2004) 'Morphological study of poly(vinylidene fluoride) asymmetric membranes: Effects of the solvent, additive, and dope temperature', *Journal of Applied Polymer Science*, 92(3), pp. 1782–1789. doi: 10.1002/app.20141.

Zhang, Y. and Wang, R. (2013) 'Gas-liquid membrane contactors for acid gas removal: Recent advances and future challenges', *Current Opinion in Chemical Engineering*. Elsevier Ltd, 2(2), pp. 255–262. doi: 10.1016/j.coche.2013.03.008.

Zhang, H. Y., Wang, R., Liang, D. T. and Tay, J. H. (2008) 'Theoretical and experimental studies of membrane wetting in the membrane gas-liquid contacting process for CO_2 absorption', *Journal of Membrane Science*, 308(1–2), pp. 162–170. doi: 10.1016/j.memsci.2007.09.050.

Zydney, A. L., Aimar, P., Meireles, M., Pimbley, J. M. and Belfort, G. (1994) 'Use of the log-normal probability density function to analyze membrane pore size distributions: Functional forms and discrepancies', *Journal of Membrane Science*, 91(3), pp. 293–298. doi: 10.1016/0376-7388(94)80090-1.

Appendix A: Transport and Reaction Kinetic Correlations for predictive MBC modeling.

Macroscopic reaction rates between the CO_2 and the amine solvent are assumed to follow mass-action kinetics,

$$R_{CO_2} = -k_{MDEA}\, C_{CO_2}\, C_{MDEA} - k_{PZ}\, C_{CO_2}\, C_{PZ} \quad (A.1)$$

$$R_{MDEA} = -k_{MDEA}\, C_{CO_2}\, C_{MDEA} \quad (A.2)$$

$$R_{PZ} = -k_{PZ}\, C_{CO_2}\, C_{PZ} \quad (A.3)$$

The reaction rate constants are given by (Ko and Li, 2000; Sun et al., 2005; Lu et al., 2007)

$$k_{MDEA} = 4.01 \times 10^5 \exp\left(-\frac{5400}{T_l}\right) \quad (A.4)$$

$$k_{PZ} = 4.49 \times 10^9 \exp\left(-\frac{5712}{T_l}\right) \quad (A.5)$$

The diffusivity of CO2 in liquid is also estimated based on the analogy of N_2O diffusivity in solution (Versteeg and Van-Swaaij, 1988)

$$D_{CO_2,l} = D_{N_2O,l} \frac{D_{CO_2,H_2O}}{D_{N_2O,H_2O}} \quad (A.6)$$

The diffusivities of CO_2 and N_2O in water are given by

$$D_{CO_2,H_2O} = 2.35 \times 10^{-6} \exp\left(-\frac{2119}{T_l}\right) \quad (A.7)$$

$$D_{N_2O,H_2O} = 5.07 \times 10^{-6} \exp\left(-\frac{2371}{T_l}\right) \quad (A.8)$$

The diffusion coefficient of N_2O in liquid amine solution is estimated using the modified Stokes-Einstein relation (Brown, 1991; Mandal et al., 2003;Wang et al., 2013)

$$D_{N_2O,l} = D_{N_2O,H_2O} \left(\frac{\mu_{H_2O}}{\mu_l}\right)^{0.6} \quad (A.9)$$

where the viscosities μ_{H_2O} and μ_l of the water and amines, respectively, are obtained from the package 'UNIQUAC-RK'. Likewise, the temperature-corrected diffusivities of MDEA and PZ amines in the liquid phase are correlated using the modified Stokes-Einstein relation (Brown, 1991; Mandal et al., 2003).

$$D_{\mathrm{MDEA,l}} = D_{\mathrm{MDEA,H_2O}} \frac{T_\mathrm{l}}{273} \left(\frac{\mu_{\mathrm{H_2O}}}{\mu_\mathrm{l}}\right)^{0.6} \quad \text{(A.10)}$$

$$D_{\mathrm{PZ,l}} = D_{\mathrm{PZ,H_2O}} \frac{T_\mathrm{l}}{273} \left(\frac{\mu_{\mathrm{H_2O}}}{\mu_\mathrm{l}}\right)^{0.6} \quad \text{(A.11)}$$

where the diffusivities of MDEA and PZ in water, and the liquid and water dynamic viscosities are obtained from the the package 'UNIQUAC-RK'. The diffusivity of CO_2 in NG was estimated from empirical correlations based on kinetic gas theory [Cussler, 2009; Bird et al., 1960]

$$D_{\mathrm{CO_2,NG}} = \frac{T_\mathrm{g}^{1.75}\left(\frac{1}{M_{\mathrm{CO_2}}}+\frac{1}{M_{\mathrm{NG}}}\right)^{1/2}}{10^5\, P_\mathrm{g}\left[\left(\sum V_{\mathrm{CO_2}}\right)^{1/3}+\left(\sum V_{\mathrm{NG}}\right)^{1/3}\right]^2} \quad \text{(A.12)}$$

where $M_{\mathrm{CO_2}}$ and M_{NG} stand for the molecular weights of CO_2 and NG; and the summations of atomic diffusion volumes for the species of the CO_2-NG gas mixture are taken as $\sum V_{\mathrm{CO_2}} = 26.9$ and $\sum V_{\mathrm{NG}} = 24.42$. The diffusivity of CO_2 in N_2 gas was obtained from the package 'Advanced Peng-Robinson'. Lastly, the surface tension of liquid was estimated using the package 'UNIQUAC-RK'.

The numerical values reported in Tables A.1 and A.2 correspond to the temperature and pressure conditions in the lab- and pilot-scale MBC modules in Chapter 3 and 4 (see Tables 3.1 and 4.2).

Table A.1. Model parameters used in the lab and pilot plant MBC simulations in Chapter 3.

Parameters	N_2/CO_2 (Lab)	CH_4/CO_2 (Lab)	NG (Pilot)
Diffusivity of CO_2 in gas, $D_{\mathrm{CO_2,g}}$ [$m^2\ s^{-1}$]	1.44×10^{-6}	1.50×10^{-6}	3.23×10^{-7}
Diffusivity of CO_2 in liquid, $D_{\mathrm{CO_2,l}}$ [$m^2\ s^{-1}$]	1.00×10^{-9}	1.46×10^{-9}	1.46×10^{-9}
Diffusivity of MDEA in liquid, $D_{\mathrm{MDEA,l}}$ [$m^2\ s^{-1}$]	1.39×10^{-10}	2.37×10^{-10}	2.37×10^{-10}
Diffusivity of PZ in liquid, $D_{\mathrm{PZ,l}}$ [$m^2\ s^{-1}$]	3.26×10^{-10}	5.32×10^{-10}	5.31×10^{-10}
Reaction rate constant of MDEA, k_{MDEA} [$m^3 mol^{-1}\ s^{-1}$]	4.01×10^{-3}	9.83×10^{-3}	9.83×10^{-3}
Reaction rate constant of PZ, k_{PZ} [$m^3 mol^{-1}\ s^{-1}$]	15.5	40.0	40.0
Henry's constant, $H_{\mathrm{CO_2,l}}$ [m^3 Pa mol^{-1}]	2878	3636	3588
Density of gas, ρ_g [kg m^{-3}]	13.3	8.5	49.2
Density of liquid, ρ_l [kg m^{-3}]	994	986	986
Dynamic viscosity of liquid, μ_l [kg $m^{-1}\ s^{-1}$]	2.49×10^{-3}	1.73×10^{-3}	1.74×10^{-3}
Surface tension of amine solvent, γ [N m^{-1}]	0.046	0.046	0.046

Table A.2. Model parameters used in the lab and pilot plant MBC simulations in Chapter 4.

Parameters	N_2/CO_2 (Lab)	NG (Pilot)
Diffusivity of CO_2 in gas, $D_{CO_2,g}$ [$m^2\ s^{-1}$]	3.01×10^{-7}	3.10×10^{-7}
Diffusivity of CO_2 in liquid, $D_{CO_2,l}$ [$m^2\ s^{-1}$]	1.50×10^{-9}	1.47×10^{-9}
Diffusivity of MDEA in liquid, $D_{MDEA,l}$ [$m^2\ s^{-1}$]	2.85×10^{-10}	2.39×10^{-10}
Diffusivity of PZ in liquid, $D_{PZ,l}$ [$m^2\ s^{-1}$]	6.34×10^{-10}	5.37×10^{-10}
Reaction rate constant of MDEA, k_{MDEA} [$m^3 mol^{-1}\ s^{-1}$]	1.13×10^{-2}	9.83×10^{-3}
Reaction rate constant of PZ, k_{PZ} [$m^3 mol^{-1}\ s^{-1}$]	46.4	39.9
Henry's constant, $H_{CO_2,l}$ [m^3 Pa mol^{-1}]	5825	4759
Density of gas, ρ_g [kg m^{-3}]	73.4	48.9
Density of liquid, ρ_l [kg m^{-3}]	971.3	987
Dynamic viscosity of liquid, μ_l [kg $m^{-1}\ s^{-1}$]	1.39×10^{-3}	1.71×10^{-3}
Surface tension of amine solvent, γ [N m^{-1}]	0.040	0.046

Appendix B: Radial Domain Scaling for Membrane Dry and Wet Spatial Subdomains and MBC Model Equations for Process Wide Design and Operation.

A rescaling of the radial dimension in the partial differential equations was conducted in order for the membrane dry and wet spatial subdomains to be rectangular. The steps for the domain scaling are provided as per below:

Step 1: Specify the distribution domains of membrane dry and wet spatial to be rectangular such that $[r_1 : r_{w\_ref}]$ and $[r_{w\_ref} : r_2]$, respectively as shown in Figure B.1. The wetted radius reference, r_{w_ref} can be estimated as $r_{w\_ref} = r_2 - [r_2 - r_1]\,\zeta_{ref}$ in accordance to Eq. (3.10); where ζ_{ref} can be a parameter of value from (0,1).

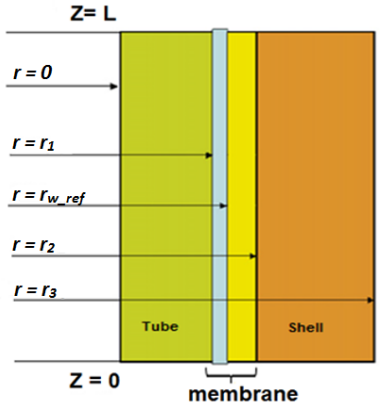

Figure B.1:Spatial domains in MBC model

Step 2: Account for the predicted $r_w(z)$ from Eq. (3.10) in the mass conservation equations in membrane dry and membrane wet and boundary conditions as summarized in Table B.2.

Table B.1: Mass conservation equations in membrane dry and membrane wet and boundary conditions with rescaling of the radial dimension.

Section	Material Balances
Membrane-Dry Phase $(r,z) \in [r_1, r_{\mathrm{w}}(z)] \times [0, L]$:	$\frac{r_{w\_ref}-r_1}{r_w(z)-r_1} D_{\mathrm{CO_2,md}} \left[\frac{\partial^2 C_{\mathrm{CO_2}}(r,z)}{\partial r^2} + \frac{1}{r}\frac{\partial C_{\mathrm{CO_2}}(r,z)}{\partial r}\right] = 0$
Membrane-Wet Phase $(r,z) \in [r_{\mathrm{w}}(z), r_2] \times [0, L]$:	$\frac{r_2 - r_{w\_ref}}{r_2 - r_w(z)} D_{\mathrm{i,mw}} \left[\frac{\partial^2 C_i(r,z)}{\partial r^2} + \frac{1}{r}\frac{\partial C_i(r,z)}{\partial r}\right] + R_i(C_i(r,z)) = 0, i \in \{\mathrm{CO_2}, \mathrm{sol}\}$
Boundary Conditions	
Gas-liquid Interface $r=r_w(z)$, $z \in [0, L]$:	$C_{\mathrm{CO_2}}(r_{\mathrm{w}}^-(z), z) = \frac{H_{\mathrm{CO_{2,l}}}}{ZRT_{\mathrm{g}}} C_{\mathrm{CO_2}}(r_{\mathrm{w}}^+(z), z)$, $\frac{r_2-r_{w\_ref}}{r_2-r_w(z)} \frac{\partial C_{\mathrm{sol}}(r,z)}{\partial r}\Big\|_{r=r_{\mathrm{w}}^+(z)} = 0$, $\frac{r_{w\_ref}-r_1}{r_w(z)-r_1} D_{\mathrm{CO_2,md}} \frac{\partial C_{\mathrm{CO_2}}(r,z)}{\partial r}\Big\|_{r=r_{\mathrm{w}}^-(z)} = \frac{r_2-r_{w\_ref}}{r_2-r_w(z)} D_{\mathrm{CO_2,mw}} \frac{\partial C_{\mathrm{CO_2}}(r,z)}{\partial r}\Big\|_{r=r_{\mathrm{w}}^+(z)}$.
Liquid-membrane Interface $r=r_2$, $z \in [0, L]$:	$C_i(r_2^+, z) = C_i(r_2^-, z)$, $i \in \{\mathrm{CO_2}, \mathrm{sol}\}$ $D_{i,\mathrm{l}} \frac{\partial C_i(r,z)}{\partial r}\Big\|_{r=r_2^+} = \frac{r_2-r_{w\_ref}}{r_2-r_w(z)} D_{i,\mathrm{mw}} \frac{\partial C_i(r,z)}{\partial r}\Big\|_{r=r_2^-}$, $i \in \{\mathrm{CO_2}, \mathrm{sol}\}$

The model equations and boundary conditions used for modeling of MBC in Chapter 4 are summarized in Table B.2.

Table B.2. Summary of model equations and boundary conditions used in Chapter 4 : MBC model

Section	**Material Balances**
Gas Phase $(r,z) \in [0, r_1] \times [0, L]$:	$\frac{d\overline{C_{\mathrm{CO_2}}}(z)}{\partial z} = -\frac{2\, D_{\mathrm{CO_2,md}}}{\overline{v}_{\mathrm{g}}(z) r_1}\left[1 - \frac{ZRT_{\mathrm{g}}^{\mathrm{in}}\overline{C_{\mathrm{CO_2}}}(z)}{P_{\mathrm{g}}^{\mathrm{in}}}\right]\frac{\partial C_{\mathrm{CO_2}}(r,z)}{\partial r}\Big\vert_{r=r_1^+}$ $\frac{d\overline{v_{\mathrm{g}}}(z)}{\partial z} = -\frac{2\, D_{\mathrm{CO_2,md}}}{r_1}\frac{ZRT_{\mathrm{g}}^{\mathrm{in}}}{P_{\mathrm{g}}^{\mathrm{in}}}\frac{\partial C_{\mathrm{CO_2}}(r,z)}{\partial r}\Big\vert_{r=r_1^+}$, $N_{i,\mathrm{g}}^{\mathrm{out}} = N_{i,\mathrm{g}}^{in} - N_{i,\mathrm{l}}^{\mathrm{out}}, \quad i \in \{\mathrm{CH_4}, \mathrm{C_2H_6}, \mathrm{C_3H_8}\}$, $y_{i,\mathrm{g}}^{\mathrm{out}} = \frac{x_{i,\mathrm{l}}^{\mathrm{in}}\, P_i^{\mathrm{vap,in}}}{P_{\mathrm{g}}^{\mathrm{out}}}, \qquad i \in \{\mathrm{H_2O}, \mathrm{MDEA}, \mathrm{PZ}\}$, $N_{\mathrm{i,g}}^{\mathrm{out}} = N\pi r_1^2 \overline{v}_{\mathrm{g}}(0)\frac{y_{i,\mathrm{g}}^{\mathrm{out}} P_{\mathrm{g}}}{ZRT_{\mathrm{g}}}, \quad i \in \{\mathrm{H_2O}, \mathrm{MDEA}, \mathrm{PZ}\}$
Membrane-Dry Phase $(r,z) \in [r_1, r_{\mathrm{w}}(z)] \times [0, L]$:	$\frac{r_{w\_ref} - r_1}{r_w(z) - r_1} D_{\mathrm{CO_2,md}}\left[\frac{\partial^2 C_{\mathrm{CO_2}}(r,z)}{\partial r^2} + \frac{1}{r}\frac{\partial C_{\mathrm{CO_2}}(r,z)}{\partial r}\right] = 0$
Membrane-Wet Phase $(r,z) \in [r_{\mathrm{w}}(z), r_2] \times [0, L]$:	$\frac{r_2 - r_{w\_ref}}{r_2 - r_w(z)} D_{\mathrm{i,mw}}\left[\frac{\partial^2 C_i(r,z)}{\partial r^2} + \frac{1}{r}\frac{\partial C_i(r,z)}{\partial r}\right] + R_i(C_i(r,z)) = 0, i \in \{\mathrm{CO_2}, \mathrm{sol}\}$
Liquid Phase $(r,z) \in [r_2, r_3] \times [0, L]$:	$v_{\mathrm{l}}(r)\frac{\partial C_i(r,z)}{\partial z} = D_{i,\mathrm{l}}\left[\frac{\partial^2 C_i(r,z)}{\partial r^2} + \frac{1}{r}\frac{\partial C_i(r,z)}{\partial r} + \frac{\partial^2 C_i(r,z)}{\partial z^2}\right] + R_i(C_i(r,z)), \quad i \in \{\mathrm{CO_2}, \mathrm{sol}\}$ $v_{\mathrm{l}}(r) = 2\overline{v}_{\mathrm{l}}(r_3^2 - r_2^2)\frac{r^2 - r_2^2 + 2r_3^2 \ln\left(\frac{r_2}{r}\right)}{4r_2^2 r_3^2 - r_2^4 - 3r_3^4 - 4r_3^4 \ln\left(\frac{r_2}{r_3}\right)}, \ \overline{v}_{\mathrm{l}} = \frac{F_{\mathrm{l}}^{\mathrm{in}}}{\pi R_{\mathrm{m}}^2(1-\emptyset)}$, $C_{i,\mathrm{l}}^{\mathrm{out}} = \frac{\mathrm{y}_{i,\mathrm{g}}^{\mathrm{in}} P_{\mathrm{g}}}{H_{i,\mathrm{l}}}, \quad i \in \{\mathrm{CH_4}, \mathrm{C_2H_6}, \mathrm{C_3H_8}\}$, $N_{i,\mathrm{l}}^{\mathrm{out}} = C_{i,\mathrm{l}}^{\mathrm{out}} F_{\mathrm{l}}, \quad i \in \{\mathrm{CH_4}, \mathrm{C_2H_6}, \mathrm{C_3H_8}\}$, $N_{\mathrm{i,l}}^{\mathrm{out}} = N_{\mathrm{i,l}}^{\mathrm{in}} - N_{\mathrm{i,g}}^{\mathrm{out}}, \quad i \in \{\mathrm{H_2O}, \mathrm{MDEA}, \mathrm{PZ}\}$, $F_{\mathrm{l}}^{\mathrm{in}}\, \rho_{\mathrm{l}}\, C_{\mathrm{p}}\frac{dT_{\mathrm{l}}(z)}{dz} = -\pi r_1^2 N\frac{d\left(\overline{v_{\mathrm{g}}}(z)\overline{C_{\mathrm{CO_2}}}(z)\right)}{dz}\Delta H_{\mathrm{r}}$
	Boundary Conditions
Gas inlet, z=*L*:	$\overline{v}_{\mathrm{g}}(L) = \frac{M_{\mathrm{g}}^{\mathrm{in}}}{N\pi r_1^2 \rho_{\mathrm{g}}}, \qquad \overline{C_{\mathrm{CO_2}}}(L) = \frac{y_{\mathrm{CO_2,g}}^{\mathrm{in}} P_{\mathrm{g}}^{\mathrm{in}}}{ZRT_{\mathrm{g}}}$

Liquid inlet, z=0, $r \in [r_2, r_3]$:

$$C_{\mathrm{CO_2}}(r,0) = f_{\mathrm{CO_2,l}}^{\mathrm{in}} C_{\mathrm{sol}}^{\mathrm{in}}\,,\quad C_{\mathrm{sol}}(r,0) = C_{\mathrm{sol}}^{\mathrm{in}}\,,$$

$$Q_{\mathrm{vap}} = F_{\mathrm{l}}^{\mathrm{in}}\,\rho_{\mathrm{l}}\,C_{\mathrm{p}}\,\left(T_{\mathrm{l}}^{\mathrm{in}} - T_{\mathrm{l}}(0)\right) = \bar{v}_{\mathrm{g}}(0) N\pi r_1^2 \sum \frac{x_{i,\mathrm{l}}^{\mathrm{in}}\,P_i^{\mathrm{vap,in}}}{ZRT_{\mathrm{g}}}\,\Delta H_i^{\mathrm{vap}}\left(T_{\mathrm{l}}^{\mathrm{in}}\right)$$

Liquid outlet

$z=L$, $r \in [r_2, r_3]$:

$$\left.\frac{\partial C_i(r,z)}{\partial z}\right|_{z=L} = 0 \qquad i \in \{\mathrm{CO_2}, \mathrm{sol}\}$$

Gas-membrane Interface

$r=r_1$, $z \in [0, L]$:

$$C_{\mathrm{CO_2}}(r_1^+, z) = \overline{C_{\mathrm{CO_2}}}(z)$$

Gas-liquid Interface

$r=r_w(z)$, $z \in [0, L]$:

$$C_{\mathrm{CO_2}}(r_{\mathrm{w}}^-(z), z) = \frac{H_{\mathrm{CO_{2,l}}}}{ZRT_{\mathrm{g}}} C_{\mathrm{CO_2}}(r_{\mathrm{w}}^+(z), z)\,,$$

$$\left.\frac{r_2 - r_{w\_ref}}{r_2 - r_w(z)} \frac{\partial C_{\mathrm{sol}}(r,z)}{\partial r}\right|_{r=r_{\mathrm{w}}^+(z)} = 0\,,$$

$$\frac{r_{w\_ref} - r_1}{r_w(z) - r_1} D_{\mathrm{CO_2,md}} \left.\frac{\partial C_{\mathrm{CO_2}}(r,z)}{\partial r}\right|_{r=r_{\mathrm{w}}^-(z)} = \frac{r_2 - r_{w\_ref}}{r_2 - r_w(z)} D_{\mathrm{CO_2,mw}} \left.\frac{\partial C_{\mathrm{CO_2}}(r,z)}{\partial r}\right|_{r=r_{\mathrm{w}}^+(z)},$$

$$r_{\mathrm{w}}(z) = r_2 - [r_2 - r_1]\,\mathfrak{Z}(z)\,,$$

$$\mathfrak{Z}(z) = \frac{\int_{\frac{-2\gamma\cos\theta}{\Delta P_{\mathrm{TMPD}}(z)}}^{\delta_{\max}} \delta^2 f(\delta)\,d\delta}{\int_0^{\delta_{\max}} \delta^2 f(\delta)\,d\delta},$$

$$P_{\mathrm{TMPD}}(z) = P_{\mathrm{l}}^{\mathrm{out}} + 8\mu_{\mathrm{l}}\bar{v}_{\mathrm{l}} \frac{r_3^2 - r_2^2}{4r_2^2 r_3^2 - r_2^4 - 3r_3^4 - 4r_3^4 \ln\left(\frac{r_2}{r_3}\right)} (L - z) - P_{\mathrm{g}}^{\mathrm{in}}$$

Liquid-membrane Interface

$r=r_2$, $z \in [0, L]$:

$$C_i(r_2^+, z) = C_i(r_2^-, z)\,,\quad i \in \{\mathrm{CO_2}, \mathrm{sol}\}$$

$$D_{i,\mathrm{l}} \left.\frac{\partial C_i(r,z)}{\partial r}\right|_{r=r_2^+} = \frac{r_2 - r_{w\_ref}}{r_2 - r_w(z)} D_{i,\mathrm{mw}} \left.\frac{\partial C_i(r,z)}{\partial r}\right|_{r=r_2^-},\ i \in \{\mathrm{CO_2}, \mathrm{sol}\}$$

Liquid Boundary

$r=r_3$, $z \in [0, L]$:

$$\left.\frac{\partial C_i(r,z)}{\partial r}\right|_{r=r_3},\ i \in \{\mathrm{CO_2}, \mathrm{sol}\}$$